Super-Resolution Microscopy of Synaptic Proteins

DISSERTATION ZUR ERLANGUNG DES
NATURWISSENSCHAFTLICHEN DOKTORGRADES
DER JULIUS-MAXIMILIANS-UNIVERSITÄT
WÜRZBURG

vorgelegt von

Sarah Aufmkolk

geboren in Arnsberg

Würzburg, Juli 2017

Eingereicht am: ....

Mitglieder der Promotionskommission:

Vorsitzender: ....

Gutachter: Prof. Dr. Markus Sauer

Gutachter: Prof. Dr. Manfred Heckmann

Tag des Promotionskolloquiums: ....

Doktorurkunde ausgehändigt am: ....

"Pictures provide information."

Sauer and Heilemann, 2017

"Use it or lose it!"

Dr. Marian Diamond

Abstract

The interaction of synaptic proteins orchestrate the function of one of the most complex organs, the brain. The multitude of molecular elements influencing neurological correlations makes imaging processes complicated since conventional fluorescence microscopy methods are unable to resolve structures beyond the diffraction-limit.

The implementation of super-resolution fluorescence microscopy into the field of neuroscience allows the visualisation of the fine details of neural connectivity. The key element of my thesis is the super-resolution technique *d*STORM (*direct* Stochastic Optical Reconstruction Microscopy) and its optimisation as a multi-colour approach. Capturing more than one target, I aim to unravel the distribution of synaptic proteins with nanometer precision and set them into a structural and quantitative context with one another.
Therefore *d*STORM specific protocols are optimized to serve the peculiarities of particular neural samples.
In one project the brain derived neurotrophic factor (BDNF) is investigated in primary, hippocampal neurons. With a precision beyond 15 nm, pre- and post-synaptic sites can be identified by staining the active zone proteins bassoon and homer. As a result, hallmarks of mature synapses can be exhibited. The single molecule sensitivity of *d*STORM enables the measurement of endogenous BDNF and locates BDNF granules aligned with glutamatergic pre-synapses. This data proofs that hippocampal neurons are capable of enriching BDNF within the mature glutamatergic pre-synapse, possibly influencing synaptic plasticity.
The distribution of the metabotropic glutamate receptor mGlu4 is investigated in physiological brain slices enabling the analysis of the receptor in its natural environment. With dual-colour *d*STORM, the spatial arrangement of the mGlu4 receptor in the pre-synaptic sites of parallel fibres in the molecular layer of the mouse cerebellum is visualized, as well as a four to six-fold increase in the density of the receptor in the active zone compared to the nearby environment. Prior functional measurements show that metabotropic glutamate receptors influence voltage-gated calcium channels and proteins that are involved in synaptic vesicle priming. Corresponding *d*STORM data indeed suggests that a subset of the mGlu4 receptor is correlated with the voltage-gated calcium channel $Ca_v2.1$ on distances around 60 nm.
These results are based on the improvement of the direct analysis of localisation data. Tools like coordinated based correlation analysis and nearest neighbour analysis of clusters centroids are used complementary to map protein connections of the synapse. Limits and possible improvements of

these tools are discussed to foster the quantitative analysis of single molecule localisation microscopy data.

Performing super-resolution microscopy on complex samples like brain slices benefits from a maximised field of view in combination with the visualisation of more than two targets to set the protein of interest in a cellular context. This challenge served as a motivation to establish a workflow for correlated structured illumination microscopy (SIM) and *d*STORM. The development of the visualisation software coSI*d*STORM promotes the combination of these powerful super-resolution techniques even on separated setups. As an example, synapses in the cerebellum that are affiliated to the parallel fibres and the dendrites of the Purkinje cells are identified by SIM and the protein bassoon of those pre-synapses is visualised three-dimensionally with nanoscopic precision by *d*STORM.

In this work I placed emphasis on the improvement of multi-colour super-resolution imaging and its analysing tools to enable the investigation of synaptic proteins. The unravelling of the structural arrangement of investigated proteins supports the building of a synapse model and therefore helps to understand the relation between structure and function in neural transmission processes.

Zusammenfassung

Das Zusammenspiel von synaptischen Proteinen organisiert präzise die Funktion eines der komplexesten Organe, dem Gehirn. Die Vielfalt der molekularen Bestandteile, die diese neurologischen Beziehungen beeinflussen, verkomplizieren den Bildgebungsprozess, da die konventionellen Fluoreszenzmikroskopiemethoden Strukturen, die kleiner sind als das Beugungslimit, nicht auflösen können.

Die Implementierung der hochauflösenden Fluoreszenzmikroskopie in das Gebiet der Neurowissenschaften ermöglicht die Visualisierung feiner Details neurologischer Verbindungen. Die hochauflösende Mikroskopietechnik *d*STORM (*direct* Stochastic Optical Reconstruction Microscopy) und dessen Optimierung als Mehrfarbenanwendung sind Schlüsselelemente meiner Doktorarbeit. Mit der Möglichkeit mehr als ein Protein zu messen, ist es mein Ziel die Verteilung synaptischer Proteine mit nanometer Genauigkeit zu entschlüsseln und diese in ein strukturelles und quantitativ Verhältnis zueinander zu setzen.
Aus diesem Grund wurden *d*STORM spezifische Protokolle den Besonderheiten der jeweiligen neuronalen Proben angepasst und optimiert.
In einem Projekt wird der neurotrophe Faktor BDNF (brain derived neurotrophic factor) in primären hippocampalen Neuronen untersucht. Mit einer Auflösungspräzision von unter 15 nm kann durch eine Färbung der Proteine Bassoon und Homer in der aktiven Zone die prä- und postsynaptische Seite identifiziert werden. Daraus resultierend können Kennzeichen für vollentwickelte Synapsen erfasst werden. Die Einzelmolekülsensitivität von *d*STORM ermöglicht erstmalig die Messung von endogenem BDNF und zeigt, dass die BDNF Gruppierungen entlang von glutamatergen Präsynapsen verteilt sind. Diese Daten beweisen, dass hippocampale Neuronen die Möglichkeit haben, BDNF in der vollausgebildeten glutamatergen Präsynapse anzureichern und somit möglicherweise synaptische Plastizität beeinflussen.
Die Verteilung des metabotropen Glutamatrezeptors mGlu4 wird in physiologischen Gehirnschnitten untersucht. Das ermöglicht den Rezeptor in seiner natürlichen Umgebung zu analysieren. Mit Zweifarben-*d*STORM Messungen wird das räumliche Arrangement der mGlu4 Rezeptoren in der Präsynapse der parallelen Fasern der molekularen Schicht des Mauskleinhirns visualisiert und eine vier- bis sechsfache erhöhte Dichte des Rezeptors in der aktiven Zone, verglichen mit dem näheren Umfeld, aufgezeigt. Vorausgegangene funktionale Messungen zeigen, dass metabotrope Glutamatrezeptoren spannungsgesteuerte Calciumkanäle und Proteine, die in synaptische Vesikelgrundierung involviert sind, beeinflussen.

Entsprechende *d*STORM Daten deuten darauf hin, dass ein Teil der mGlu4 Rezeptoren mit dem spannungsgesteuerten Calciumkanal Ca$_v$2.1 auf einer Distanz von circa 60 nm korreliert ist.

Diese Ergebnisse basieren auf der Verbesserung der direkten Analyse der Lokalisationsdatensätze. Werkzeuge, wie die Koordinaten basierte Korrelationsanalyse und die Nächste Nachbaranalyse von Clusterschwerpunkten werden sich ergänzend benutzt, um ein umfassendes Bild von Proteinverbindungen in der Synapse zu erzeugen. Die Grenzen und die Verbesserungsmöglichkeiten dieser Werkzeuge werden diskutiert, um die quantitative Analyse von Einzelmoleküldatensätzen voranzubringen.

Die Durchführung von hochauflösender Mikroskopie an komplexen Proben, wie Gehirnschnitten, wird begünstigt durch die Maximierung der Aufnahmefläche in Kombination mit der Möglichkeit mehr als zwei Zielstrukturen zu visualisieren, um somit das Protein von primären Interesse in einen zellulären Zusammenhang zu setzen. Diese Herausforderung hat als Motivation gedient, ein Messprotokoll für korrelierte Strukturierte Beleuchtungsmikroskopie (SIM) und *d*STORM zu etablieren. Die Entwicklung der Visualisierungssoftware coSI*d*STORM erleichtert die Kombination dieser beiden leistungsstarken, hochauflösenden Techniken, sogar wenn diese auf getrennten Mikroskopieaufbauten umgesetzt werden.
Als ein Beispiel werden Synapsen, die zwischen den parallelen Fasern in der molekularen Schicht des Cerebellums und den Purkinje-Zellen ausgebildet werden, mit SIM identifiziert und das Protein Bassoon in diesen Präsynapsen wird mit einer nanometergenauen Präzision drei-dimensional mit *d*STORM Messungen visualisiert.

In meiner Arbeit habe ich den Fokus auf die Weiterentwickelung von hochauflösender Mehrfarbenmikroskopie und die damit verbundenen analytischen Werkzeuge gelegt, sodass die Untersuchung von synaptischen Proteinen ermöglicht wird. Die Herausarbeitung des strukturellen Arrangements der untersuchten synaptischen Proteine unterstützt den Aufbau eines Models der Synapse und erweitert somit das Verständnis des Zusammenhangs von Struktur und Funktion in neuronalen Übertragungsvorgängen.

Contents

x

Chapter 1

Introduction and Theoretical Background

In my thesis I aimed to optimise multi-colour super-resolution imaging with *direct* Stochastic Optical Reconstruction Microscopy (*d*STORM) to analyse synaptic proteins. Since super-resolution methods rose as a precious new tool in biology in the last ten years, I want to introduce the recent development of these techniques with special focus on the function of single molecule localisation microscopy.

With regard to the vast variety of questions in the nanoscopic scale in neuroscience, it was just consequent to approach imaging the brain with the method *d*STORM. The review "The Big and the Small: Challenges of Imaging the Brain's Circuits" by Lichtman and Denk, 2011 gave a solid overview of the challenges of imaging in neuroscience. Here they stated five problems highlighting the main demand in neuroimaging. First they claimed the immense diversity of cell types that need to be distinguished when connecting them to certain functional patterns. This leads secondly to the need of drawing a map of functions and connecting the pathways to a structural peculiarity. Therefore imaging along the extension of whole neurons is mandatory. However neurons occur in sizes from some microns to millimeters. This extension exceeds the field of view of nanoscopic imaging processes. This is a main motivation for the improvement of correlative methods, in which multiple imaging modes are combined. But the field of super-resolution imaging is still adapting to the requirements of synaptic analysis. Last they claim the importance and need for dense or saturated reconstruction, a problem that rose to another level with the increase of imaging precision.

Already published in 2011 this review still gives a frame for ideas to address in this fast evolving field. In my thesis I discuss solutions to some of the aforementioned challenges. To set a context for these methods I want to introduce in this chapter the background of super-resolution microscopy and the basic theory behind it.

Using *d*STORM as foundation for this work, I will present approaches to quantitative structural analysis of synaptic proteins and their improvement over time. In the following sections, analytical tools for interpreting single molecule localisation microscopy (SMLM) will be portrayed. Furthermore I

will address the motivation behind the projects I applied *d*STORM on, unravelling the nanoscopic distribution of the brain derived neurotrophic factor (BDNF) and the metabotropic glutamate receptor mGlu4.

Another part of my work is the evaluation of how to combine quantitative analysis of endogenous protein distribution on a nanoscopic scale with a microscopic overview of the structural context of neurological tissue. Discussing the limitation of multi-colour *d*STORM, the debate on correlative methods is fostered and I will present correlated SIM-*d*STORM imaging as valuable alternative.

1.1 History and Principles Leading to Super-Resolution Microscopy

1.1.1 Fluorescence Microscopy

Fluorescence microscopy is one of the most widely used methods in biology. The Stokes shift of absorption to emission spectrum, describing the principle of emission light having a longer wavelength than the absorbed wavelength, allows us to filter the introduced excitation light leaving behind solely fluorescent light with an improved contrast to conventional microscopy. Paired with the exquisite specificity of many cell markers, which I will introduce on a later occasion, fluorescence microscopy is a valued tool for bringing biological questions into light. Unravelling questions on a cellular base one has to recognize that the achievable resolution should match the studied object. To draw a mechanistic picture from cell accumulations to the smallest links in the chain, fluorescence methods needed to overcome the limitations inflicted by the diffraction of light, which prevents processes and structures beyond 200 nm to be resolved. For many years the diffraction limit as it was introduced by Ernst Abbe and Lord Rayleigh (Abbe, 1873; Rayleigh, 1896) was stated insuperable. Abbe described that the distance d of two lines of a periodic grid imaged through a microscope, can still be resolved if $d = \frac{\lambda}{2NA}$, with λ being the wavelength of light and NA the numerical aperture of the objective. The Rayleigh criterion states the diffraction limit for two pointlike light-sources can be still separated if the maximum of the PSF, describable by an Airy-function, of the first object lies in the first minimum of the second PSF. This leads to the equation of a resolvable distance of $d = \frac{1.22\lambda}{2NA}$. Therefore having an emission wavelength of a fluorophore of 600 nm, using an objective with a typical NA of 1.45, we can just resolve structures that are at least at a distance of 252 nm. Improvement of the resolution can be gained by using smaller wavelength or a larger NA of the objective. However, we are limited to visual wavelength above 300 nm and a maximal NA of state-of-the-art objectives. In conclusion all classical fluorescence microscopy methods using visible light underlay this principle of diffraction limited resolution, which prevents structures beyond 200 nm from being resolved.

1.1.2 Methods to Circumvent the Diffraction Limit

The advent of super-resolution microscopy, which contains all the methods, which circumvent the diffraction limit, was made by the detection of a single subdiffraction particle, when Moerner and Kador, 1989 and Orrit and Bernard, 1990 showed the independent detection of single dopant molecules in a host crystal in the 1990s. Evolving from this, in Betzig, 1995 the idea of a super-resolution method was based on the spatial or temporal definement of otherwise identical molecules in one focal area. The follow ups of the spectroscopic distinction by fluorescence spectra or lifetime resulted in multiple approaches for multicolour imaging. A critical advance towards proposing this theory in biological samples was the discovery of optically switchable constructs based on organic dyes by Bates, Blosser, and Zhuang, 2005 and Heilemann et al., 2005. Though a multitude of approaches entered the field of imaging some basic ideas crystallised and these key approaches can be categorised in mainly two groups. The deterministic approach, where for example an illumination pattern is introduced to the sample or a stochastic approach, where the temporal confinement of fluorophore signalling is used in an advantageous matter. Figure 1.1 gives a quick overview on the main methods of these groups and addresses the contradictory trends of imaging speed and approachable resolution. One approach of the deterministic group is to decrease the illumination spot artificially by "deexitation" (stimulated emission depletion, STED Klar and Hell, 1999) resulting in a signal emitting area smaller than the diffraction limit. Another method representing this group relies on the readout of fluorescence along thin strips, named Structural Illumination Microscopy (SIM, Gustafsson, 2000; Gustafsson, 2005; Gustafsson et al., 2008; Heintzmann and Cremer, 1999). Citing Ströhl and Kaminski, 2016, SIM has evolved to a powerful and versatile optical super-resolution technique, combining improved resolution with good acquisition speed and flexibility of use. In principle, any fluorophore that can be imaged in wide-field fluorescence microscopes is amenable to a SIM microscope and thus the complete catalogue of fluorescence probes that has been developed for biochemical analysis is available for the method.

Illuminating the sample with patterned light causes interference fringes in the detected raw image (Moiré patterns). Those patterns contain higher spatial frequency information, which again describe the fine details of a sample, that normally get filtered out by the microscope objective. By varying this structured illumination multiple times, these high spatial frequencies can be shifted to lower ones and therefore be mathematically translated into highly resolved image information, leading to a resolution improvement which is twice the diffraction limit. A detailed elaboration of the evolution of this technique is found in Ströhl and Kaminski, 2016. SIM is a technique this work benefits from and therefore a short overview of the used system is described in the methodical chapter.

The evolution of Single Molecule Localisation Microscopy pushed the field of super-resolution microscopy to spatial resolutions of a few nanometers. The peculiarities of the different approaches should be named here, while
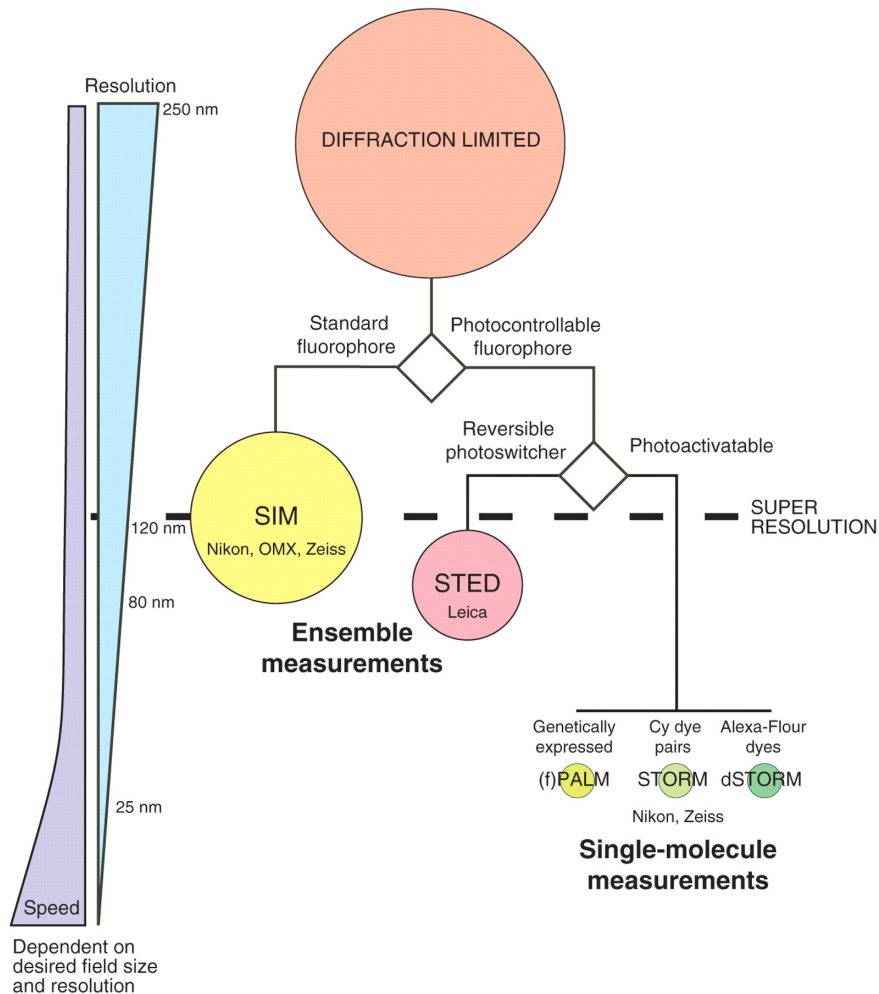
FIGURE 1.1: In the review "Super-resolution microscopy at a glance" Galbraith and Galbraith, 2011 it is visualised that there is an inverse relationship between image acquisition speed and image resolution. The main methods are displayed and grouped regarding their special characteristics including fluorescent probes, speed and resolution. Copyright permission has been granted by Company of Biologists LTD.

the underlying principle of SMLM will be described in one of the following chapters. Singe-molecule-based techniques use light induced manipulation of fluorescent dyes to have just a sparse subset of probes in a fluorescent state being spatially separated further than the diffraction limit and then being localised with high accuracy. The methods differ mainly in the kind of fluorescent probe used to realise this separation. Photo-activated localisation microscopy (PALM, Betzig, 2005, Manley et al., 2008) use genetically expressed photoactivatable or photoconversionalable fluorocent proteins to generate a sparse subset per frame. Stochastic optical reconstruction microscopy (STORM Bates, Blosser, and Zhuang, 2005) uses pairs of fluorophores, a reporter and an activator dye (e.g. Cy5-Cy3). The reporter dye

photoswitches under certain chemical conditions, when activated by the absorption wavelength of the activator dye. A more straight forward approach is *direct*STORM using also photoswitchable standard fluorescent probes like Cy5, that switch in the presence of thiol between a bright *on* and a reduced *off* state with a long lifetime. Further specifications are reviewed in Klein, Proppert, and Sauer, 2014.

Fluorophores – Various Colours for Microscopy

Fluorescent probes are a crucial link to this field. The precision with which fluorophores can be localised depends on the fluorophore properties. The choice of fluorophore lies in the nature of the method and the target being labelled. While already in the 1940s Coons, Creech, and Jones, 1941 introduced the concept of labelling a biological structure with antibodies connected to fluorescein, the discovery of the green fluorescence protein GFP in 1962 by Shimomura, 1979 opened up new possibilities to fluorescent microscopy. The demand on visualizing more than one protein was served in the followup, though a milestone for SMLM was the advent of photoswitchable fluorophores, such as PA-GFP, which was adopted for PALM by Patterson and Lippincott-Schwartz, 2002; Subach et al., 2010. Currently the rational design of FPs evolves further. FPs as tools for photoswitching and other powerful labelling strategies are presented in Day and Davidson, 2009, as well as specified tools for neuroscience as shown by Shen, Lai, and Campbell, 2015, Zhao and Campbell, 2015. Parallel to this a multitude of organic dyes evolved, serving the demand on higher photon yields, photostability and specific photo-physical properties. It was first shown that the carbocyanine Cy5 is reversible switchable in an oxygen-depleted thiol containing aqueous buffer, while being irradiated with short wavelengths of 337 - 532 nm Heilemann et al., 2005; Bates, Blosser, and Zhuang, 2005. To facilitate the switch in between an *on* and *off* state, Cy5 was connected with a green-absorbing activator fluorophore (Cy3). This led to the development of stochastic optical reconstruction microscopy (STORM, Bates, Blosser, and Zhuang, 2005) with a activator-reporter-based fluorophore pair. On the discovery that Cy5 could be switched without an activator, *direct*STORM (Heilemann et al., 2005) was announced. Multi-colour *d*STORM is the method this thesis is based on and until now several dyes have been tested for this approach as shown in Linde et al., 2009; Linde et al., 2013.

From Photoswitching to Super-Resolution

*d*STORM relies on photoswitchable fluorophores, or more directly, organic dyes. This means, that they are reversibly switched between a fluorescent *on* and non-fluorescent *off* state. This property enables a temporal control of the fluorescent emission, so that the majority of fluorophores can be set into a dark state and just a small subset will emit light per acquisition time frame.

The centre of the emission pattern of a single object can be determined by fitting a two-dimensional Gaussian function. Concretely the image of the PSF of a single emitter is detected on a two-dimensional, single-photon-sensitive array. Each pattern is fitted with a two-dimensional Gaussian-function with the result that the centre of the fluorophore can be determined with a sub-pixel resolution. This process is repeated for several frames until every fluorophore has been detected at least once, but rather multiple times and a super-resolved image can be reconstructed by the localisation data. The ac-
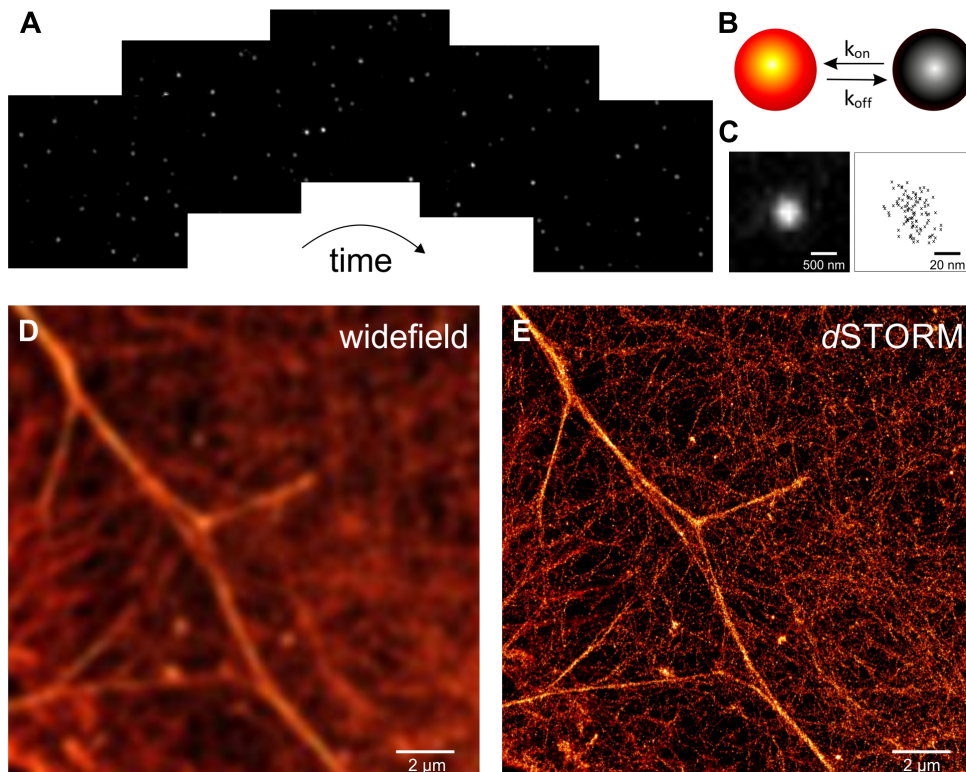

FIGURE 1.2: A) Acquisition of several frames with seperated emission pattern of single objects. B) The on-off ratio k_{on} to k_{off} is determined by the chemical environment and the illumination energy. C) The precision of the two-dimensional fit to the emission pattern is directly proportional to the $1/\sqrt{N}$, N number of photons. Comparison of a widefield image D) and the reconstructed dSTORM image E) of the cytoskeleton in a U2OS cell by staining actin with Alexa Fluor 647 phalloidin. The ultra-structure of filaments is now resolved.

curacy of this process is dependent on the photoswitching cycle. The precision, with which the emission pattern can be fitted is dependent on the number of detected photons N and the standard-deviation σ of the PSF, resulting in a dependency of the precision to $\sim\sigma/\sqrt{N}$. Furthermore the precision can be affected by the pixelsize of the camera and the background signal (Mortensen et al., 2010).

The peculiarity of the dyes used in dSTORM lies in the photoswitching cycle they undergo. This process is sketched by a Jablonski diagram in Figure 1.3.

While under irradiation with suitable light the dyes undergo a fluorescent cycle. They can perform with a lower probability an inter-system-crossing into a triplet state. In this reactive state the molecule can be reduced to a non-fluorescent dark state. Reducing and oxygen-depleting agents like thiols favour or stabilise this dark state respectively, and support the advantageous constellation that a major subset of fluorescent probes are in an *off* state. Those molecules can enter reversibly the fluorescent cycle in a stochastic manner by irradiation of light or oxidation. Therefore a controlled manipulation of photophysics by laser intensity and reducing reagent is enabled. These processes were investigated in many ways and the most important findings are summarised in the article "How to switch a fluorophore: from undesired blinking to controlled photoswitching" by Linde and Sauer, 2014.

While a certain labelling density is necessary to serve a nanoscopic resolution according to the Nyquist-Shannon sampling theorem (Shannon, 1949), dense samples need to be temporal confined sufficiently (Compare Figure 1.3 A). In practice the distance should be further departed than the diffraction limit, an estimated minimum value of 0.6 emitter per μm^2 is needed to enable reliable spot finding and fitting Wolter et al., 2011, though this value is dependent on the fitting algorithm used. This interplay between labelling density and therefore staining approaches (immunostaining, click chemistry, transgenic marker etc.) and photophysical properties of used dyes needs to be taken into account when choosing probes for imaging.

The detectable spot density is dependent on the applied fitting and reconstruction software. Several open-source packages are available and serve reliable fitting algorithm with mainly real-time reconstruction velocity. In this work solely the Software `rapidSTORM` was applied, which was elaborated in the Sauer group and is described extensively in Wolter et al., 2011, Wolter et al., 2012b. Different approaches are discussed and explained in the Review "Fluorophore localisation algorithms for super-resolution microscopy" (Small and Stahlheber, 2014).

Multi-Colour Approach

A multi-colour SMLM approach was first realised with probes that contained activator and reporter fluorophores. While the activation dyes differs, the reporter dyes were the same, which minimised the effects of achromatic aberration and STORM images with up to three colours were shown in Bates et al., 2007 and Dani et al., 2010. One draw back is that nonspecific activation results in cross talk. Though correction is possible and applied in the previously mentioned paper, it leads to a high exclusion of localisations and therefore of information. Sequential methods that differentiate activator-free fluorophores with complete separation of the spectral information are well used with *d*STORM (Linde et al., 2013, Andreska et al., 2014), though correction of chromatic aberration needs to be applied. Another chromatic abberation free method is spectral-demixing (SD-) *d*STORM. First shown with the fluorophore pair Alexa Fluor 647 and CF680 by Lampe et al., 2012,

this approach uses the partially overlapping absorption and emission spectra to excite the dyes with one wavelength and splits the fluorescent signal with a dichroic mirror on two cameras. The signal of each fluorophore is visible on both channels and the fluorophore type can be assigned by its emission ratio. Both approaches in *d*STORM are dependent on the variety of fluorophores with a specific absorption and emission spectra. Though a multitude of fluorophores exists, a vast majority is not suitable for high quality super-resolution imaging. The fluorophore pairs should perform ideally in the same chemical environment. Although a working switching buffer condition for a multitude of fluorophores is defined (Linde et al., 2011), suitable dye pairs are still rare.
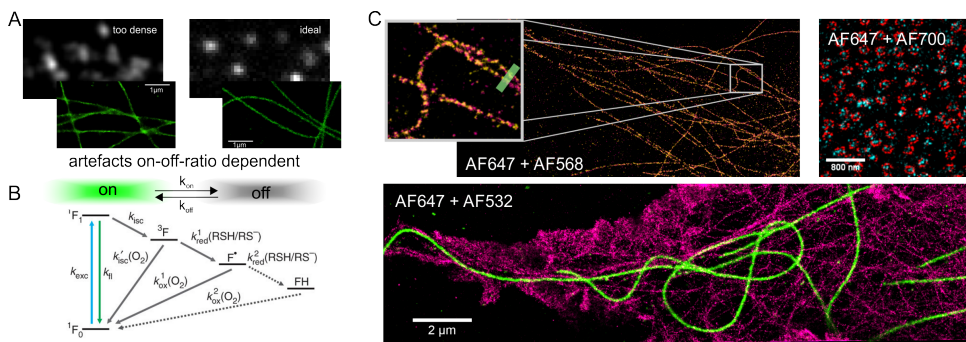

FIGURE 1.3: A) The fitting algorithm used is sensitive to the density of emission events and therefore to the on-off-ratio. B) The Jablonski diagram outlines transitions from a fluorescent on-state to non-fluorescent states. Chemical surroundings influence the redox-milieu and therefore the switching rates. Those parameters are individual to different fluorophores. C) Successful imaged fluorophore pairs, which work in the same reduction buffer conditions.

In Figure 1.3 C three functional colour combinations for *d*STORM are presented. However, this thesis mainly demonstrates the capability of the fluorophore pair Alexa Fluor 647 and Alexa Fluor 532 to process super-resolution imaging of synaptic proteins and to enable further correlation analysis.

Three-Dimensional SMLM

To identify the position of a single fluorophore in three-dimensional space, distinguished information about the PSF pattern specific to a certain axial position needs to be defined. There are different approaches, whereas one of them introduces a cylindrical lens in the detection pathway of the widefield setup to manipulate the PSF pattern (Kao and Verkman, 1994). This asymmetrical distortion enables a PSF pattern assignment to every axial position. This technique is well adapted for SMLM measurements and shown in Huang et al., 2008a. Another technique introduces multiple focal planes to analyse the PSF. Therefore the image gets split with a relative focus offset in the axial position. The axial position of the emitter can be extracted

from the focus pattern ratio of the respective planes. This was shown with the signal split into two regions of the same camera by Juette et al., 2008. This approach is easy to realise using a setup with two cameras already adapted for sequential two-colour imaging. The introduced difference in focal planes matches the pathway distance necessary for achromatic correction for green and red focal planes. But also an approach to combine biplane and SD-*d*STORM was successfully shown in Winterflood et al., 2015. A novel technique named temporal, radial-aperture-based intensity estimation (TRABI) by Franke, Sauer, and Linde, 2017 extracts three-dimensional information directly from the intensity distribution of the PSF pattern of a two-dimensional acquisition-track. A combination with biplane configuration enables 3D-*d*STORM reconstruction with an axial range of 600 nm and an axial precision of approximately 20 nm. This approach is used in this work to realise 3D-*d*STORM imaging.

1.1.3   Analysis of Single Molecule Localisation Microscopy Data

As quoted at the very beginning "Images provide information." (Sauer and Heilemann, 2017). Identifying molecules that are directly linked to a fluorophore, with nanometer precision, tempts one to expect a 1:1 stoichiometry between the number of detected fluorophores and the target protein. Nevertheless artefacts and methodological peculiarities may arise that lead to undercounting or overcounting. Imperfect labelling efficiency is a factor for undercounting affecting all SMLM methods, as well as co-incidental blinking of two fluorescent probes seated in diffraction limited distance. While first quantitative PALM experiments did not take into account that reversible photoblinking might occur (Greenfield et al., 2009), the problem of overcounting was addressed. This occured with FPs as it did with mEos2, whose specific blinking properties were recently understood and through the grouping of blink events overcounting could be prevented by Annibale et al., 2011. Further attempts are discussed in Deschout et al., 2014 and McEvoy et al., 2012, in which similar photophysical behaviour for the photoconvertible FP mMaple was reported. Organic fluorescent probes used in particular for *d*STORM return reversibly from a long dark-state several times and are advantageously brighter and more photostable than common FPs. However, to correct for overcounting the average number of localisations per secondary and primary label bound to an epitope needs to be estimated. Here I note that counting is possible and was recently shown successfully by Ehmann et al., 2014 quantifying the Bruchpilot protein and therefore identifying the state of an active zone. But several challenges remain when using SMLM for quantitative measurements, with the result that strict controls are absolutely essential. A strength of *d*STORM is its high precision, making distributional analysis an obvious application area. In the following I will briefly introduce the utilised algorithm specified on the output format of localisation data.

Precision   The quality of a SMLM image is defined by the localisation precision. Despite the possibility of evaluating the precision with the Mortensen equation Mortensen et al., 2010, another approach is presented in Endesfelder et al., 2014, which takes the experimental influence of every measurement into account. This approach is in my opinion favourable for estimating the precision of SMLM images. Here the localisation precision is determined by the distances of nearest-neighbour fluorophores in consecutive frames. This leads to an effective tool to describe the precision, also not fully accounting for the influences of labelling, photophysics of the dye and the drift stability of the setup, and is used in this work, whenever the precision is stated.

Cluster Analysis   In neurological systems proteins often accumulate in nanoscopic domains and their analysis supports the understanding of functional processes. For example the clustering of receptor proteins on the cell membrane initiates a signalling pathway (Laine et al., 2016). Even single proteins, labelled potentially with several antibodies and therefore multiple fluorophores, can be claimed as a cluster of localisations. By this method, cluster finding algorithms help to unravel localisation data and facilitate quantitative analysis.

Ripley's K Function   The Ripley's K function is a descriptive statistic approach to identify deviations from spatial homogeneity of distributed points. A homogeneous data set is for example a set of localisations in a plane that are distributed in a manner that in any given area with the radius r the same number of localisations occur. The Ripley's K analysis came to use on PALM and dSTORM data identifying spatial inhomogeneities of proteins in the plasma membrane by Owen et al., 2010. In our approach we use the H-function, which is the linearised form normalised to be equal to zero for all r in a random distribution. Is the value significantly above zero, clustering is indicated and a peak indicates dimensions of a highly clustered feature.

DBScan   Ripley's K cluster analysis is biased towards circular clusters, though arbitrary shaped clusters are the norm in biological samples. DBScan is a density-based clustering algorithm proposed by Ester et al., 1996 and has been used in various biological studies (Nan et al., 2013, Endesfelder et al., 2013). DBScan introduces two variables to identify groups of points that are packed densely, the maximum radius r of a neighbourhood and the minimum number of points minPts that form a neighbourhood. The principle is visualised in Figure 1.4. With a starting point a cluster is built up if in r there are at least the stated minimum number of neighbours. If the neighbours fulfil the same criterion, the cluster propagates (green circles), if there are no more neighbours the point is assigned as a boundary point (yellow circles). Points which fail the criterion are outliners (blue circles). The values for r and MinPts need to be critically evaluated for every sample.
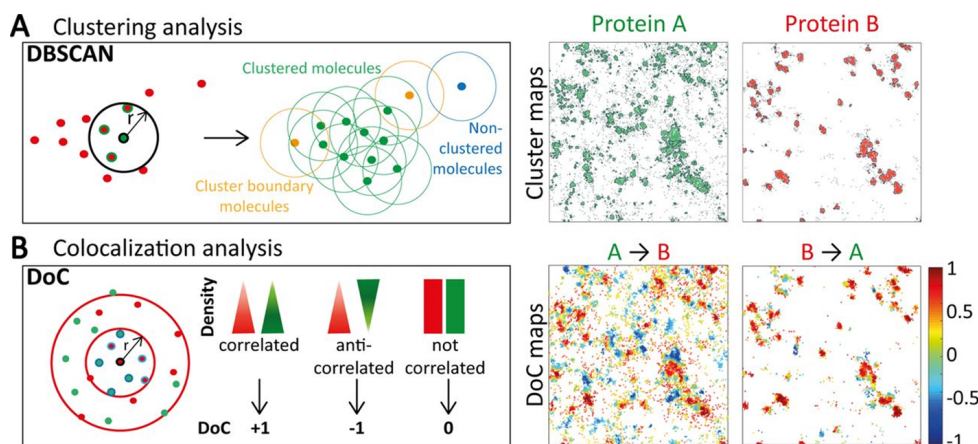
FIGURE 1.4: A) The clustering analysis tool DBScan identifies by a set number of neighbours in a defined radius points that belong to a cluster(green) or defines a boarder (yellow) and outliners (blue) and can therefore provide robust cluster maps of SMLM data. B) A coordinate based colocalisation approach by Malkusch et al., 2012 calculated the local density of each protein population (red and green points) at increasing radius sizes around each localisation. For each population a gradient is defined and tested for correlation, resulting in a degree of correlation (DoC) for every localisation. The DoC score rates from -1 to 1, while -1 indicates perfect segregation, 0 no correlation and 1 colocalisation. Imaged published by Pageon et al., 2016 - copyright granted.

Alpha-Shapes The approximation of a cluster area is sometimes of interest. The alpha-shape algorithm can be utilised as an analysis tool that confines the area more precisely than a standard convex hull. The concept of alpha shapes is a generalisation of the convex hull. This approach formulates a shape for a spatial points set, like SMLM data, by building sub-graphs of the Delaunay triangulation. Delaunay triangulation creates a triangle mesh of a point set. With the parameter alpha of this algorithm the desired level of detail is controlled. Introduced by Edelsbrunner, Kirkpatrick, and Seidel, 1983 as a general shaping tool, it is currently used for molecular shaping Albou et al., 2009.

There are several other techniques to define clusters and for the project investigating BDNF in hippocampal neurons another approach is described. Many of the explained analysis routines are implemented in an analysis software package named locan based on the Wolfram language Mathematica and was developed by PD Dr. Sören Doose. Locan is used among other applications for identifying higher order synaptic protein clusters, representing the active zone of a synapse.

Colocalisation of Two Populations In conventional fluorescence microscopy approaches for colocalisation, that evaluate the relative overlap of the signal of two different sources in defined pixel areas, are standard

tools. Common approaches for intensity, correlation-based colocalisation are the Pearson's correlation coefficient (Pearson, 1896; Manders et al., 1992) or Mander's overlap coefficient (Manders, Verbeek, and Aten, 1993). These approaches used on SMLM data require image processing like histogramming or blurring and therefore loose the advantage of super-resolved information that is given by the collected information of all individual localisations (Pageon et al., 2016). However, localisation based approaches struggle with the identification of colocalisation distances lying above the achievable resolution. Proteins that were colocalising in the diffraction limited images might now be displayed 50 nm apart. A recently presented approach, the coordinate-based correlation (CBC) method by Malkusch et al., 2012 enables an analysis of the affiliation of two protein groups. This method applies its algorithm directly to each localisation coordinate and defines a density gradient of both protein populations along increasing radii around every localisation. To compare the distributions of both populations a rank correlation coefficient (Spearman correlation) is used. This correlation value is weighted by a value proportional to the distance to the nearest neighbour to reduce long-distance effects. Each molecule gets assigned a value in between -1 (anticorrelated) and 1 (perfectly correlated). 0 describes a noncorrelated state. The correlation in between two protein populations can be evaluated bidirectionally. To gain a better interpretation of the colocalisation values and the choice of variables, the evaluation should be compared to simulations that match specific experimental conditions or experimental data sets that serve as a control.

1.2 Super-Resolution Imaging of Synaptic Proteins

From the beginning of SMLM approaching biological topics, synaptical proteins have served as interesting targets. While investigations into synaptic plasticity were supported by PALM measurements, imaging dynamic changes of actin in spines (Frost et al., 2010, Izeddin et al., 2011), also the nanoscopic structure of actin and spectrin could be elucidated with STORM measurements in Xu, Zhong, and Zhuang, 2013. We could reproduce the spectrin measurements and show the periodic structure in mature motoneurons with *d*STORM and also reveal the synaptic cleft by measuring the pre- and post-synaptic active zone proteins bassoon and homer (compare Figure 1.5).

The reviews Tønnesen and Nägerl, 2013 and Laine et al., 2016 give an excellent overview of multiple SMLM approaches in neuroscience.

Undeniable synaptic processes involve various components. Therefore multi-colour *d*STORM is an essential premise to target a hypothesis of the distributional affiliation of two proteins. Depending on the dimensions of the sample, one must redefine any hypothesis in order to be answered with super-resolution microscopy. On a flat sample, it might be sufficient to analyse the 2D projection as we did in the BDNF project. We examined the distribution of the neurotrophic factor in the defined area of hippocampal
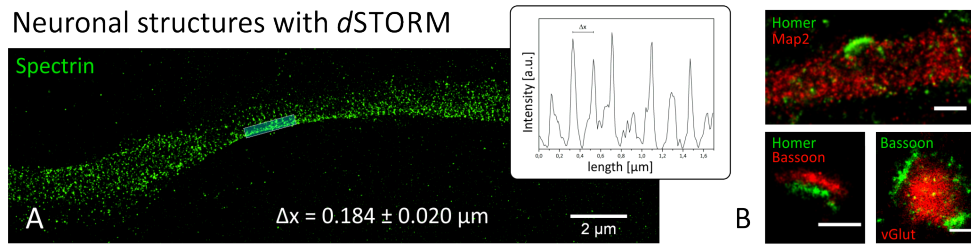
FIGURE 1.5: A) Immunolabelling of spectrin in motoneurons. The same periodic structure as shown in Xu, Zhong, and Zhuang, 2013 of hippocampal neurons was found. The mean value of the distances in between the periodic structure of 184 ± 20 nm is evaluated of 20 measuring sites. B) Various stainings of synaptic proteins in a hippocampal cell culture. Scale bars 500 nm.

neurons. This is a relatively flat structure and contains the targets of interest within a small area. However, imaging in a three-dimensional system, for once cell accumulations or tissue slices, call for a different approach. Figure 1.6 maps briefly circumstances and possibilities to approach those samples.

In the mGlu4 project I performed measurements in cryo-slices of the cerebellum of a mouse brain. Therefore the orientation of the synapse is naturally quite arbitrary. For analysing the metabotropic glutamate receptor mGlu4, it is of interest to differentiate in between front and side view of the synapse. While one colour 3D *d*STORM measurements are quite adapted, three dimensional two-colour measurements are delicate to handle. This was a motivation to extract the orientation information out of two-dimensional data with cluster analysing tools.

Some characteristics of targets are dependent on more than one interaction partner. To enable a multi-colour approach with a larger field of view, improving the orientation in brain areas of interest, I implemented a work-flow for correlated SIM-*d*STORM at our institute and it was tested on a neurological sample structure. We were interested in synapses that are affiliated with climbing fibres and dendrites of the Purkinje cells in the molecular layer of the cerebellum. For visualisation and manipulation of these datasets the Bachelor student Sebastian Reinhardt and I developed the Software coSI*d*STORM.

1.2.1 BDNF - Image Based Analysis of a Synaptic Protein

Brain-derived neurotrophic factor (BDNF) is a member of the neurotrophin family that mediates as a key factor for synaptic refinement, plasticity and learning (Barde, Edgar, and Thoenen, 1982; Park and Poo, 2013). Long-term potentation (LTP) is a prototypical model to study synaptic plasticity and cellular learning (Korte et al., 1995, Figurov et al., 1996, Gottschalk et al., 1998, Huang et al., 2008b) and BDNF/TrkB signaling in the hippocampus and emotional circuits is deeply involved in this process. Various studies
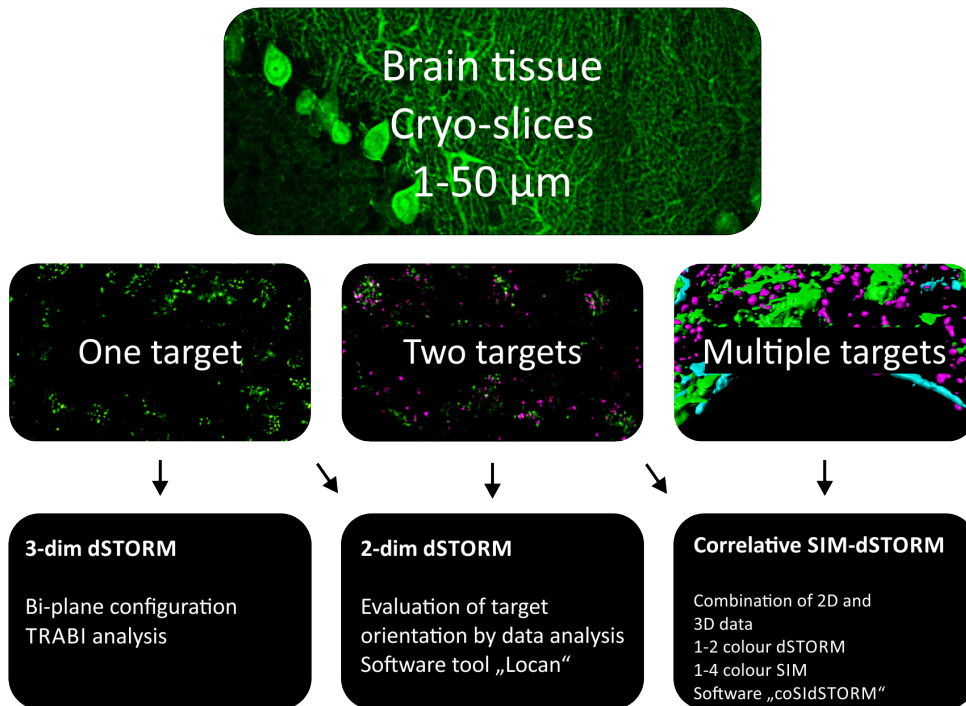
FIGURE 1.6: How to approach a neuronal tissue sample? In a physiological brain tissue the cell density and variety is enormous. With selective staining a contrast is granted. However, approaches that capture the three-dimensional extent are advantageous. For single protein investigations 3D **d**STORM is easy to apply, although for two colour staining it is challenging. Here I suggest analysing tools to identify the orientation of e.g. synapses. Increasing the imaging dimensions almost to a four-fold wider field of view, up to 80 x 80 μm^2, I used correlated SIM-*d*STORM to visualize a highly-resolved protein in the context of more than one interaction partner measured with SIM.

elucidate the function and effects of BDNF at synaptic sites (Blum and Konnerth, 2005, Park and Poo, 2013), though localisation attempts to study distributions were complicated due to the low amounts of endogenous BDNF normally found in neurons in vivo (Dieni et al., 2012). On these grounds various studies rely on vector-driven expression of recombinant BDNF to support detection (Canossa et al., 2001, Dean et al., 2009, Cheng et al., 2011). Several studies claim contrary findings on the main residence of BDNF. While many conclude that BDNF is stored and released from both, axonal and dendritic compartments, it is suggested in Hartmann, Heumann, and Lessmann, 2001, Brigadski, Hartmann, and Lessmann, 2005 that postsynaptic secretory granules close to glutamatergic synapses are a preferential site of BDNF release. On the contrary Altar et al., 1997, Conner et al., 1997, Dieni et al., 2012 visualize BDNF at pre-synaptic sites in brain sections, affirming synaptic effects of BDNF by anterograde release. *d*STORM provides

the sensitivity and the resolution to reveal the nanoscopic distribution of endogenous BDNF in hippocampal neurons. In the publication "High abundance of BDNF within glutamatergic pre-synapses of cultured hippocampal neurons" Andreska et al., 2014, which was published in cooperation with Robert Blum of the Institute for Clinical Neurobiology, we clarified whether BDNF is mainly present in the pre- or post-synapse or at extra-synaptic sites. Therefore we established a staining that defines pre- and post-synaptic sites and performed a colocalisation analysis on two-colour *d*STORM images to specify the affiliation of BDNF.

1.2.2 mGlu4 – Localisation Based Analysis in Tissue

This project investigates the distribution of the metabotropic glutamate receptor 4 (mGlu4) at the pre-synaptic active zone. The metabotropic glutamate receptors are a family of class C G-protein-coupled receptors (GPCRs) that modulate synaptic transmission processes. GPCRs play a critical role in the modulation by negative feedback loops of the voltage-dependent calcium channels and therefore influence calcium-dependent processes and ultimately suppression of neurotransmitter release as described in Dolphin, 2003. mGlu4 is a member of group III metabotropic glutamate receptors that is concentrated in active zones, which was shown in several studies with immuno-EM approaches (Shigemoto et al., 1996, Corti et al., 2002). Since the structural and functional composition of the active zone is a key element of understanding synaptic transmission as summarised in the Review of Südhof, 2012 super-resolution methods like *d*STORM are an important tool to unravel the distribution of AZ correlated proteins with nanometer precision.

In this context the distribution of mGlu4 at a central excitatory synapse is of key interest in this cooperation with the group of Prof. Dr. Davide Calebiro (Institute of Pharmacology and Toxicology; University clinic of Würzburg). In Kinoshita et al., 1996 a hypothesis is already drawn that mGlu4 is located pre-synaptically in the parallel fibres arising from the granule corps in the cerebellar cortex, though the nanoscopic distribution could not be unravelled. Therefore we investigated the organisation of this glutamate receptor in relation to different components of the pre-synaptical site at the synapses in between parallel fibres and Purkinje cells in the molecular layer of the cerebellum in cryo-sliced brain tissue.

In my thesis I concentrate on the improvement of quantitative analysis of dual-colour *d*STORM data to define the spatial arrangement of mGlu4 with, for example, bassoon as a component of the pre-synaptical active zone and the P/Q-type voltage-dependent calcium channel $Ca_v2.1$. I aim to establish a localisation data-based analysis as a reliable tool for cluster and correlation analysis and affirm with that approach the hypothesis of the mGlu4 receptor being affiliated with several pre-synaptic proteins. Additionally to the structural analysis we add novel quantitative information to the spatial distribution.

1.2.3   *d*STORM - SIM Microscopy - a Correlative Method

Analysis of super-resolution two-colour images reveal an insight of protein distribution, nevertheless we miss the bigger picture since the cellular context of the proteins stays literally dark. To reveal the environment and gain orientation in brain tissue I introduced a correlative approach of SIM and *d*STORM imaging. *d*STORM enables super-resolved imaging by accumulating the signals of several thousand frames and reaches precisions of approximately 10 nm. This procedure is on a relatively small field of view with required acquisition times of several minutes. To gain an overview of spacious samples, faster approaches are advantageous. A rapid search mode that facilitates the identification of areas of interest or specific cell types is a necessary tool to regain orientation in tissue. SIM offers a fast data acquisition and still achieves a high structural resolution in the range of 100 nm and the sample preparation for both methods is consistent. The diverging requirements in the fluorophore properties utilised for these two methods supports their joint-venture. To perform any SMLM method single emission events need to be spatially isolated. The method is highly dependent on the blinking quality of the fluorophore. The photo physical properties affect the reachable resolution and accuracy of this method. A high quantum yield is recommended due to the proportional dependence between detected photons and precision, as described before, as well as a suitable on-off-ratio. Therefore the list of convenient fluorophores is limited. It was shown that quantitative measurements with *d*STORM are most reliably performed using the red emitting carbocyanine dye Alexa Fluor 647 or its homolog Cy5 (Ehmann et al., 2014). SIM is more independent in the choice of suitable fluorescence marker. Therefore standard fluorescent proteins like GFP and RFP are applicable. A photo-stable fluorescent probe is recommended and should be enhanced by a proper chemical anti-fading reagent.

An ideal platform should combine both illumination techniques in one setup as shown in Mönkemöller et al., 2015. Here it is also mentioned that a particular challenge are the low laser powers that are provided in commercial setups, which result often in a laser power density of less than 0.5 kW/cm^2. We recommend laser powers of approximately 5 kW/cm^2, though the exact value is highly dependent on the fluorophore and the labelling density.

Few attempts at multi-modal super-resolution microscopy have been conducted. Matsuda et al., 2010 used a 3D-SIM optical platform to acquire data for single molecule localisation microscopy. Rossberger et al., 2013 demonstrated a combined platform for SIM and SMLM and imaged identical regions of H3K293 cells. Also, (Hamel et al., 2014) used 3D-SIM to obtain multi-colour SIM data and compared several structures with STORM data on a single setup.

A combined setup facilitates the procedure of imaging, but it is less likely that laboratories are equipped with one. Furthermore a software to combine the data of different approaches is a missing link. In my thesis I will therefore introduce a work-flow to perform both techniques on individual

setups and introduce our home-made software coSI*d*STORM. This software enables the visualisation of high content data sets in three dimensions and offers tools to align the images based on the target structure itself. Furthermore, I show the application of coSI*d*STORM using a three-colour labelled brain slice through the assignment of single, super-resolved synapses to different neuron types.

Chapter 2

Materials and Methods

2.1 Fluorescence Labelling of Biological Samples

2.1.1 Sample Preparation

Cover-slips Preparation

Cover-slip For super-resolution microscopy high-precision coverslips (no. 1.5 thickness) to mount the samples are mandatory. High-precision cover glasses feature an exceptionally accurate thickness of 170 ± 5 μm. Following chambers or cover-slips were used in the experiments:

Labtek Nunc 2	8 well chamber; thickness 1.5 Borosilicat; #155409 Nunc
Ibidi μ-slide	8 well chamber; thickness 1.5 (high precision) glass bottom; #80827 Ibidi
Round cover-slip	18 mm and 24 mm round cover-slip; thickness 1.5 (high precision); #LH23.1 and #PK26.1 Carl Roth GmbH
Attofluor cellchamber	Chamber for prior listed cover-slips; #A7816 Life Technologies
μ-Dish grid chamber	Chamber with grid matrix; 500 μm grid distance #81168 and 50 μm grid distance #81148 Ibidi

Coating of Cover-slips for Brain Tissues Clean the glass for 15 min in 1M KOH and 5 min in ethanol in a sonicator. Incubate it afterwards in a 2% 3-Aminopropyltriethoxysilan in methanol solution for 4 min. Wash with ddH2O and let it dry.

Preparation Cryoslices

The immersion-fixated brain is stored in PFA. Incubate the brain for two days in 30 % sucrose solution and then freeze it in isopentan on dry ice. For cryosectioning a Leica 3050 S cryotome was used. The slicing temperature

depends on the demanded slice thickness, but varies in between -20 °C to -28 °C.

2.1.2 Standard Labelling Protocols

Protocols for staining biological samples enabling fluorescence microscopy need to be adjusted and optimised for every target structure. In the following two protocols are described that were used repetitively. The *Small* protocol (based on Small et al., 1999) is used for staining the cytoskeleton and optimised to get a stable actin staining. The second protocol was establish to stain mouse brain tissue, that was fixed by perfusion with formaldehyde. If further protocols were used, they are described in the corresponding section.

Cytoskeleton Staining   A cytoskeleton buffer is the base solution for this protocol and contains 10 mM MES, 150 mM NaCl, 5 mM EGTA, 5 mM glucose and 5 mM $MgCl_2$ and should be set on a pH of 6.1. The cells are washed with prewarmed PBS (1x, 37°C) and then fixed and permeabilised in two steps. First incubate up to two minutes with a solution of 0.3% (v/v) glutaraldehyde and 0.25% (v/v) Triton X-100 in cytoskeleton buffer (CB). For the second step the sample is submerged for 10 minutes in a 2% (v/v) glutaraldehyde in CB solution. To reduce the possible background due to fluorescent aldehyde groups, incubate the sample for 7 minutes with 0.1 % (w/v) sodium borohydride ($NaBH_4$) in PBS. Then wash the sample three times for 10 minutes with PBS. Introduce Alexa Fluor 647-phalloidin soluted in PBS to the sample and keep it for 24 hours at 4°C in the dark. The Alexa Fluor 647 phalloidin stock solution is 200 units/mL, which is equivalent to approximately 6.6 μM. Use 5 μL of the stock solution in 200 μL PBS for one well of a chamber. When immunofluorescence labelling of other cellular components (e.g. tubulin) is required, it is recommended that this process is performed first and actin is labelled afterwards, since phalloidin molecules may dissociate during the extensive washing steps. After labelling it is recommended to perform the measurements quickly. A post-fixation can be performed, but increases the probability of fixation artefacts.

Tissue Staining   The tissue is blocked for 30 minutes with 0.02 M glycine in PBS at room temperature to bind free aldehyde groups that would otherwise bind antibodies. To additionally reduce background the sample incubates for 1.5 hours in a blocking solution (1 % BSA, 5 % NGS in 0.3 % PBT). The primary antibodies incubate in blocking solution at 4°C overnight and are washed for 5, 5 and 90 minutes with PBS at RT. The incubation step with the secondary antibody in blocking solution takes 2 hours in room temperature, while keeping the sample in dark. The washing procedure of 5, 5 and 90 minutes with PBS at RT is repeated. For longer storage the sample is post-fixed with 4 % formaldehyde for 10 minutes. Before imaging the sample is stored in PBS at 4 °C.

Primary antibodies

Target	Specification	Conc.	Company
Anti β-tubulin	mouse mAb	10-20 μg/mL	Sigma T 8328
Anti α-bassoon	mouse mAb	5-10 μg/mL	Enzo Life Science SAP7F407
Anti bassoon	rabbit pAb	1 mg/mL (stock)	Synaptic Systems 152203
Anti BDNF mab9	mouse mAb	5 μg/mL	Yves-Alain Barde
Anti α-Ca channel (Ca$_v$2.1)	rabbit pAb	1 mg/mL (stock)	Synaptic Systems 152313
Anti Calbindin-D-28k	chicken pAb	5 μg/mL	Synaptic System
Anti Map2	chicken pAb	1 μg/mL	Abcam ab92434
Anti α-mGlu4	guinea-pig pAb	0.94 mg/mL (stock)	Shigemoto group
Anti Munc18-1	mouse mAb	1 mg/mL (stock)	Synaptic Systems 116011/6
Anti vGlut1	rabbit pAb	1 mg/mL (stock)	Synaptic Systems 116011/6

Secondary antibodies

Fluorecence marker	Specification	Conc.	Company
Alexa Fluor 532	goat-anti-mouse	10 μg/mL	Thermo Fischer A-11002
Alexa Fluor 532	goat-anti-rabbit	10 μg/mL	Thermo Fischer A-11009
Alexa Fluor 568	goat-anti-chicken	10 μg/mL	Thermo Fischer A-11041
Alexa Fluor 647	goat-anti-mouse	10 μg/mL	Thermo Fischer A-21237
Alexa Fluor 647	goat-anti-rabbit	10 μg/mL	Thermo Fischer A-21245
Alexa Fluor 647	goat-anti-guinea-pig	10 μg/mL	Thermo Fischer A-21450

TABLE 2.2: Primary and secondary antibodies used for fluorescence staining in fixed tissue and cells. Polyclonal and monoclonal antibody are abbreviated with pAb and mAb. If the concentration used in the following experiments varies the stock solution is inscribed and the used dilution is mentioned with in the experiment description. The concentration of the secondary antibody equals the standard dilution of 1:200. This concentration is used, if not otherwise stated.

2.1.3   Antibodies and Dyes

Most antibodies that were used are purchased commercially. In Table 2.2 the used primary and secondary antibodies are listed with their main specifications. Their reliability was tested in every case through specificity controls. Additionally for staining the cytoskeleton compound actin the drug phalloidin marked with the dye Alexa Fluor 647 was utilized. It was purchased from ThermoFischer GmbH (A22287).

2.2   Microscope Setups and Data Processing

2.2.1   Fluorescence Wide-Field Microscope

For localisation-based super-resolution microscopy such as PALM and *d*STORM experiments, two custom-built wide-field setups were utilised. The setup that was mainly used for two-colour measurements is described in the following. The second system is specialised on 3D measurements with the bi-plane approach as shown in Juette et al., 2008 and differs mainly in the detection pathway. All setups are placed on an air-damped optical table (Linos).

Excitation Pathway   All laser that are used in the main setups are listed in table 2.3. The laser beams are monochromised by a compatible bandpass filter with 10 nm bandwidth (Semrock, Clean-Up filter) and aligned on one pathway by a combination of dichroic longpass filters (Semrock, multiplex procedure LaserMUX-filter).

Laser	Specification	Output	Company
403 nm	Diode iBEAM-SMART-405-S	120 mW	Toptica Photonics
487 nm	Diode iBEAM-SMART-488-S-HP	200 mW	Toptica Photonics
514 nm	OPSL Genesis MX514-500 STM	500 mW	Coherent
558 nm	OPSL Genesis MX561-500 STM	500 mW	Coherent
640 nm	OPSL Genesis MX639-1000 STM	1000 mW	Coherent
641 nm	Cube 640-100C	100 mW	Coherent

TABLE 2.3: Lasers used for excitation on the dual-colour and the bi-plane setup.

For laser intensity density modulation three lenses are available to enlarge the excitation beam diameter. Subsequently the beam is focused by another lens on the back focal plane (BFP) of the objective. The position

of the beam focus can be modulated by a mirror to enable the alteration between TIRF (total internal reflection fluorescence), HILO (highly inclined and laminated optical sheet) and epi-illumination. A stable focus in the different excitation modi is ensured as all lenses and the mirror are installed on a coherent rail system with a micrometer screw modulation.

Microscope Configuration The stage system of the setup is the Olympus inverted microscope IX-71 is equipped with an oil-immersion objective (APON 60x, NA 1.49, N2709400 Olympus). A nose-piece (IX2-NPS, Olympus) is implemented to ensure a reduction of drift and vibrations by disconnecting the objective and the sample holder from the stage during an ongoing measurement. Dichroic mirrors are utilised to separate excitation and fluorescent light and are listed in table 2.4.

Specification	Company
dichroic mirrors	
ZT 405/514/635	Chroma
R442/514/647 band-elimination	Semrock
FF 410/504/582/669 BrightLine	Semrock
630 DCXR customized	Chroma
bandpass filters	
582/75 BrightLine	Semrock
679/41 BrightLine	Semrock
longpass filters	
LP 514 RazorEdge	Semrock
LP 647 RazorEdge	Semrock

TABLE 2.4: Main filters of the custom-built two-colour widefield setup.

Detection Pathway The same objective as used for illumination collects the fluorescent light. After transmission through the dichroic mirror the fluorescent light is filtered by an additional band-elimination filter. A telescope system of two lenses is introduced to the detection path way to obtain a pixel size in between 100-150 nm. Before the light is projected onto the detection plane, it is split spectrally. For the dual-colour approach a dichroic mirror (630 DCXR, compare table 2.4) was utilized. Two EMCCD cameras (Ixon DU 897; 512 x 512 pixel a 16 μm; Andor) ensure single molecule sensitivity. The two-camera imaging adapter TuCam (Andor) frames the setup of the detection pathway. For the bi-plane approach, enabling 3D-measurements, the dichroic mirror dividing the fluorescence signal spectrally is substituted by a 50/50 beamsplitter.

2.2.2 Structured Illumination Microscopy

Structured illumination microscopy (SIM) imaging was performed on a commercial ELYRA S.1 structured illumination microscope (Zeiss AG). The setup is equipped with four excitation lasers, a 405 nm diode (50 mW), a 488 nm OPSL (100 mW), a 561 nm OPSL (100 mW) and a 642 nm diode (150 mW). All SIM measurements were taken with a Plan-Apochromat 63x/1.40 immersion-oil based objective (Zeiss AG).
The setup can be operated by the software 'Zen' (black edition, Zeiss AG), including routines for e.g. individual settings, automated 3D imaging of chosen ROIs and image processing. The Zen software was mainly used for colour correction with a channel alignment tool and the structured illumination processing.

2.2.3 Super-Resolution Data Acquisition

All measurements acquiring super-resolved *d*STORM data are performed as described repetitivly in Linde et al., 2009; Heilemann et al., 2009; Andreska et al., 2014. The excitation intensity ranges in between 1-10 kW/cm^2 and is highly dependent on the utilised fluorophores and the label density. Furthermore the integration time is dependent on those parameters and varied in between 10 to 60 Hz.
To enable reversible photoswitching, the fluorophore needs to be exposed to an environment that contains thiol-groups promoting a reduction of the dye. Suitable switching buffer environments for several fluorophores are described in Linde et al., 2009. A typical switching buffer contains 100 mM β-mercaptoethylamin (MEA-HCl, Applichem). The pH is set fluorophore dependent in between 7 - 8.5 with a corresponding 5 M KOH dilution. In the publication Linde et al., 2011 a trouble shooting list for *d*STORM protocols is provided.

Two-Colour Measurements

In this work all two-colour measurements were recorded sequentially. Therefore the spectrum of the utilized fluorophores needs to be separated. Using different detection pathways and cameras, it is mandatory to align the two signals.
An extended description of performing two-colour *d*STORM is discussed in Aufmkolk, 2012 and Linde et al., 2013. Since the two-colour measurements are a key-technique of this thesis, a short acquisition work-flow is provided.

Data Acquisition with Sequential Two-Colour *d*STORM   To ensure a minimisation of cross talk for the utilised fluorophores, suitable chromatic mirrors and detection filters need to be introduced to the setup. Dichroic mirrors and detection filters used in the experiments of this thesis are listed in table 2.4.

A switching buffer has to be applied that offers suitable condition for both utilised fluorophores. For the combination of Alexa Fluor 647 and Alexa Fluor 532 a standard *d*STORM switching buffer of 100 mM MEA with a pH of 7.4-8.2 is used.

To enable sequential two-colour measurements the fluorescence emission of both fluorophores needs to be separated spectrally, in our case on two cameras. Note that the focal plane difference on the camera planes for the different wave-lengths need to be adjusted to each fluorophore pair.

To minimise photo-destruction effects the fluorophore, excited by the longer wavelength, is measured first and the read-out of the shorter wavelength excited dye is read out subsequently. It is important that in between these acquisition processes the focus is not changed, also not for possible axial drift effects. If this occurs, the data should be discarded, since the image set cannot be aligned to each other. However, an alignment is necessary due to chromatic aberration effects and variations in between the different optical elements in the corresponding detection pathway.

Channel Registration To align both detection channels, a registration sample, that shows the same pattern in the spectral range of both acquisition channels, is acquired. For this purpose a Tetraspecks sample (Fluorescent Microspheres, 0.2 or 0.5 μm diameter, ThermoFischer) is utilised. Arrange the Tetraspecks on your sample holder and check if both cameras are physically aligned on one pixel accuracy. Choose the excitation intensity in a matter that the fluorescence intensity is approximately the same on both channels. Record both channels simultaneously. Repeat the acquisition on different areas to ensure a high density of alignment marker in a reconstructed image of all Tetraspeck recordings. For the reconstruction of a super-resolved image, rapidSTORM was used. To create a localisation list of the Tetraspeck sample use exactly the same settings as they are used in the two-colour measurement reconstruction.

With the Fiji plugin bUnwarpJ a registration matrix can be evaluated. Therefore open the images of each channel signal and set five up to ten landmarks on different Tetraspecks visible in both images. Performing the registration bUnwarpJ creates an elastic transformation matrix that describes B-Spline polynomial functions estimating the distortion in between the images. This matrix can be translated into a raw transformation matrix. This pixel-to-pixel transformation can be read out by rapidSTORM. When using bUnwarpJ the direction of the transformation is chosen by defining one channel as source and the other as target image. Note, that the raw transformation utilised by rapidSTORM needs to be applied on the channel defined as target image.

A possibility to check the quality of this two-channel alignment is discussed in chapter 3.1.1.

3D Measurements

There are different approaches for three dimensional SMLM imaging. There is astigmatic imaging implemented by introducing a cylindrical lens to the detection path of the microscope. For further information I want to refer to the dissertation of Sven Proppert Proppert, 2015 and Huang et al., 2008a. Another approach is the multi-plane acquisition technique, where the fluorescence signal is split to multiple detectors, where every detector is focused on a distinct axial plane in the sample. Therefore you get simultaneously more information on the PSF of an object. This can be used to constrain the z position of the point source as shown in Juette et al., 2008. This approach was used for three-dimensional imaging performed for this thesis. To increase the accuracy of the 3D information gained in bi-plane measurements, an additionally approach, called temporal, radial-aperture-based intensity estimation (TRABI) by Christian Franke Franke, Sauer, and Linde, 2017 was applied in all tissue measurements.

2.2.4   Data Processing

rapidSTORM

The software rapidSTORM is used for the reconstruction of the SMLM raw data. A detailed description of its underlying algorithm and work-flows is given in Wolter et al., 2012b and the rapidSTORM manual Wolter et al., 2012a. rapidSTORM aims to identify sparsely emitting single fluorophores in sequences of images. Briefly explained, rapidSTORM identifies the number and position of the emission pattern of single fluorophores. The most likely fluorophore position is determined by a two-dimensional Gaussian fitting algorithm. The achievable precision is mainly dependent on the photon statistic of the signal. As a result a list of localisations is created and all localisations are summed up in a reconstructed high-resolution image. rapidSTORM supports the implementation of a transformation matrix to correct two-colour data sets for chromatic aberration. Linear drift correction is also feasible. Three-dimensional imaging is enabled by the computation of individual fluorophore's z-positions via the observation of shape changes in the point spread function. Both astigmatic and multi-layer approaches are supported. rapidSTORM is an open-source software and can be downloaded on the homepage of the Biotechnology and Biophysics department of Prof. Dr. Markus Sauer of the University of Würzburg. ($http : //www.super - resolution.biozentrum.uni - wuerzburg.de$)

Fiji

Fiji (Fiji is just ImageJ) is an image processing tool based on the open-source platform ImageJ that bundles several features that facilitates scientific image analysis. A plugin that is mainly used in this thesis is the registration tool bUnwarpJ to create a transformation matrix for aligning the spectral

channels performing two-colour dSTORM measurements. bUnwarbJ enables two-dimensional image registration applying an elastic deformation represented through B-splines.
The tool is explained on $http://imagej.net/BUnwarpJ$.

Locan Mathematica Script

Locan is a software package based on the Wolfram language Mathematica developed by PD Dr. Sören Doose. Locan implements various tools to perform localisation based analysis. The main features refer to the evaluation of intrinsical data properties as for example determining the experimental precision of the measurement, different approaches for cluster identification and analysis and comparison methods of two populations.
The data processing of the mGlu4 project is fully performed with this analysis tool and the utilized features are explained in the corresponding chapter.

coSIdSTORM

This software was developed to process and visualize the correlated dSTORM-SIM data. The basic program structure and details of the code are discussed in the bachelor thesis of Sebastian Reinhardt, who is mainly responsible for the programming work. This software is rudimentary based on vividSTORM, which is a open-source software for correlated confocal and SMLM image analysis facilitating the measurement of molecular abundance and was published by Barna et al., 2016.
We improved the software to higher processing velocity of large data quantities, which typically occur with super-resolution microscopy data. In our software we focused on the visualization of 3D data to facilitate orientation in dense biological structures as they occur in brain tissue. The application and detailed handling of coSIdSTORM is described in chapter 3.2.2 as it is a main part of the correlative SIM-dSTORM microscopy project.

Imaris

Imaris is a commercial Software distributed by Bitplane (Oxfords Instruments) that delivers visualisation and analysis tools for 3D microscopy data sets. It is used to render 3D SIM datasets. Further informations on Imaris is provided on the website $http://www.bitplane.com/imaris/imaris$.

Chapter 3

Results and Discussion

3.1 Analysis of Synaptic Proteins

Determining quantitative information about the molecular distribution and densities of synaptic proteins calls for a method that exhibits a precision capable of resolving the spatial relationship between single synaptic proteins. *d*STORM offers a spatial resolution of 20 nm. As described in the introduction many nanoscopic structures could have been unraveled with SMLM methods. In the following I will introduce two projects that investigate the organisation of synaptic affiliated proteins, the brain derived neurotrophic factor BDNF and the metabotropic glutamate receptor mGlu4. All measurements were performed as two-colour *d*STORM in two-dimensions by serial data acquisition as described in Chapter 2.2.3. For two-colour measurements it has to be stated that the achievable resolution highly depends on the photo-physics of the particular fluorophore. This and the accuracy of the channel alignment with Tetraspecks via bUnwarpJ should be described initially to the examples. One focus in this Chapter is drawn to the improvement of super-resolution data analysis. In the BDNF project the visualisation of endogenous concentration of BDNF was a novel achievement. The colocalisation with the presynaptic site could be solved on the base of image analysis and was facilitated through the flat structure of the neural culture. For the investigation on the mGlu4 receptor the analysis is more complicated, since we observe the distribution in brain slices. Here I will set the focus on the improvement of the analysis of single molecule localisation data. This is superior to image analysis performed on binned localisation data due to the processing of raw localisation data. The novel approach to this data is explained extensively.

3.1.1 Precision and Accuracy of Two-Colour *d*STORM

The precision of a localisation is indirectly proportional to the number of detected photons per on-state. Therefore the quality of the data depends highly on the chosen fluorophore. Here I compared the localisation precision of those fluorophores used mainly for the two-colour measurements with *d*STORM. To analyse the average experimental precision we use a nearest neighbourhood analysis based approach as described in Endesfelder et

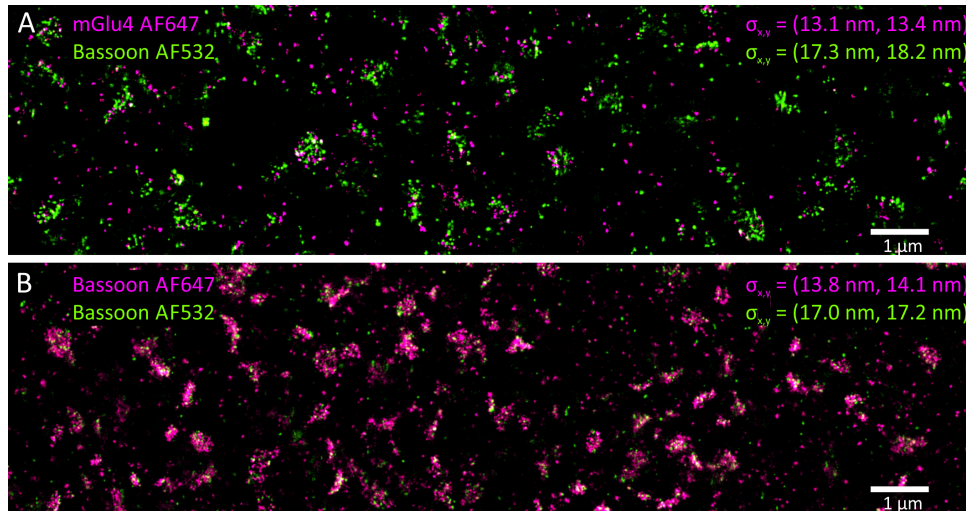al., 2014. The precision was estimated for two typical samples shown in

FIGURE 3.1: Precision estimation for *d*STORM images: For every fluorophore the precision in x and y direction is evaluated. A) The mGlu4 receptor was stained with Alexa Fluor 647 and Bassoon with Alexa Fluor 532 in the molecular layer of cerebellar brain tissue. B) In this tissue sample bassoon is labelled with two different antibodies and and secondary antibodies carrying also Alexa Fluor 647 and Alexa Fluor 532, respectively.

Figure 3.1. Both samples are cryo-slices of brain tissue and labelled via a primary and secondary antibody staining. Both times a precision of approximately 13 nm for Alexa Fluor 647 and 17 nm for Alexa Fluor 532 was evaluated. In the publication Ehmann et al., 2014 they compared the precision of Bruchpilot staining in the active zone cytomatrix in the Drosophila neuromuscular junction with Alexa Fluor 647, Alexa Fluor 700 and Alexa Fluor 532. They could measure a sigma of 14 nm (647), 35 nm (700) and 26 nm (532), which is comparable to my experiments. This suggests that the protein of main interest should be labelled with Alexa Fluor 647. All fluorophores still show a 10 fold improved resolution compared with the diffraction limit.

An important factor in the accuracy of two-colour data is the quality of the alignment of colours. We use mainly sequential measurements, where the signal of two fluorophores is split spectrally on two cameras. Due to chromatic aberration and slight differences in detection pathways, spheres filled with fluorophores (Tetraspecks by ThermoFischer) are detected on both cameras and are used to determine a registration matrix.
To proof that the alignment with Tetraspecks and the bUnwarpJ analysis is sufficient, I compared the localisation precision of the individual Tetraspecks images with the average nearest neighbour distance of the centroids of respectively the Tetraspeck signal on camera 1 and on camera 2. An alignment should be used just for the next follow-up sample, since the error of the alignment increases drasticly with time, immersion oil changes and most
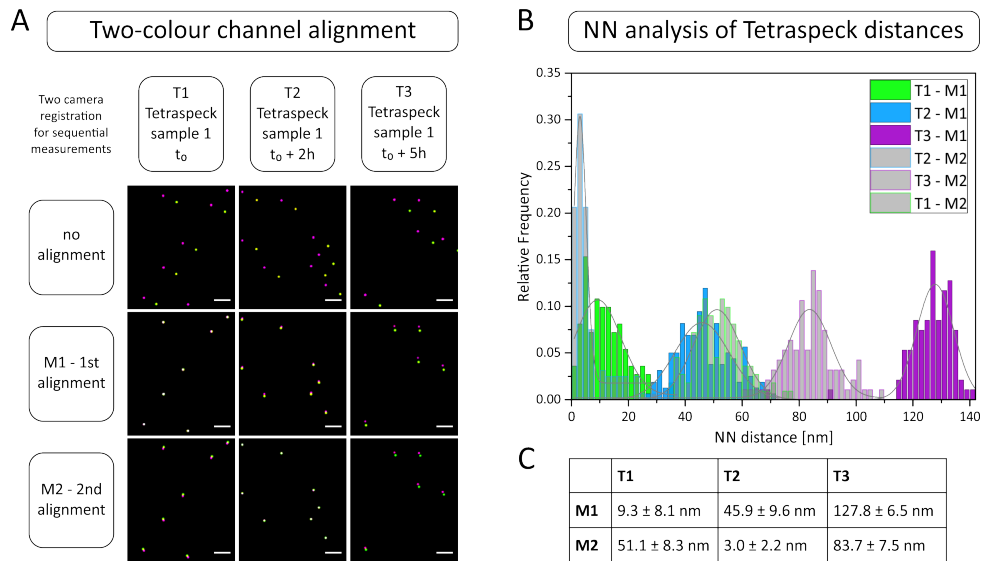
FIGURE 3.2: Test of alignement accuracy. A) Three alignment measurements with Tetraspecks (T1-T3) were taken on one measurement day. An alignment matrix optimised for two samples (M1 for T1 and M2 for T2) is used for all samples respectively and subsets of the resulting two-colour images are presented. Note that the Tetraspeck images are blurred (Gauss-function $\sigma = 14$ nm) for better visibility. Scale bar 500 nm. B) Nearest neighbour distances for each magenta and green Tetraspeck couple are evaluated and plotted for each T-M combination. The distributions are fitted with a Gauss-function and the peak values $\pm$ the sigma of the Gaussian fit are listed in C).

critical re-focusing with the nose-piece (compare setup description in Chapter 2). The nose-piece stabilises the sample holder and objective combination and prevents drift, though the focus thread seems to lead to a linear offset, when used. This is of course a very setup specific error.

To test these scenarios I used a set of alignment measurements of a normal measurement session. The first alignment measurement (T1) was performed at $t_0 = 0$ and prepared for the focus plane of the sample of interest. After changing the sample and refocusing I performed a second alignment (T2) at $t_1 = t_0 + 2h$. Before the next alignment (T3) at $t_2 = t_1 + 3h$ I changed the sample and therefore oil and focus twice. For the accuracy test I created an optimised transformation matrix (M) for T1 and T2 and applied M1 and M2 on each alignment sample. In Figure 3.2 A are the results for this experimental setup shown. The different combinations are named $T_i - M_i$ dependent on the Tetraspeck sample and the applied matrix.

To identify localisation cluster belonging to one Tetraspeck I used the alpha-shape cluster-finding algorithm with the variable set as $\alpha = 10$. Afterwards a nearest neighbour analysis of the centroids of every cluster displays a distance that describes the precision of the alignment. In frame B the distribution of the nearest neighbour distances of every alignment scenario is plotted. The peaks of the distance distributions are fitted and the peak-values

with the sigma of the Gaussian fit are listed in C. Ideally the alignment matrix has an accuracy of 3 up to 9 nm as evaluated for T1-M1 and T2-M2. As soon as strong refocusing via the nose-piece or after a longer measurement period is proceeded, the alignment accuracy decreases drastically. This process can be a tool to control the quality and accuracy of every taken alignment measurement. But also might be helpful to evaluate the stability of the experimental setup itself.

If an alignment matrix is created on a regular base the error of the alignment lies well below the *d*STORM precision. With this strategy we can still claim a precision of approximately 20 nm for two-colour *d*STORM images.

3.1.2   Project BDNF

To identify the nanoscopic distribution of the brain-derived neurotrophic factor (BDNF) in hippocampal neuron cultures, we performed two-colour *d*STORM measurements in mature cultures. We just used cultures older than two weeks (> 14 div). BDNF antibody testing is crucial for the reliability of fluorescent measurements, particularly for highly sensitive methods . Various test and controls to ensure the quality of the labelling and cell culture were performed and are described extensively in Andreska et al., 2014. The focus of my thesis lies in the analysis and execution of the *d*STORM data. This also was the main contribution to that paper.

Identification of the Synaptic Scaffold Structure

Initially to our experiments we wanted to prove that we are capable to resolve the synaptic scaffold structure with *d*STORM. Furthermore we could verify suitable markers to test our hypothesis that BDNF is correlated with the pre-synaptic site in hippocampal neurons. In Figure 3.3 super-resolved images of double-stained hippocampal neurons with immunocytochemical tags are displayed. The synaptic scaffold proteins Bassoon and Homer are visualised as dense molecule bar-like structures, separated by the synaptic cleft. In a complete neurological network we expected that every post-synaptic structure has a pre-synaptic counterpart, though some Homer bars occur without Bassoon signal (cyan arrows). The vGlut signal is fenced by Bassoon signal and marks the complete pre-synaptic site, while Bassoon is concentrated in the active zone.

Super-Resolved BDNF Distribution at Synapses

Hippocampal cultures contain glutamatergic and GABAergic neurons. For this reason we tested BDNF immunoreactivity (IR) at both kinds of synapses. While vGlut was homogeneously distributed in theses synaptic areas, BDNF IR appeared in densely packed, immunoreactive clusters visualised in Figure 3.4 A. This reveals that BDNF IR can be found in close proximity to vGlut+ synapses, and overlaps with vGlut IR signal (magenta arrows). We
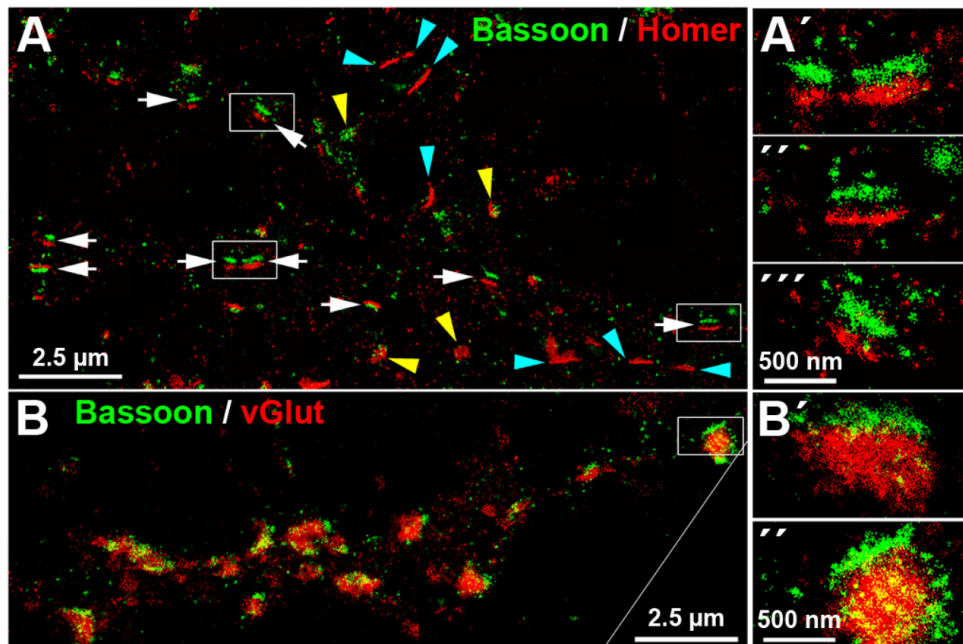
FIGURE 3.3: A) Pre-synaptic Bassoon and post-synaptic Homer can be well separated by *d*STORM imaging and the synaptic cleft is revealed. The juxtaposed bar structures (white arrows) occur just in mature neurons (DIV 35). Elliptical disk-like cluster may represent front-view synapses (yellow arrows). Some Homer bars lacked a pre-synaptic counterpart (cyan arrows) and might indicate non functioning synapses. (B) Bassoon and vGlut are in tight association. The close-up images, a front of a side view of a synapse, reveal that the pre-synapse is delineated by vGlut. Therefore vGlut serves as a good pre-synapse indicator. (Image adopted from Andreska et al., 2014; permission granted.)

never found accumulation of BDNF IR in synapses positive for the vesicular GABA transporter (vGAT; Figure 3.4 B). Neither vGAT enriched synapses close to BDNF enriched somata, nor vGAT-positive structures in peripheral neurites showed a substantial BDNF label (cyan arrows). In subset A and B the same area is visualised and for a better comparability cyan arrows point to vGAT-enriched/BDNF-poor synapses and magenta arrows towards vGlut-enriched/BDNF-enriched synapses. Colocalisation analysis of confocal z-stack data was determined with the mean Pearson's coefficient ($r \pm$ SD) for pixel based analysis as described in Costes et al., 2004. Anti-BDNF and anti-vGlut labels showed a non-random correlation (Pearson's correlation coefficient $r = 0.24 \pm 0.04$ SD, $n = 9$) of overlapping structures. In contrast, no correlation was seen between anti-BDNF and anti-vGAT labels ($r = 0.01 \pm 0.01$ SD, $n = 9$). This value was equal to the correlation coefficient comparing vGAT and vGlut labels ($r = 0.01 \pm 0.01$ SD, $n = 9$). The data suggests that BDNF is mainly pre-synaptic, though the resolution is not efficient enough to identify exactly the affiliation or possible sub-structures. Two-colour *d*STORM experiments were performed as described in 2. After

an initial screening procedure, we found Alexa Fluor 532 for BDNF label-
ing and Alexa Fluor 647 for synaptic markers to be a potent combination
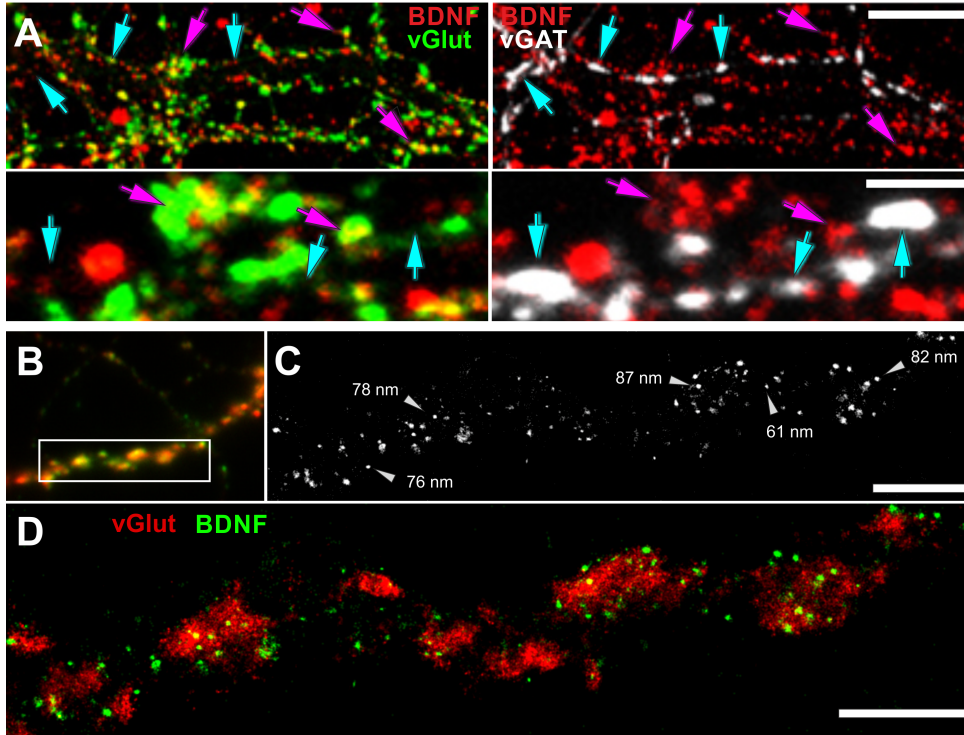for the *d*STORM imaging. On average we acquired 40,000 frames for an

FIGURE 3.4: (A) Function indicates that BDNF is present at glutermatergic
synapses. Therefore we performed confocal imaging of BDNF and vGlut
(left) . As a control for the contrary hypothesis in (right) of BDNF and
VGAT. Though LSM does not provide spatial resolution to obtain infor-
mation if BDNF is concentrated in glutermatergic terminal. (B) Epifluores-
cence of a hippocampal neuron (DIV 35) confirm strong labelling of BDNF
(green) and vGlut (red). The inset in the widefield image is displayed as
a super-resolution reconstruction in (D). (C) BDNF granules occur with a
diameter in the range of 60-90 nm. (D) Single granules of BDNF are iden-
tified in close proximity to vGlut. (Image slightly modified from Andreska
et al., 2014)

image, while measuring the different wavelengths sequentially. For pho-
toswitching a PBS-based buffer containing 100 mM β-mercaptoethylamine
(MEA) adjusted to pH 8.0–8.3 was used (Linde et al., 2011). Experiments
were performed by TIRF illumination to reduce background. The images
were reconstructed with the Software rapidSTORM.
In Figure 3.4 C the BDNF granule distribution is revealed with a resolution
of 20 nm. BDNF assembles in close proximity to vGlut in synapses (D),
though a direct colocalisation is not a priori visible. To define a BDNF gran-
ule, I performed a imaged-based analysis to create a binary mask for the area
occupied by BDNF. All operations were performed with the open-source
Software ImageJ. A Gaussian blur with a sigma of 10 nm (proportional to

our resolution) was applied. A threshold with a pixel value of 0.25 to account for the fact that the rapidSTORM algorithm divides a localisation that is not exactly in the middle of a pixel evenly on four pixels is set afterwards. This pixel value occurs when the localisation is exactly located in between four pixels. This threshold is just valid, if the measurements are background free. After the transformation of intensity values to binary, the area of interest is selected with a mask. To exclude sparse localisation a grayscale image in which the gray value is equal to the exact number of localisations per pixel was created.
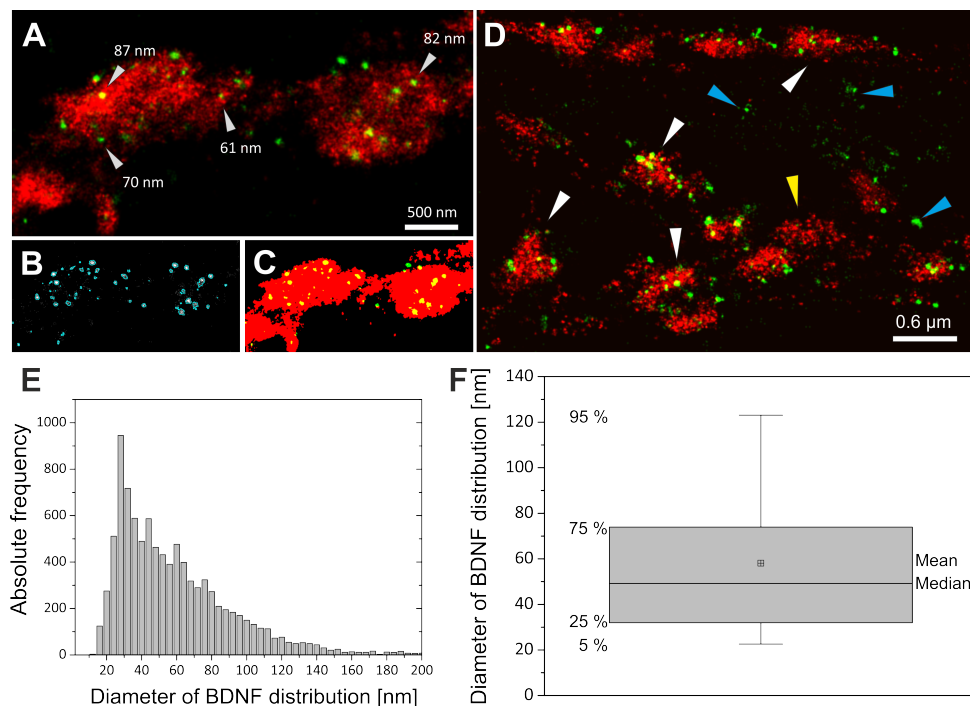

FIGURE 3.5: Quantitative analysis of BDNF granules: A) The BDNF localisations in the the vGlut structure appear as well-seperated granules. B) The BDNF distribution is identified by a localisation mask. C) The greyscale information is transfered to a binary information to analyse the area overlap of BDNF and vGlut without being compromised by different intensity dependency of both populations. Here, 91 % of all BDNF localisations colocalise with the vGlut signal. D) vGlut synapses contain densely packed BDNF+ vesicles (white arrows) and vGlut+ discs with low amount of BDNF+ vesicles (yellow arrowhead) were found in close neighbourhood. Accumulation of BDNF+ vesicles was also seen at vGlut-negative sites of unknown origin (cyan arrowhead) (here DIV 30). D) Histogram of the diameter of all BDNF localisation points. The selection mask (B, cyan mask lines) defines the size (pixelarea) of BDNF vesicles. Assuming that those are approximately circular yields to a mean diameter of 58 nm and a median diameter of 49 nm (n = 9562 BDNF localisations clusters). F) Boxplot diagram of E), box defines 1st and 3rd quartile and the whiskers the 5th and 95th percentile.(Image adopted from Andreska et al., 2014)

The BDNF mask was applied to this data (Figure 3.5 B - cyan mask) and all cluster with less than 2 localisation were excluded. As the BDNF localisations formed almost spherical image elements, we determined the diameter of BDNF IR clusters as $d = 2\sqrt{Area/\pi}$. The mean diameter of all BDNF clusters was determined as 58.2 nm ($\pm$ 0.4 s.e.m.; n = 9562 clusters, analyzed from 17 *d*STORM images of 4 cultures). Histogram and Box-plot diagram of the data is visualised in Figure 3.5 E and F.

vGlut disc-like synaptic structures are formed by multiple, small spherical localisation clusters. To identify the overlap in between BDNF and vGlut, we created a binary mask as described before for vGlut. Herewith two cluster areas were considered as overlapping when the distance between the localisations in the x,y-direction was less than 20 nm. This distance was set via the border criterion of the mask and corresponded approximately to the spatial resolution achieved in our experiments. The evaluation of the area overlap of BDNF and vGlut masks equals the colocalisation value. In all measured cultures the amount of BDNF per vGlut-enriched synapse differs significantly. In Figure 3.5 D different constellation are marked. Exemplary vGlut negative / BDNF positive clusters are signaled with cyan arrowheads. Some vGlut+ discs with low numbers of BDNF+ localisations exist in close neighbourhood to synapses with high BDNF IR (yellow arrowheads). On average, 39.4 % of all BDNF localisations in all two-dimensional *d*STORM images of neurites overlap with immunoreactivity masks of vGlut (data of 12 *d*STORM images; collected from 3 cultures). If we focus on synapses that contain both signals, for example in Figure 3.4 D the overlap of BDNF clusters with the vGlut counterstain is 88.4%, in Figure 3.5 A even 91%. Remarkable is when vGlut-enriched disc-like synaptic structures are not too dense, so that multiple, small spherical localisation clusters can be resolved (compare Figure 3.5 white arrowheads), we can observe, that BDNF and vGlut granules are not completely co-localised, but occur in a distance of a few nanometer.

To countercheck that BDNF is not affiliated with the post-synaptical site, we perform a double-staining of BDNF and homer. In Figure 3.6 we see homer (red) forming bar like structures representing the active zone of the post-synapse.

Just some rare cluster of BDNF align along those structures. This colocalisation might be caused through the projection of the three dimensional structure, so the angle of view on the synapse leads to a misinterpretation and therefore false positive correlation values. As described in Andreska et al., 2014 we prefer the interpretation that these vesicles represent endosomes that are transcellularly filled from the BDNF-rich presynaptic part, probable via endocytosis together with post-synaptic TrkB receptors (Kohara et al., 2001; Lazo et al., 2013; Orefice et al., 2013).

A future challenge will be to find out whether or not BDNF is mainly released at the active zone or equally distributed over the synapse. All data in this publication suggests that BDNF protein is most likely formed in the somatic compartment and brought to the glutamatergic pre-synapse by
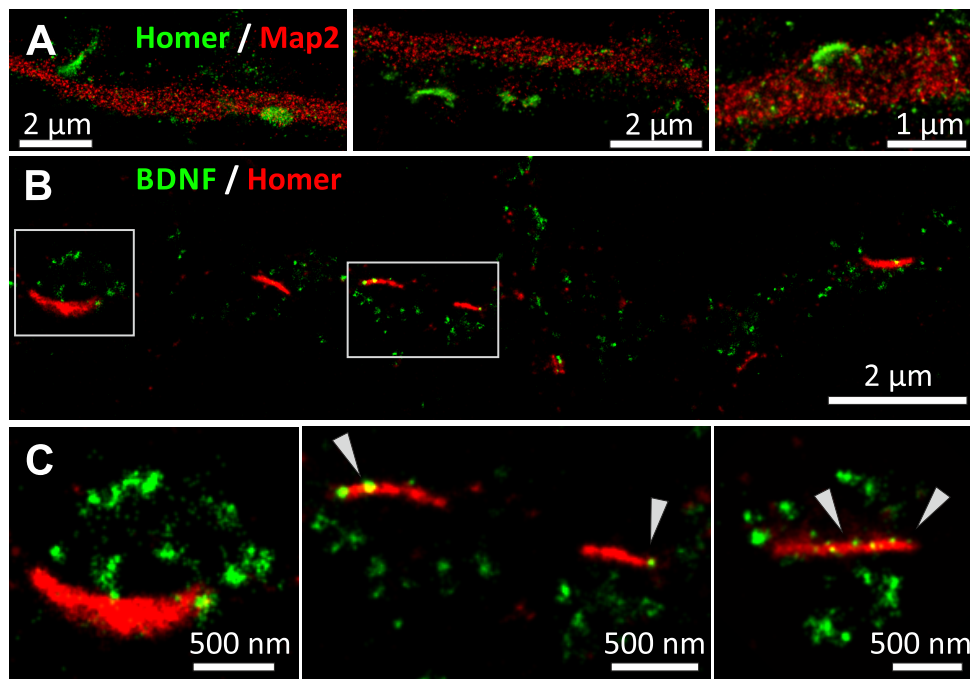
FIGURE 3.6: *d*STORM images of BDNF with postsynaptic staining. A) Post-synaptic active zones, marked my homer (green) are assembled along, but not within Map2 stained dendrites. B) Super-resolved image of homer (red) and BDNF (green) in mature hippocampal neurons (DIV 30). BDNF is accumulated in close proximity to the postsynaptic structures, though just 6.7% of the BDNF granules are found in contact with the homer structure. C) In the detailed cut outs some small BDNF granules are marked that overlap with the post-synaptic bar-structures, while the vast majority of BDNF signal is departed of the homer staining.

anterograde transport. Further experiments to investigate potential transportation vesicles or partners like cromogranin are of interest.

A critical point on this analysis is that we projected a three-dimensional problem into two dimensions. The orientation of the synapse was neglected. Still we considered this method valid to this case, since the sample structure was flat and we could perform the measurements with TIRF-illumination. For samples with an extended axial dimension or higher background signal colocalisation tests need to be improved.

3.1.3 Project mGlu4

In the previous section we could show the affiliation of BDNF with the presynapses by a two-dimensional area comparison. Though a strength of single molecule localisation microscopy is that we can process directly the raw data material without bothering to use image analysis tools. Here I show the improvement of tools for cluster and colocalisation tests applied on the investigation of the metabotropic glutamate receptor mGlu4. The cluster and correlation approaches were processed with the mathematica user interface

locan, which was programmed by PD Dr. Sören Doose. Locan offers localisation based analysis of two and three-dimensional data sets.

In this project we seek insights on the distribution of the metabotropic glutamate receptor mGlu4 and its affiliation with components of the presynaptic active zone. This is a cooperation with the group of Prof. Davide Calebiro.
The mGlu4 receptor could be a promising target for neuropsychiatric disorder investigations, since G-protein coupled receptors (GPCRs) are a key-element in the modulation of synaptic transmission. In the cerebellum it has a depressive effect on the parallel fibre to Purkinje cell excitatory transmission. This effect is partially mediated via inhibition of the synaptic calcium influx which regulates glutamate release.
Some studies already showed the distribution of the mGlu4 receptor along the presynaptic membrane of parallel fiber synaptic terminals in the cerebellar molecular layer on rats with a pre-embedding immunogold method (Mateos et al., 1999), though the information on interactive distribution of mGlu4 and other components of the active zone are limited. With dual-colour (dSTORM) experiments we aim to directly analyse the nanoscopic organisation of mGlu4 receptors at the synapse between parallel fibers and Purkinje cells in the cerebellum. To be more specific we perform imaging on 1.5 - 5 μm thick cryoslices of a with 4% PFA fixed mouse cerebellum. With dSTORM visualisation of direct immunolabelling of the endogenous protein concentrations we enable distributional analysis in the cellular context of the molecular layer and in the following I reveal estimations on the density of mGlu4 in the pre-synapse.
In my thesis I emphasize the methodological approach of analysing this super-resolved data sets and concentrate on the explanation of applied analysis approaches.

Identification of a Clustered Distribution

To create a first overview of how different potential interaction partner of the mGlu4 receptor are allocated in the sample, we want to test if the targets are homogeneously distributed or clustered in any way. In the following I present different methods of cluster analysis on those various targets and set them into context to the receptor.

General Cluster Test by the Ripley's H Function   The Ripley's H function is normalised on a arbitrary distribution equalling zero and provides hints on length scales on which clustering or anticlustering occurs. I investigated the function for following target: mGlu4 as main target, Bassoon as active zone protein, Munc18 as essential component of the synaptic vesicle fusion protein complex and the voltage-gated Calcium channel $Ca_v2.1$. In Figure 3.7 B the evaluated functions are plotted. To set the gained data in to context a random distribution (green) and a Neyman-Scott distribution (pink).
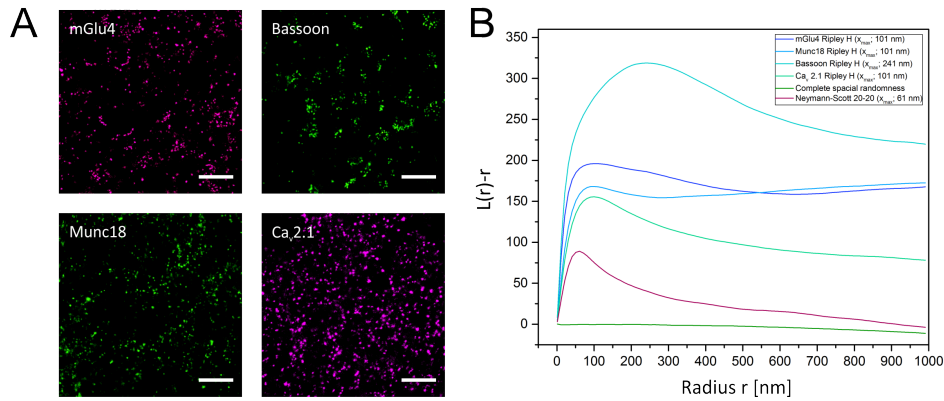
FIGURE 3.7: General cluster test by the Ripley's H function: A) *d*STORM images of synaptic proteins that where analysed in this project. Scale bars 1μm. The graph B) shows the Ripley H distributions of the proteins Bassoon, mGlu4, Munc18 and the calcium channel subunit Ca$_v$2.1.

The Neyman-Scott process forms cluster, where the mean number of points per cluster and the spread of that daughter events can be determined. Typical every fluorophore blinks several times in a *d*STORM acquisition process, therefore a point signal contains often several localisations. Defining a Neymann-Scott process with 20 daughter points per cluster event and a sigma of the probability density function of 20 nm, we can mimic a distribution similar to the main target distribution of mGlu4. This distribution gives a peak around 60 nm for the Ripley's H function. The distribution of mGlu4, Munc18 and the calcium channel are similar and form a peak, showing clear signs of clustering at small radii. In contrast to the Neyman-Scott simulation the peak is shifted to a sigma of approximately 100 nm, which indicates a slightly bigger cluster and can be influenced for example by active zone clustering. For the mGlu4 distribution an extended shoulder shifted to higher radii is noticeable and gives a hint for another cluster population, which resembles the distribution of Bassoon. Bassoon shows higher order clustering, identifying the pre-synapse, shown by a prominent shoulder of the Ripley's H function shifted to higher radii compared to the other distribution.

Analysis of the mGlu4 Receptor Distribution   mGlu4 signal occurs as clusters with hypothetical denser accumulation at the active zones. Ripley's H analysis of the localisation data of mGlu4 as shown before suggests that there are two populations of clustering. A smaller one that could represent a single receptor and the accumulation at the active zone. To analyse the receptor signal and therefore the small cluster population better, a reliable cluster finding parameter needs to be evaluated. Additionally the label-density needs to be optimised and therefore we titrated the primary and secondary antibody solution.

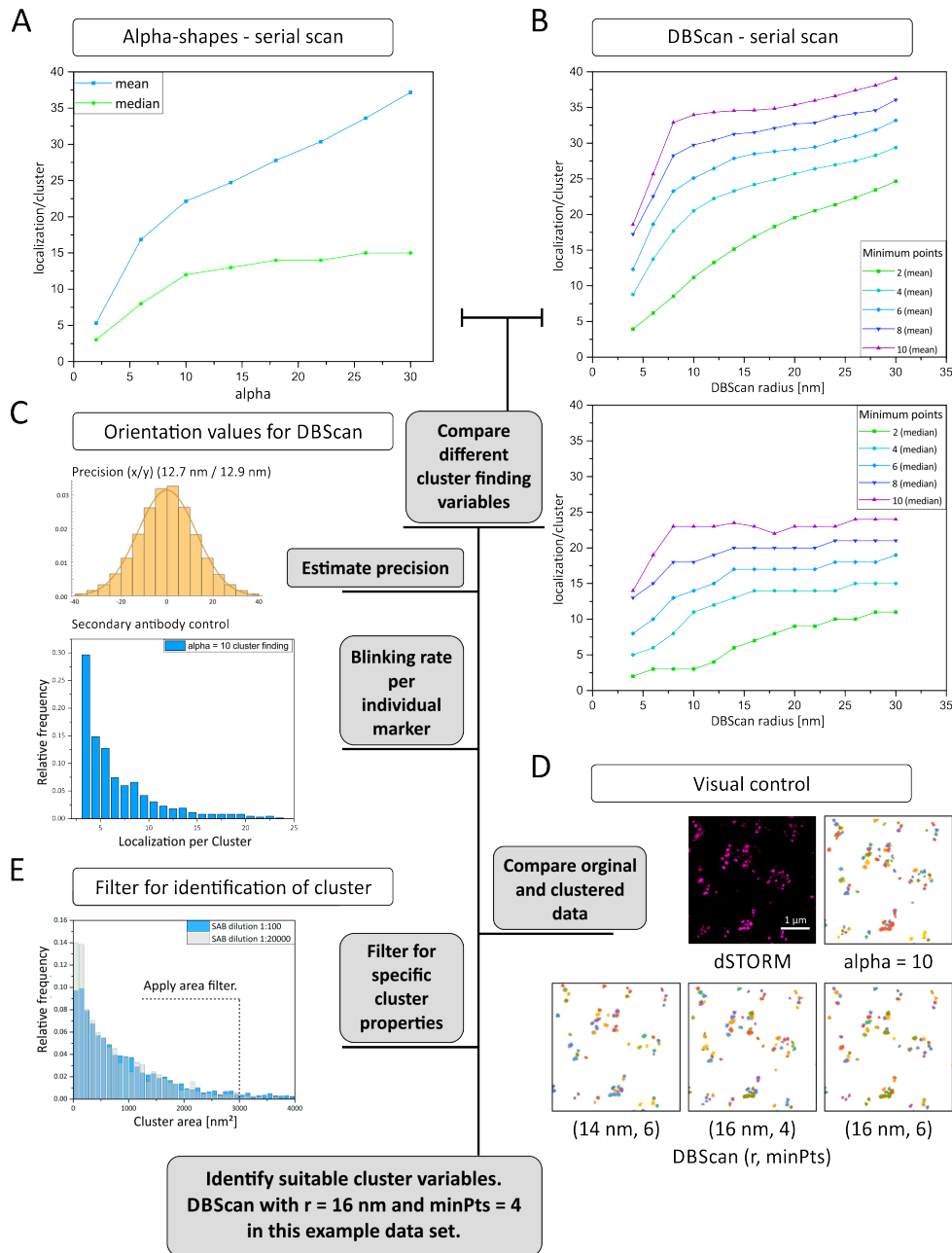In Figure 3.8 I describe which possibilities are given and which factors have

FIGURE 3.8: Parameter evaluation for cluster finding on the example of a mGlu4 staining: A) Alpha-shape analysis was performed for various alpha. For every alpha the mean value for localisation per cluster and the corresponding median is plotted. B) For the DBScan serial analysis the various parameter for the scan radius and the minimum points per area were tested. The mean value for the localisation per cluster distribution for the different parameter and the corresponding median are plotted in individual graphs. Peculiar forms of the line diagram like plateaus pinpoint an area of suitable cluster parameter. C) For the DBScan analysis the precision gained with the specific staining and the number of localisation measured per single marker are additionally good orientation points for finding suitable parameter for the radius and the value for minimum points. D) Visual control by comparing the data with the evaluated clusters seems helpful if not a distinct parameter is determinable. E) A filter for specific cluster properties should be applied. In this case the area was confined to discard larger accumulations. An histogram over the cluster area sizes for a very dense and a coarse staining gives an orientation for a suitable area range.

to be taken into account to find suitable parameters for identifying the cluster of interest.

As an example and for being the main protein of interest the parameter finding process is shown for the mGlu4 data. For the investigation on this receptor population I performed a serial scan of different parameters for BDScan analysis and α-shape cluster finding. On both correlation curves (Figure 3.8 A and B we can not distinguish a variable that fits best to the mGlu4 population at first sight, though a slowly increasing plateau is identifiable after an α-value of 10 (A) for the median of the number of localisations per cluster. The median is not so much effected by cluster connections that easily occur due to background or dense structures, and therefore the cluster algorithm combines cluster areas. These outliers increase on the other hand the mean value rapidly. For the DBScan there are two parameters of connectivity that determine a cluster, a minimum number of neighbours $minPts$ (minimum points) and the radius r. In the serial scan of different minPts and radii no obvious parameter pair is identifiable, though similar to the α-shape approach a plateau is confining the radius parameter at a range of 10 to 20 nm. The DBScan is favourable due to its fast performance and a robust calculation while excluding sparse localisations and will be used mainly for further analysis.

In Pageon et al., 2016 the median localisation precision is suggested to be a good starting point for choosing the radius for a DBScan. With a precision of approx. 13 nm for this test sample, the radii parameter of 14 nm and 16 nm were checked further. For the minPts comparision it is of interest to know the minimum output of one marker. As smallest labelling chain-link I estimated the localisations per secondary antibody by measuring single secondary antibodies in a standard sample environment, in our case on a brain slice. With a median of eight localisations per secondary antibody a orientation point for the minPts is set. With a slightly overestimated radius and underestimated minPts I compared the cluster findings of some parameters with the source data (D). Having a natural diversity of cluster sizes in the biological sample influenced through measurement parameters, like unresolved dense spots or background, the parameter can just be optimised to a certain degree and some filter specific for the cluster properties should be applied. In this case being interested solely in single receptor cluster, accumulations in dense areas should be excluded. In Figure 3.8 E) I histogrammed the area sizes of found cluster of mGlu4 acquired via two measurements stained with different antibody concentration to identify an area range. Smaller areas than 100 nm^2 are considered as unspecific bindings and areas bigger than 3000 nm^2 as connected receptor cluster. Assuming a round cluster an area of 3000 nm^2 equals a radius of 31 nm, which is already a progressive upper boarder estimation.

Overall the parameter of α = 10 for the α-shape algorithm and r = 16 nm with 4 minPts were estimated as reliable values to identify the mGlu4 cluster distribution. These values are used for all further evaluations.
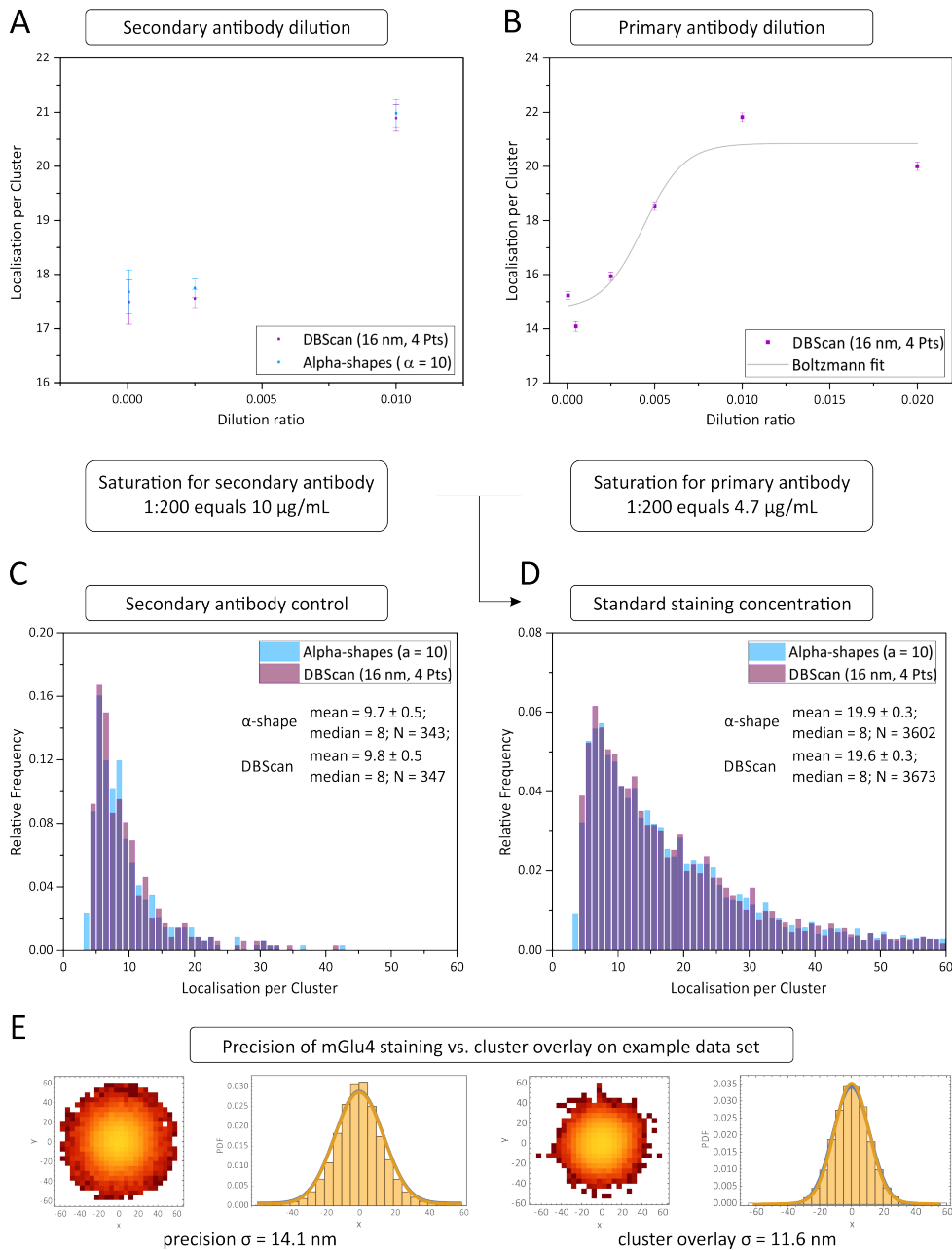
FIGURE 3.9: Antibody dilution tests and quantification of the mGlu4 receptor. A) Localisations per mGlu4 cluster plotted over three secondary antibody dilutions. The error bars describe the standard error of the number of localisations per cluster. This coarse estimate led to a preferred dilution of 1:200 (10 μg/mL) to work with in following experiments. B) Titration experiment of six dilution variation for the primary antibody against the mGlu4 receptor. The number of localisation per cluster reach a plateau after a 1:200 dilution. To minimize costs and background by unspecific binding, yet still have a saturated staining a final concentration of 1:200 is used as the standard parameter. C) Relative frequency histogram of localisation per cluster for a secondary antibody control (no primary antibody). D) Histogram as in C for the standard concentration parameter. The sample preparation and measurements for C and D were performed on the same day with the same sample batch. E) Comparision of experimental precision of the mGlu4 staining with AF 647 and an overlay of the found receptor cluster. The distribution were fitted by a normal distribution to estimate sigma.

In order to estimate the optimal antibody dilution for a mGlu4 staining we performed a titration experiment. It is desirable to have a saturation of all epitopes, but minimize the usage of antibodies due to an increased probability for unspecific binding. For the secondary antibody we performed a coarse titration with three measurement points to estimate a saturation concentration. In Figure 3.9 A the mean value of the localisations found per cluster is plotted over the dilution ratio, which is defined as the relative concentration of the stock solution. For the maximal concentration of 1:100 we found full saturation, while a dilution of 1:400 is almost on the level of a minimal dilution of 1:20000. Both cluster finding algorithm show the same distribution with errors. In the follow-up we use a dilution of the Alexa Fluor 647 goat anti guinea-pig antibody of 10 μg/mL (1:200) which is assumed close to saturation. The saturation value of the primary antibody dilution row of approximately 21 localisations per cluster affirms this assumption. For the primary antibody concentration curve we performed six different dilutions. The used primary antibody was a polyclonal guinea-pig anti αmGluR4 in a stock concentration of 0.94 mg/mL provided by Prof. Dr. H. Shigemoto. In Figure 3.9 B) the number of localisations per cluster (mean value) is plotted over the dilution value. A saturation was approximately reached with an primary antibody concentration of 4.7 μg/mL (1:200).

In addition to the optimisation of the staining conditions, titration experiments can help to gain quantitative informations about the glutamate receptor configuration. The question is whether it is possible to gain information about the presence of the mGlu4 receptor in a dimerised form in the parallel fibers.

GPCRs exist as homer and hetero dimers. Although it is highly discussed if GPCRs always function as dimer or not (Gurevich and Gurevich, 2008), it is agreed on that class C receptors exist as stable dimers as described in Kunishima et al., 2000 and Muto et al., 2007. Newer findings in Kammermeier, 2012 suggest also hetero-dimerisation.

It would be advantageous, if it is possible to count the number of receptor epitopes in one cluster. Since reversible switchable fluorophores are located several times in one acquisition session, we need to normalise the data on the number of localisations that are expected on one receptor. For the primary antibody the receptor has theoretically four binding epitopes, although it is questionable that all epitopes are reachable at the same time. Every primary antibody (PAB) can bind up to two secondary antibodies (SAB). One secondary antibody can be labelled with several fluorophores. A standard value for a commercial secondary antibody is 3-4 dyes per antibody. We used the same charge of secondary antibody with a degree of labelling (DOL) of 3 for all experiments. The amount of localisations that is detectable for one labelling cascade of primary and secondary antibodies and dyes possesses a high variance.

For an eventual quantification I fitted the primary antibody concentration with a Boltzmann function and estimated a minimum plateau of 14.7 $\pm$ 1.3

(SE) localisations per cluster and a maximum value of 20.8 ± 0.8 localisations. To estimated the number of localisations gained of a single secondary antibody, we stained our sample with the standard protocol not providing a primary antibody. The amount of unspecific binding was very low, although we could use the sparse localisation events from single secondary antibodies in a comparable environment to our normal experiment. The target was identified with alpha-shapes (α = 10) and DBScan (16 nm radius, 4 minPts) applying an area filter (100 - 3000 nm^2). As shown in figure 3.9 C) the amount of localisations per cluster was evaluated to be of 9.7 ± 0.5 nm (number of cluster N = 343) respectively 9.8 ± 0.5 nm (N = 347). To set this in comparison to a complete staining I measured samples with a saturated antibody concentration and the same switching buffer in a brain slice on the same day. Here we can identify 19.9 ± 0.3 nm (α-shapes; N = 3602) respectively 19.6 ± 0.3 nm (DBScan; N = 3673) localisations per cluster (Figure 3.9 D). These values are consistent with the saturation curve values.

Having a minimum localisation value for the primary antibody of approximately 1.5 as much as the single secondary antibody value, we can assume that with a saturated concentration one or two secondary antibodies are bound per primary antibody. For a fully saturated staining we evaluate not even a factor two of localisations per cluster (Compare Figure 3.9). This experimental data suggests the conclusion that we have no dimers.

However, these factors do not allow a safe conclusions, since the wide distribution of the labelling cascade strongly influences statistics. Therefore we can not suggest an identification of a homo- or hetero-dimerisation concept. This example makes abundantly clear where the limitations of counting with *d*STORM lie, when using standard immunohistochemistry protocols. Quantification can be better enabled using direct markers. For example a combination of directly tagged primary antibodies with a DOL of 1 combined with titration experiments could facilitate counting as shown in Ehmann et al., 2014. Also attaching the dye with a small peptide or protein-tags like SNAP or FLAG tag decreases the variance of localisation events per target. However these approaches need to be prepared individually for each experiments and are not available for a lot of targets.

Another idea was to evaluate a hint on dimerisation by comparing the size of the cluster by overlaying several cluster distributions with the gained precision of our measurements (compare Figure 3.9 E). If the cluster size lies above the precision limit, estimations could be made if a dimer is present or not. The values shown in E) are evaluated from the same data set analysed in D) with the optimised staining conditions. With an estimated precision of 14 nm and a sigma of the distribution of the overlaying cluster of 12 nm the information is blurred in the resolution limit. Note that the smaller sigma of the cluster distribution can be a result of the chosen cluster parameter and is equal to the precision value with regards to errors. Assuming a distance of two dimerised proteins of 2 nm and a distance of the marker of 14 nm due to the primary and secondary antibody connection, the resolving distribution has a dimension around 30 nm. Any spatial information in this range

vanishes exactly in the estimated precision of 14 nm. This analysis offers therefore no extra information of the question of dimerisation, though interactions of proteins on a length scale above 30 nm can be addressed with *d*STORM and makes this method superior in spatial analysis compared to other super-resolution techniques.

Comparision of two Populations - mGlu4 to Active Zone Proteins

A better understanding of the receptor location and distribution could emphasize certain models of the underlying molecular mechanism. Two-colour measurements can reveal the correlation of the mGlu4 receptor with other synaptical components.

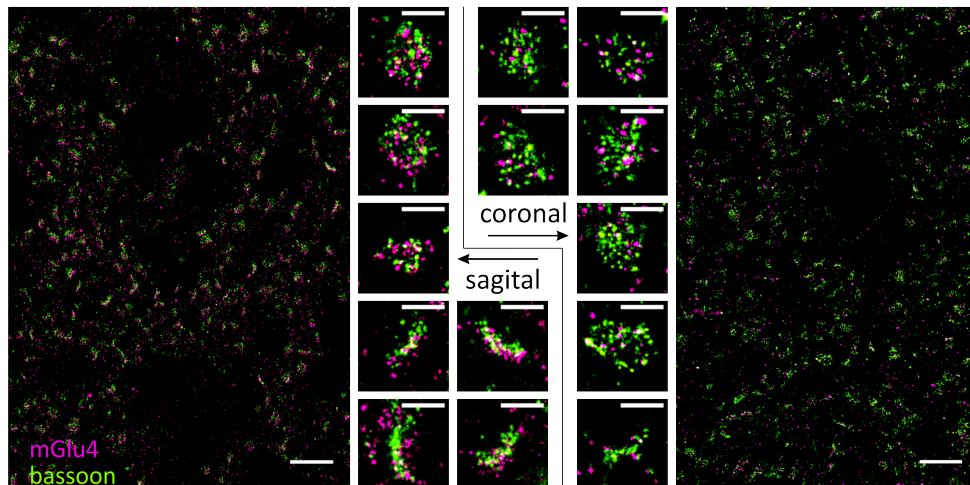The mGlu4 receptor is described to be enriched in the pre-synaptic side of

FIGURE 3.10: Two-colour *d*STORM images of mGlu4 and bassoon in the molecular layer of the cerebellum. Slices in coronal and sagital cut direction were investigated to evaluate the best orientation of imaging the front view on an active zone. The subsets show different front and side views on a synapse.

parallel fibres in the cerebellum but only limited information due to diffraction limited fluorescence imaging is available regarding the localisation of GPCRs at active zones (Kinoshita et al., 1996). To test this hypothesis I performed different cluster analysis on two-colour *d*STORM data of the mGlu4 receptor and Bassoon, a protein that defines well the active zone cytomatrix (Figure 3.10).

To describe the affiliation of mGlu4 with the active zone a major subset of the imaged synapses are captured in a front view looking through the pre- and post-synapse, orthogonal to the synaptic cleft. Cutting the brain parallel to the parallel fibres (coronal cut) should enable a high proportion of front view synapses, while a sagital cutting direction should favour the side

view. In Figure 3.10 super-resolved images of synapses are shown for both cutting directions. The coronal slices show a slightly increased amount of front view synapses. These slices are solely used for the following analysis.

Coordinate Based Correlation Analysis of mGlu4 and Partner
Coordinate based correlation (CBC) analysis enables the test of colocalisation for every localisation. These Spearman correlation values can be visualised through a probability histogram (Compare Figure 3.11 B). In simplified terms the spectrum from -1 to 1 is divided into thirds and assigned to the cases of anti-correlated, uncorrelated (zero) and correlated. For interpretation of this data it is recommended to introduce a control created from simulated data or proper experimental data before the sample of main interest as mGlu4 to bassoon is analysed.

    Positve control sample for CBC   For simulated data, probability histograms for different CBC radii are shown in Malkusch et al., 2012. To create an experimental positive control we labelled bassoon in a cerebellum tissueslice with two different primary antibodies. The antibodies differ in the host, but target the same epitope. A rabbit anti bassoon and a rabbit anti mouse is introduced to the sample with the same concentration and then marked with Alexa Fluor 647 (AF647) goat-anti-rabbit and Alexa Fluor 532 (AF532) goat-anti-mouse, respectively. In Figure 3.11 A) a sub-set of a *d*STORM image is visualised and it is obvious that the density of the two populations differ. This might be caused by a difference in primary antibody affinity, since both antibodies are in concurrence to the same epitope. Another influence factor is the fluorophore choice, since AF647 leads to more localisations than AF532.
For a biological sample this mimics a perfect colocalisation event with the likely phenomena that both population show not the same density and the markers are at least in a distances from 10-20 nm due to the immunostaining. Therefore a correlation value of 1 being equal to perfect localisation is not to expect.
In Figure 3.11 B (left column) a typical probability histogram is shown for a radius r = 120 nm. For the same structure we would expect a correlation value close to one for a majority of localisations. Contrary to our expectations a wide spectrum of Spearman coefficients is estimated and just 21% are valued as correlated. One reason lies in the difference of localisation density, in this case the higher number of localisations in population 1 (AF647). The prominent amount of uncorrelated data is due to the number of single molecule events outside of the synaptic side. To be more accurate, as soon as the algorithm fails to find partner localisations to estimate the Spearman factor, a zero is assigned.
With a change of the direction we test the correlation, in detail population 2 (AF532) regarding to population 1, the correlation value should be generally increased and the number of uncorrelated events should be minimised significantly. To clarify the design of the probability histogram it is divided

in thirds to characterize rather anti-correlated (negative values), uncorrelated (around zero) and correlated (positive) events. In Figure 3.11 C both directions of testing correlation are visualised and the probability for every correlation group is plotted respectively for several radii.

A line connection of these values creates a distinguished correlation pattern for each population with respect to the other.

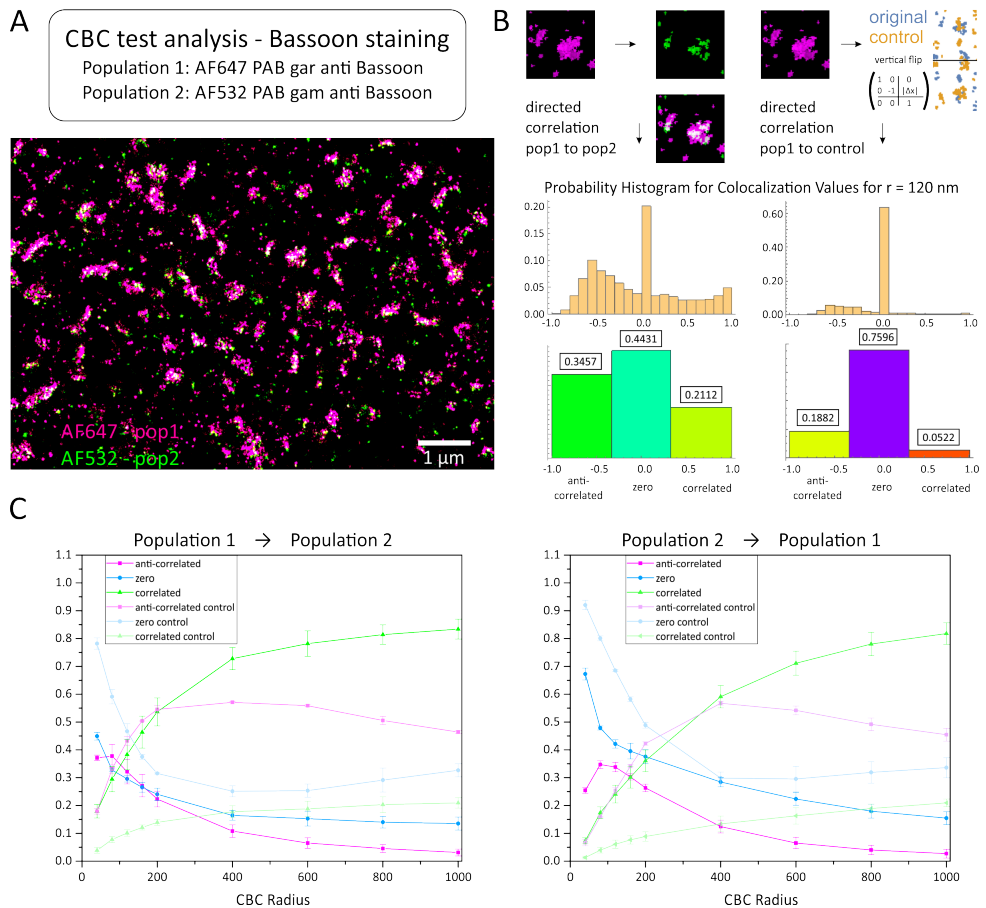If for example the fraction of localisations with a positive correlation (green

FIGURE 3.11: Positive control for CBC anaylsis is performed with an experimental sample. A) As a test sample Bassoon is stained with two marker differing in primary and secondary antibody choice. A subset of a two-colour *d*STORM analysis is analysed. B) CBC analysis of population 1 to population 2 (left) and population 1 to a control image (right) rendered by flipping the population 2 localisation data vertically by a translative matrix. The correlation values for both tests with r = 120 nm are histogrammed below. C) The colocalisation values for both directions and the controls are visualised in two line graphs, showing the probability values for the three correlation groups for different CBC radii. A signature difference in the line garphs of the data set and the control is found to be a necessary sign for a correlative behaviour.

distribution) is compared for both test directions, a greater increase with higher radii of the positive correlation values is detectable for population 1

towards population 2 than for the other way round. Looking at the image in
3.11 A it is obvious that the area of population 2 (green) is covered mainly
with population 1 area (magenta), while magenta has areas without colo-
calisation. This explains the difference in positive correlation values. This
distinguished correlation pattern for one population towards the other still
does not necessarily identify a clear colocalisation. Therefore a control sam-
ple needs to be introduced. I evaluated that the vertical flipped image of the
respective target population serves as an ideal control, since the similarity
of this control to the original data set is intrinsically granted. In the right
column of Figure 3.11 B this evaluation is exemplified. In the graphs in sub-
set C the control values are visualised in light colours and show a significant
different behaviour to the main data. If the control shows the same or ex-
treme similar progress, no clear result can be stated with a CBC analysis.
In all following data analysis a control is evaluated in this way.

mGlu4 and Bassoon   In Figure 3.10 pre-synaptical active zones are
clearly recognisable (green) and the mGlu4 receptor seems to follow this
pattern. While the Ripley's H analysis revealed just a slight evidence for
higher mGlu4 clustering, the CBC analysis enables to test the correlative
factor of every receptor to every bassoon localisation. In Figure 3.12 the cor-
relation pattern for both directions are plotted and we can identify a clear
distinction of the graphs to the control curves. The correlated population
(green) grows with test radii of 800 nm and higher over 50% for both direc-
tions, while the control stays underneath 20%. For the anti-correlated curve,
that describes juxtaposed localisation pattern in the corresponding radius,
peaks occur for radii in between 100 and 200 nm until it evolves contrary to
the correlation curve with increasing radii. This might lead to the assump-
tion that for shorter distances the mGlu4 receptor and bassoon are close to
each other, but not overlapping, though colocalise on the length-scale of the
synapse.

The whiskers on the correlation values describe the standard error of
three evaluated images taken in different areas of the molecular layer of the
sample. Since the control pattern is still differentiable to the sample pat-
tern within the error consideration, a significant positive correlation for the
mGlu4 receptor distribution towards the bassoon population on the length-
scale of synapses can be stated.
Here I want to note already that for future calculations this variance in be-
tween single measurement batches should be analysed further. Also the
distinguish behaviour of the curves of the three correlation group should
be analysed. The investigation of simulated data might establish signature
patterns, that lead to a more precise description of the interplay of two pop-
ulation regarding correlation distances and densities. Also the classification
of the Spearman values in three, equally sized, correlation values should be
tested, if it is valid or if it compromises the correlation description in any
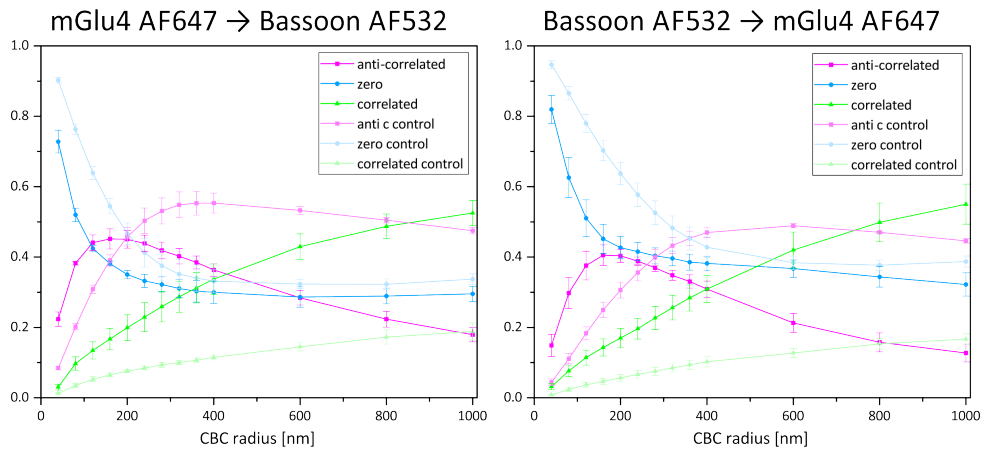way.

FIGURE 3.12: CBC analysis of mGlu4 and bassoon. In the left graph the correlation values are plotted over the CBC radius for mGlu4 localisations towards bassoon localisation. In the right graph the direction is revers. The coefficient were evaluated to a CBC radius up to 1000 nm to test the behaviuor of the curves just beyond the active zone area.

For now I assumed that the averaging of the correlation values of one sample is sufficient to describe a trend of colocalisation or to deny it. Clear conclusions towards a distances, where correlation effects occur, is not achievable in the moment.

mGlu4 and Munc18   Munc 18 is a synaptic protein that is existential for the vesicular fusion process and therefore is crucial for exocytosis. In Ramos et al., 2012 the hypothesis is stated that mGluR4 and Munc18 are colocalised. This was tested by LSM imaging in HEK 293 cells. Munc18 and the mGlu4 receptor were expressed and a partially colcalisation was observed at the plasma membrane.
Therefore we tested if we can recognize a correlative behaviour for short distances. Since the Munc18 staining is very dense and evenly distributed, I introduced a second control sample for the analysis. Additionally to the flipped image I used a non-chromatic-aberration-corrected image (Fig. 3.13 B). In subset C) the correlation pattern is plotted for radii up to 200 nm and there is no significant difference apparent in between the sample and the control pattern. This analysis reveals no significant correlated and therefore colocalised nature of those proteins. Single events might occur at synaptic sites, though no overall trend for a close proximity of mGlu4 and Munc18 is visible. This is consistent with the hypothesis that we expect a confinement of mGlu4 close to the active zone, while the protein Munc18 is not enriched in active zones, but distributed all over the plasma membrane (Südhof, 2012). With super-resolved imaging we can not confirm the hypothesis of Ramos et al., 2012, although the CBC analysis might underestimate correlative subsets that appear in the overall statistic.
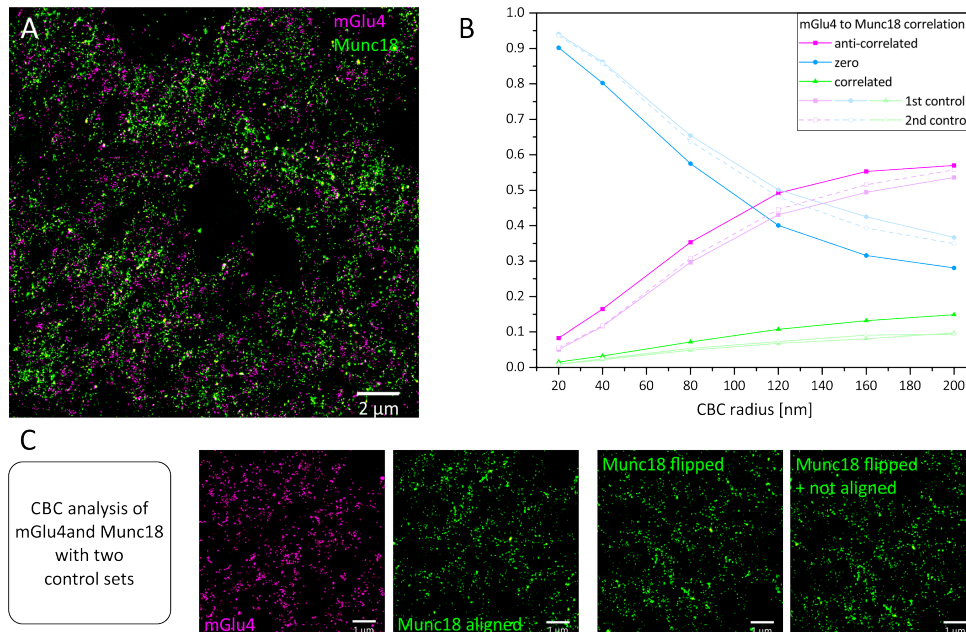
FIGURE 3.13: Coordinate based correlation analysis of mGlu4 and Munc18:
A) Dual-colour *d*STORM image of mGlu4 (magenta) and Munc18 (green).
B) CBC analysis is performed with subsets of the data. The correlation
probability is evaluated for mGlu4 towards the aligned Munc18 data and
two control data sets. The probability histogram values for various CBC
radii visualised are plotted in a diagram. C) The control data is either ver-
tically flipped or vertically flipped and not aligned.

mGlu4 and Ca$_v$2.1　　In the cerebellum of rodents mGlu4 receptors sup-
press on activation excitatory synaptic transmission. With physiological
measurements it was shown for example in Abitbol et al., 2012, that phar-
macological activation of mGlu4 acutely depresses synaptic transmission at
parallel-fibre and Purkinje cell synapses. This involves the inhibition of pre-
synaptic voltage-gated Ca^{2+} channels and therefore ultimately the control
of glutamate release. Unravelling distributional connections help to con-
firm findings of functional measurements that draw a picture of a molecular
correlation of voltage-gated calcium-channels and metabotropic glutamate
receptors.
With the CBC approach I addressed measurements of mGlu4 and Ca$_v$2.1 in
the molecular layer of a mouse cerebellum. In Figure 3.14 C and D the rel-
ative frequencies of the three correlation groups are plotted over the CBC
radii in a range of 40 to 400 nm. Comparing the data and the control curve,
both show a similar behaviour, just the correlated population exceeds the
control slightly. A resemblance to the prior analysed mGlu4 and Munc18
data sets is noticeable. Therefore the CBC analysis hints to no significant
correlation of mGlu4 and Ca$_v$2.1.
Nevertheless, in the *d*STORM images in Figure 3.14 A and B a subset of

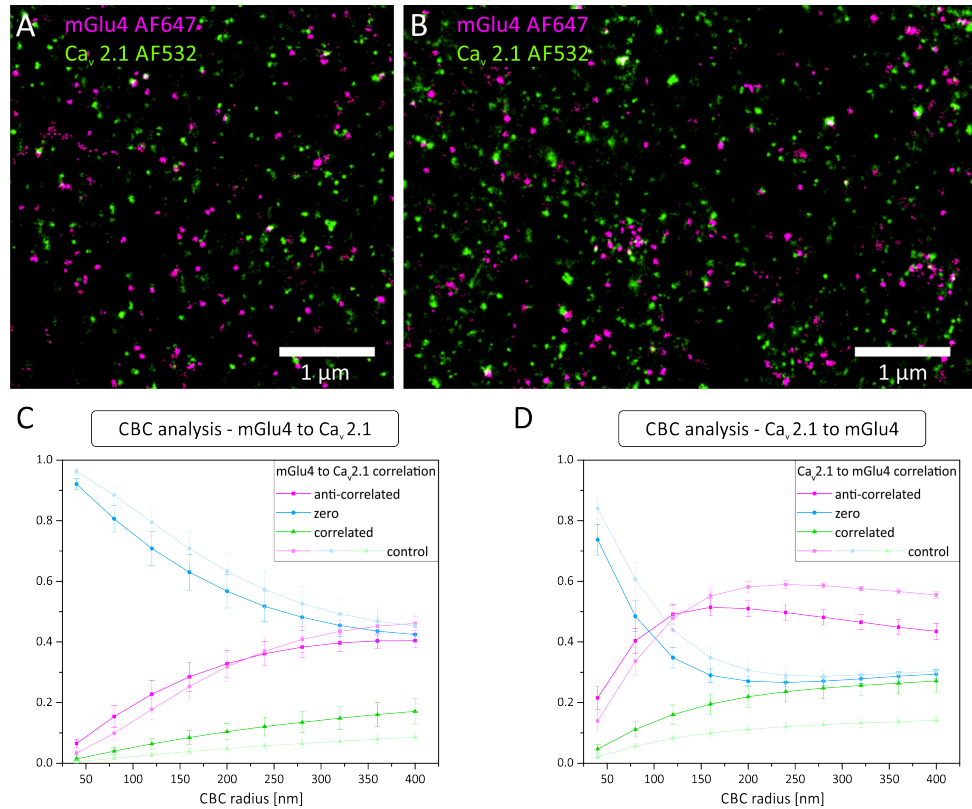mGlu4 and Ca$_v$2.1 signal occurs in close proximity.

FIGURE 3.14: Coordinate based correlation analysis of mGlu4 receptor and voltage-gated calcium channels. A) and B) are two-colour *d*STORM images of different cerebellar brain slices. The CBC analysis was performed for different measurements and the variance in between the measurements is identified with the error bars (SE). The control was the flipped data set of respectively population 2. In C) the correlation values are plotted for the direction mGlu4 receptor to calcium channel and in D) vice versa.

Another possibility to unravel a connection of those proteins is the nearest neighbour analysis of cluster centroids. Centroid nearest neighbour analysis of mGlu4 and bassoon areas is not valid for the structural size and form difference of both population. However, the appearance of mGlu4 and Ca$_v$2.1 is very similar. The cluster are circular and have approximately the same size. A nearest neighbour analysis might reveal a population of mGlu4 and Ca$_v$2.1 proteins in close proximity.
To identify the receptor and protein cluster the DBScan analysis was applied and the parameter of 4 minPts for a radius of 16 nm were found valid for both distributions. A nearest neighbour analysis was then performed on the defined cluster centroids of both populations (Figure 3.15 A). As a control the centroids of the first population are randomised and the distances with population 2 are analysed. In Figure 3.15 B and C the distances are histogrammed for both analysis directions. In both graphs a deviation from

to the control towards smaller distances is visible. This difference hints to a population subset of smaller distances in between mGlu4 and $Ca_v2.1$ that is not observed in a random distribution. Therefore the dataset shows a combination of at least two populations with a certain mean distance. Under the assumption that for larger distances the sample distribution follows the random distribution, we can estimate the size of the randomised population by normalising the random control. In subset B and C the case of a 100% random population is shown in dark magenta. To estimate a correction factor of the random curve to compare it to the real population of the random share, the random curve is compared to the data set distribution at a range where the data assumingly also follows a random distribution. For the mGlu4 randomisation I estimated a distance of 200 nm and higher and for $Ca_v2.1$ 400 nm and higher for the correction factor evaluation. In Figure 3.15 E and F the normalised distribution is visualised in dark magenta. The compensated distribution is the difference in between the normalised random population and the source data. This distribution is especially for the test direction mGlu4 to $Ca_v2.1$ shifted towards smaller distances as expected.

The NN distance analysis should show for both directions the same distribution as long as both populations occur in the same frequency and density pattern. Although specifically the calcium channel signal is widely distributed over the whole sample and therefore shows more localisations outside the pre-synaptic site resulting in a higher NN distance. The receptor mGlu4 finds finds on the other hand with a high probability a corresponding $Ca_v2.1$ signal in closer proximity to the active zone area.

To ensure that this imbalance of patterning does not compromise the analysis an additional control was implemented that uses the vertical flipped data set as a control. In our tests the flipped control follows perfectly the random control.

The peak at small distances that is visible in the mGlu4 to $Ca_v2.1$ analysis is therefore properly hidden in the distribution of a population of longer distances describing the distances of $Ca_v2.1$ to the active zone. The table in D lists the distance mean values for the two different directions. The mean and the median value of the whole distance analysis spectrum is no indicator for the distance of close proximity localisations, but simply indicates a difference from the random non correlative case. The mean value of the compensated curve is with 66 nm describing a close proximity of mGlu4 to $Ca_v2.1$, though a striking peak with a maximum at 50 nm is visible in the main distribution and hints to the direct connection of mGlu4 receptors and voltage-gated calcium channel.

Summarizing I claim that a subset of 56% of the mGlu4 cluster population is in close proximity to $Ca_v2.1$ cluster with an estimated distance of approximately 66 nm. This is an interesting affirmation of the functional relation of those two targets. I suggest further simulation controls of the NN distance distribution that help to interpret the distance distribution better and that
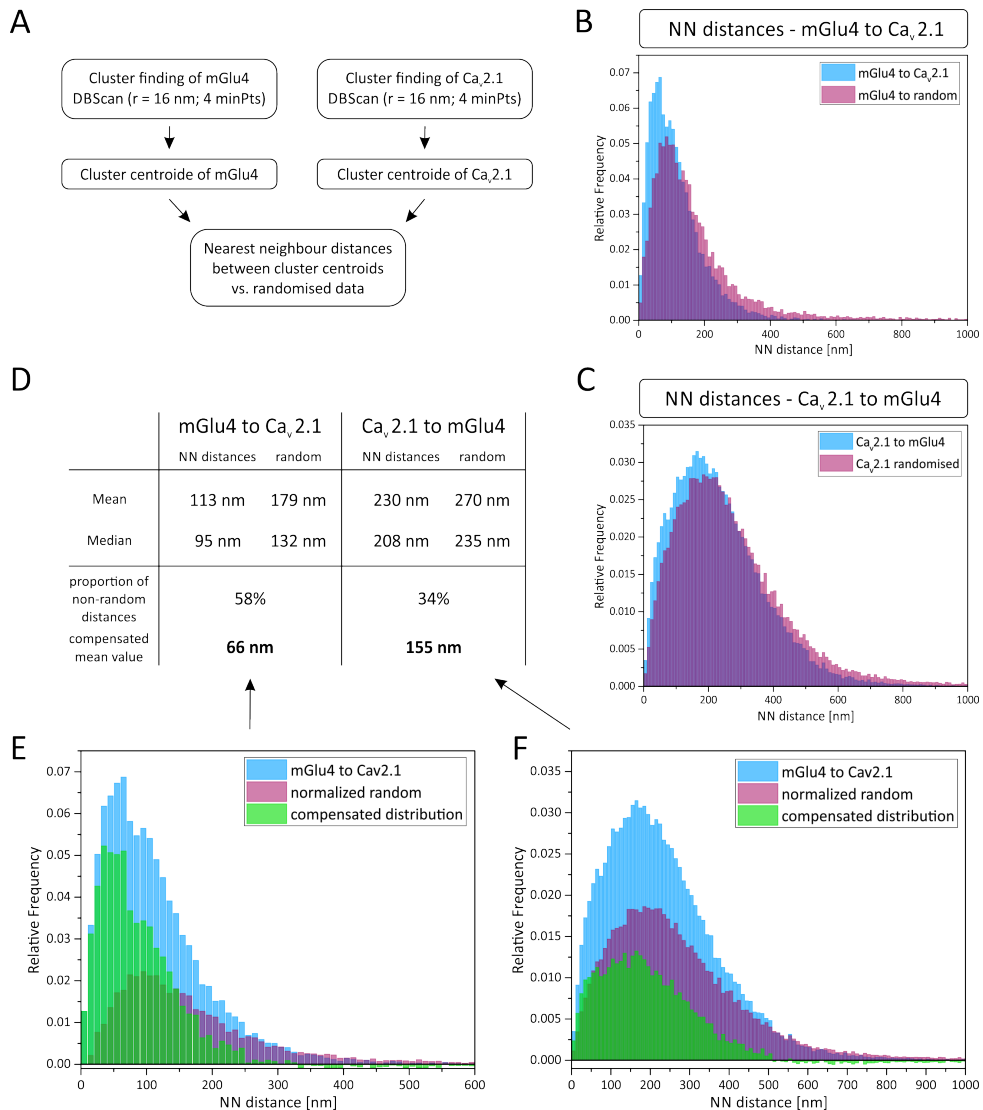
FIGURE 3.15: Nearest neighbour analysis for mGlu4 and Ca$_v$2.1 cluster centroids. A) The cluster are identified by a suitable parameter and a nearest neighbour (NN) analysis is performed on the cluster centroids. B) Histogram of the NN values for the mGlu4 centroids towards the Ca$_v$2.1 distribution. As a control the mGlu4 data was randomised, therefore we receive a control distribution with the same number of distances. C) The same analysis is performed for the opposite direction. D) Mean value and median of the NN values for both direction is comparison to the a mean value estimated on a corrected NN distance distribution. A correction is performed by normalising the random distribution as described in the text and estimating a compensated distribution by subtracting the normalised random value from the source data. In E) and F) the compensated distributions are plotted for both test directions.

additionally helps to estimated the fraction of mGlu4 receptors that are connected directly the calcium channel and is represented by the peak at 50 nm

NN distance.

Extendent Distribution Analysis of mGlu4 and the Active Zone   Previously, the correlation of the mGlu4 receptor and the active zone, identified by bassoon, was shown with a CBC analysis. All detected localisation were taken into account for this analysis. Though our sample has a three dimensional extend and the orientation of the synapses is to a certain level arbitrary. To obtain an advanced understanding over the density distribution of the receptor of interest, just the localisations around synapses that are parallel orientated to the imaging plane should be taken into account. In this case eventual patterns of the receptor distribution can be elucidated.

To accomplish this task, it is necessary to establish a strategy to distinguish front view from side view synapses and then evaluate the density and distribution of mGlu4 inside and out side of the synapses of choice.

Identification of the Active Zone   Similar to the approach I described previously for the identification of parameter for cluster findings, I performed a serial scan with variable DBScan radii and minimum number of points. A solid parameter set was hard to establish due to the fact that natural cluster distribution are a continuum of sizes and show no distinguished parameter criterion. All parameter are dependent on label density and quality of signal to noise ratio and the ultimate decision was made by visual control, which is a soft parameter. All data was evaluated with the same parameter set of a scan radius of 80 nm and the number of minimum points of 20 to grant comparability. Afterwards we perform a second cluster finding algorithm that offers a better estimation to the shape of the synapse. The alpha shape algorithm requires higher computational cost. Accordingly all cluster except those with an area (convex hull) of 40000-250000 nm^2 are excluded to reduce the amount of data. The alpha shape parameter is 50. This step was introduced to get a better estimation of the size of the active zone. The main workflow is described in Figure 3.16. To identify the orientation the two parameters *inertia moment excentricity* (IME) and *bounding box elongation* (BBE) can be calculated. The IME is proportional to the ratio of the long and short axis along the main inertia moment of the localisation distribution. The BBE is identified by the ratio of the edge length of a rectangular hull of the cluster distribution. With those two parameter we can separate the two extreme orientations of a very round distribution, interpreted as a frontal view on a synapse and an elongated distribution, mimicking the side view. A parameter range couple of $IME = (min, 0.8)$ and $BBE = (min, 0.4)$ identify the front view as shown in Figure 3.16 E (left). A zero value for both parameter would equal a perfect sphere. It is noticeable that inertia moment excentricity is susceptible to rogue localisations and the spectrum that is valid for a circular shape is widened. The parameter couple of $IME = (0.8, max)$ and $BBE = (0.5, max)$ identify the side view shown on the right side of the subset E in Figure 3.16.

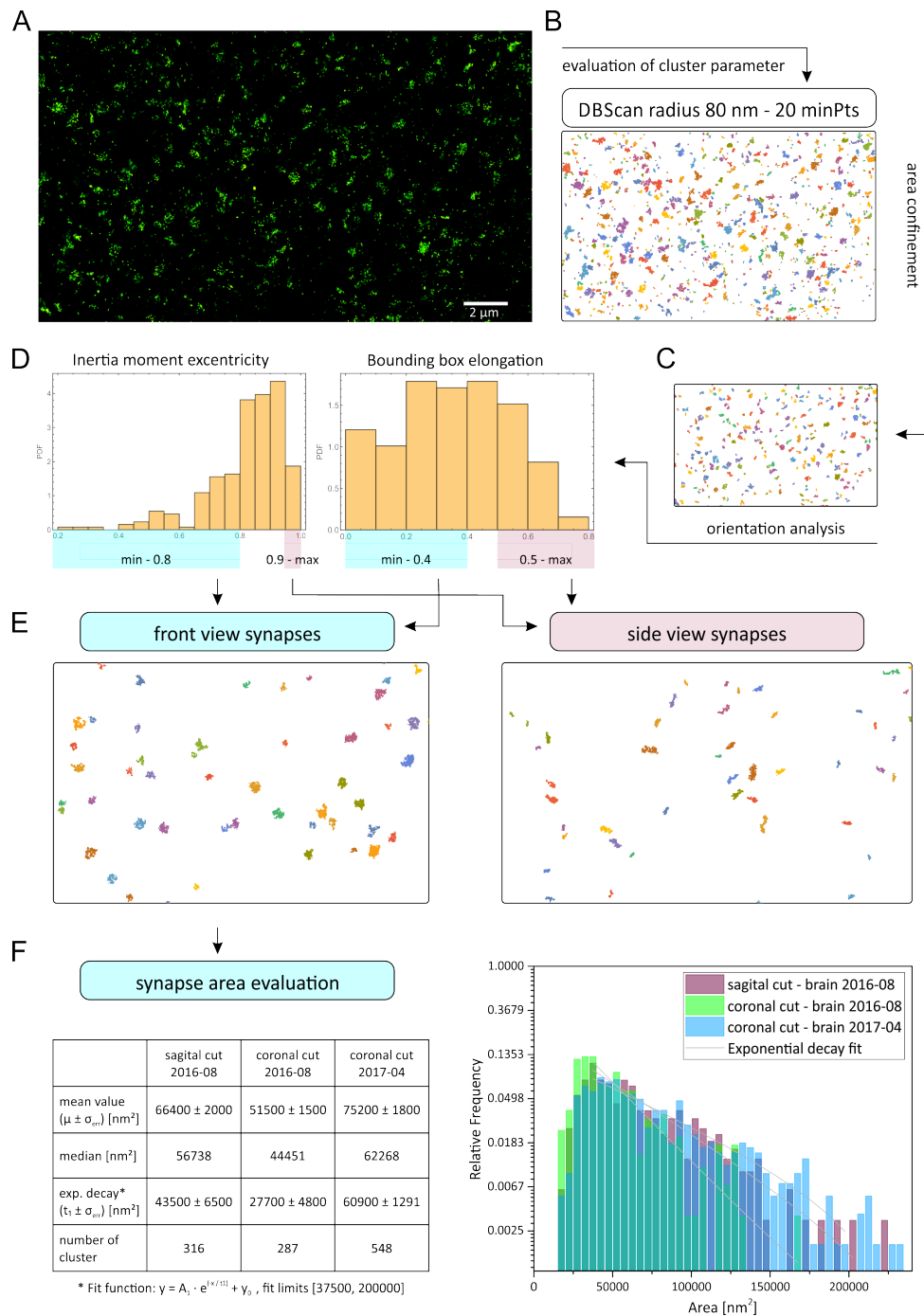This analysis enabled also an area estimation of the active zone as outlined

FIGURE 3.16: Identification of the orientation of active zones: A) *d*STORM image of bassoon stained with AF532 in coronal-direction sliced brain tissue. B) The parameter for the DBScan algorithm need to be identified and the evaluated cluster are filtered area specific (C). D) The circularity and therefore the orientation of a cluster can be defined via two factors, the bounding box elongation and the excentricity of the inertia moment. Filtering for both characteristic serves a solid criterion for the circularity of an active zone staining. In E) both extreme cases, a frontal view (left) and a side view (right), are demonstrated. F) With the front view synapses the mean area size is estimated for different sample groups and the distribution of the area sizes is histogrammed in the right diagram.

by bassoon. For these measurements we used three different samples. Two slice were cut in coronal direction, where we expected more front view synapses, and one sample cut in sagital direction. In Figure 3.16 F the evaluated area sizes are visualised in a histogram. We can identify a wide spectrum of sizes and no prominent population. Therefore it is impossible to identify an overall synapse size. In the table in Figure 3.16 F the mean value with the standard error and the median of the area distribution of every sample group is listed. Additionally the histogram of the area values was fitted with an exponential decay in the limits of 37,500-200,000 nm^2. The decay constant estimates as well a mean area. It is noticeable that the values differ by method, but also depend on the sample. For future work it might be interesting to evaluate mouse specific differences. Taking all cluster into account we can claim a mean value of 64000 ± 6900 nm^2 for the synaptic active zone extend identified by bassoon staining.

Distribution of mGlu4 Localisations Related to Active Zone Cluster
With the automatic detection of front view synapses and side view synapse, we can now identify the distance of mGlu4 localisations to the borders of a synapse. With this calculation we can identify receptor localisation within and outside the synaptic active zone and additionally identify the receptor density inside the active zone compared to outside. In Figure 3.17 the calculation steps, that are necessary for this process, are visualised. All front view synapses are identified as described in the previous section. To ensure that we count all receptor localisations that lie exactly on the border of the bassoon area, 20 nm are added to the border limit of bassoon. In the draft of one example synapse in Figure 3.17 (upper right) this is visualised with the light-blue area added to the grey one. This is now defined as the synapse border (black line). To determine the outer area, we define a maximum orthogonal distance from every border-point, in our case stated as 2000 nm, and describe this as the outer area. To avoid over-counting of localisation in this area, it is made sure that overlapping areas are just counted once.
The inner density is described by the number of localisations per synapse area (of all synapses), accordingly the outer density by the number of localisations per the entire outer area. The estimated densities are listed in the following:

sample	inner density [loc/nm^2]	outer density [loc/nm^2]	ratio
sagital cut	$15.80 \cdot 10^{-4} \pm 0.56 \cdot 10^{-4}$	$2.63 \cdot 10^{-4} \pm 0.013 \cdot 10^{-4}$	6.01 ± 0.04
coronal cut I	$7.49 \cdot 10^{-4} \pm 0.48 \cdot 10^{-4}$	$1.25 \cdot 10^{-4} \pm 0.28 \cdot 10^{-4}$	5.99 ± 0.23
coronal cut II	$4.64 \cdot 10^{-4} \pm 0.37 \cdot 10^{-4}$	$0.99 \cdot 10^{-4} \pm 0.094 \cdot 10^{-4}$	4.69 ± 0.12

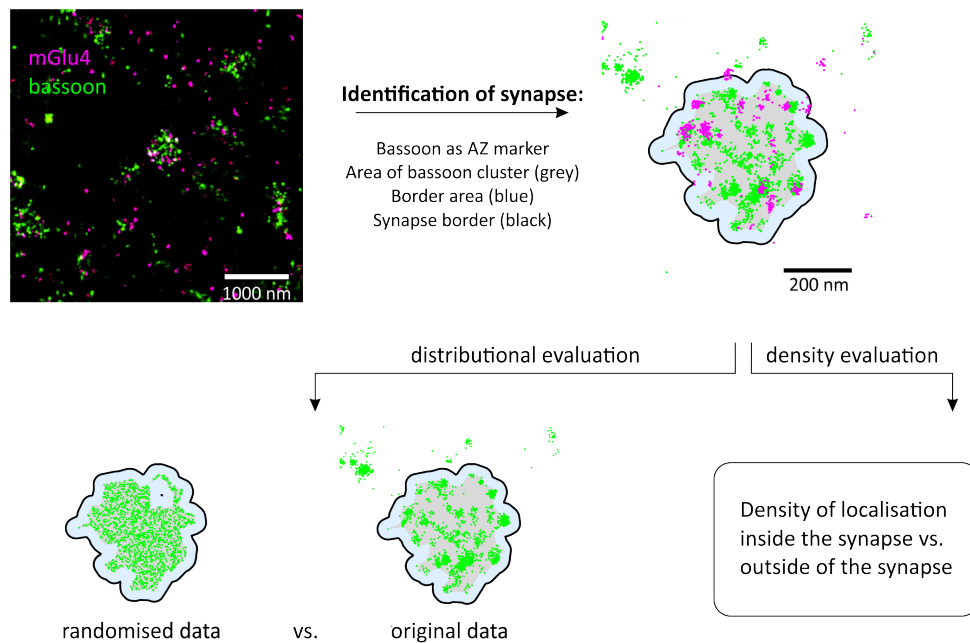TABLE 3.1: Synaptic density of the mGlu4 receptor in the molecular layer of the cerebellum.

FIGURE 3.17: Density analysis of mGlu4 in synapses: The data is scanned for front view active zones idenfied by a bassoon staining with qualities as described in the previous figure. The rim localisations of the bassoon cluster describe the synapse border. We increase the border 20 nm to the outside to cope with mGlu4 localisations on the rim, that should be counted to the inner area. For the density estimation the number of localisation is estimated per inner respectively outer area. To investigate the distances of localisation from the synapse border every the distance of every localisation of a population to the closest border point following a line orthogonal to the border is estimated. Values inside the synapse are negative. To interpret the distance distribution a control is necessary and is implemented by arranging the localisations inside or outside the synapse randomly and histogram this distribution.

For all tested samples we can estimated that the density of the mGlu4 receptor is 4-6 times higher in the synaptic active zone than outside the synapse. mGlu4 is significant enriched at the pre-synapse. If the prior evaluated synaptic area size and the estimation that every receptor cluster contains approximately 20 localisations is taken into account, it can be assumed that every synaptic site contains two to five mGlu4 receptors.

To identify if a peculiar patterning of the receptor occurs in all the synapses, the distance of every localisation from the synapse border was evaluated. The border was defined as described before. The distance is defined along an orthogonal line from the localisation to the closest border point and has negative values inside and positive ones outside. To be able to decide if the distribution is special the distance distribution needs to be compared to the distribution of a randomised pattern with the same amount of localisation events in the same area. This can be simulated for the inner and outer area of an active zone.

In Figure 3.18 this evaluation, performed with the Mathematica script locan, is visualised. In subset B the distribution for bassoon and mGlu4 is plotted for one sample. The values were evaluated of five two-colour super-resolution measurements and the absolute number of localisations is stated. It is noticeable that the distributions follow well the random distribution. The only variation occurs around the defined border. For the bassoon distribution a sharp limit around -20 nm is to be expected, since we artificially relocated the border limit 20 nm to the outside to ensure that we count the mGlu4 localisations directly on the border completely as inside localisations. We can observe that mGlu4 does not sit much further outside than the bassoon signals. The random distributed control value are allocated to the chosen border and therefore we estimate more localisations there. It is striking that the distribution forms of each of the sample differs.

The form depends strongly on the shape of the synapses and therefore it is not possible to interpret the absolute form of the distribution. A difference to the random distribution control is therefore an important criterion. Over all there is no extreme variation visible compared to a random distribution of localisations inside and outside the cluster. It is important to note that this mirrors the ensemble of all synapses. We can state that for example on average mGlu4 is not just distributed on the outer rim of the active zone or just in the centre, but everywhere along the active zone. This equal distribution pattern is not contradictory to the possibility that certain synapses form special protein distributions to support functional processes. For this a detailed patterning investigation would be of interest.

Summary of mGlu4 Receptor Distribution

The mGlu4 receptor exhibits a positive correlation coefficient on length scales of the size of the synaptic active zone. Additionally we could show that the density of mGlu4 is increased 4.5-6 fold inside the synapse compared to the outer synapse area. In the ensemble of all measured synapses (N = 1151 frontal view active zones) we could not identify a certain distributional pattern that differs significantly from a random receptor arrangement. This result does not exclude the possibility of function depended clustering or a development of nanodomains in the active zone. Though we could not find a density gradient towards the outer rim or the centre of the synapse.
Furthermore we could not determine an affiliation with Munc18 proteins. For the correlation analysis of the mGlu4 receptor with voltage-gated calcium channels the correlation varies from a random distribution and we can find a population of close to 50% being in a distance around 60 nm. With the nearest neighbour distances calculated of the cluster centroids we can confirm this, albeit a comparision with simulated data would be advisable for a proper distance determination of the correlated subset of mGlu4 and $Ca_v2.1$. Also an analysis with the nearest neighbour distance approach would be interesting for the Munc18 distribution and will be analysed as a next step.
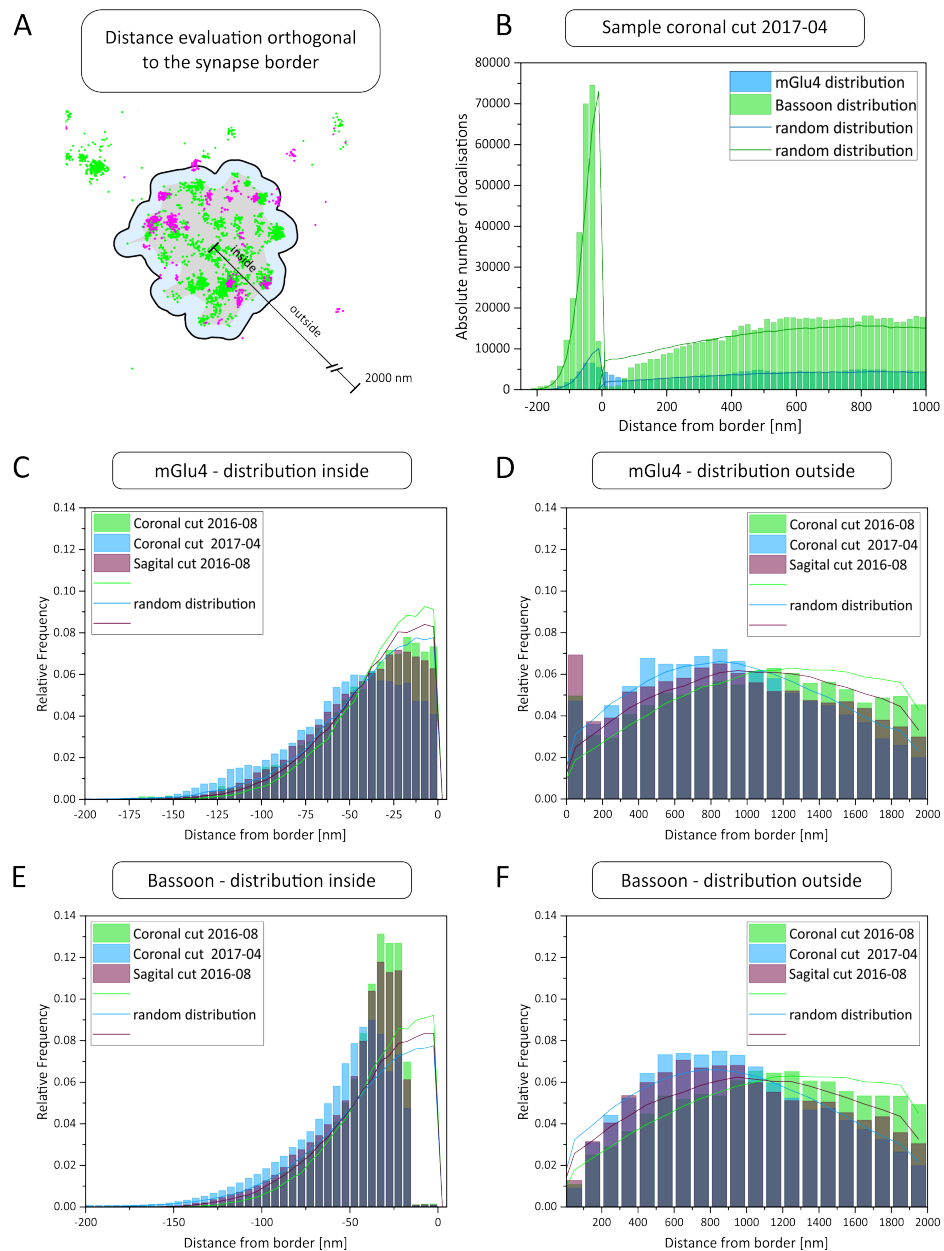
FIGURE 3.18: Evaluation of mGlu4 and Bassoon distribution around the synapse. A) A sketch of a front view synapse. The distances to the rim of every localisation are estimated along an orthogonal line towards the nearest border point. Distances inside the synapse are valued negative and outside positive. The outer area is defined as maximal 2000 nm away from a synapse border. B) Histogram of the absolute number of localisations per distance for mGlu4 and bassoon. The line plot visualizes the corresponding randomised distribution. A higher density of both proteins in the synapse is clearly visible, as also the number of bassoon localisations exceeds the number of mGlu4 approximately seven times. The graphs in C)-F) show the relative frequency of localisations for three different samples. It is noticeable that the distribution differs slightly, but for every population it follows approximately the random distribution.

3.2   Correlative *d*STORM-SIM Microscopy

Super-resolution imaging techniques are able to unravel important information about the distribution of proteins in different areas of the brain and their affiliation to another protein as shown in the previous chapters. Nevertheless, all quantitative measurements on the protein of main interest were performed with the most reliably dye, the red emitting carbocyanine Alexa Fluor 647. Even for Alexa Flour 532, which is used as reliable dye in the green spectrum, the photophysical properties that lead to an ideal on-off-ratio and a high resolution are not as reproducible as with Alexa Fluor 647. Three colour *d*STORM on a relevant biological sample has not been carried out at all.

In order to visualize the distribution of syntaptic proteins in brain slices in the context of more than one synaptic structure we developed a correlative super-resolution imaging approach. In the following chapters I introduce a *work flow* to combine one-colour 2D and 3D *d*STORM with 3D multicolour structured illumination microscopy (SIM) on two independent setups. In addition to the nanoscopic resolution of *d*STORM, SIM enables imaging of multiple targets with a twofold improved resolution compared to conventional fluorescence microscopy. Together with the bachelor student Sebastian Reinhardt I developed a software named coSI*d*STORM (correlated Structural Illumination and *direct* Stochastic Optical Reconstruction Micrsocopy) to visualize and align correlated *d*STORM-SIM data.

As a proof of principle correlated imaging is applied to a neural example structure. The pre-synaptic protein bassoon is visualised in a super-resolved 3D image and set in to context with a staining of the dendritic system of Purkinje cells in the molecular layer of a mouse cerebellum in combination with marked parallel fibres. With this approach the synaptic sites, that are formed in between those specific neural types, can be identified.

3.2.1   Acquisition and Sample Demands

The correlation of microscopy methods brings about the challenge that the sample preparation requirements differ with each method. Combining SIM and *d*STORM the demands are basically the same. Nonetheless some minor demands need to be served to establish optimal imaging conditions. One important aspect is the fluorophore type used for the particular technique. *d*STORM requires photoswitchable dyes, while the quality of the SIM images relies on photostable dyes. Therefore, it is crucial to embed the sample in a chemical environment that is advantageous for both methods. I will discuss possibilities to establish a compatible environment. Additionally different approaches to align the both data sets will be addressed. This is a non-trivial task due to the different sizes of the field of view and possible optical distortions by using varying detection pathways in the separate setups. A typical acquisition work flow is provided.

Embedding the Sample

SIM acquisition can be performed with a relative low illumination energy (focal plane intensity: 100 W/cm^2). Although it is a trade-off in between signal to noise and illumination density. There are certain reagents suggested in the literature to improve the photo-stability of several fluorophores. Pro-Long Gold (ThermoFischer) is a typical commercial choice for an antifading reagent since its refractive index matches that of the oil-objective. A premiss for our approach is that the embedding medium is either suitable for SMLM measurements or easy to remove. In the following I want to discussion three possible buffer conditions, that I tested to reduce photo-destruction and bleaching with-in the SIM measurement, and at the same time to maintain a reliable sample for the *d*STORM imaging. I tested the following buffer conditions:

Buffer	Specification	Method	Literature
VECTASHIELD Mounting Medium	no counterstain, pure medium on sample	SIM and *d*STORM	VectorLabs; Mönkemöller et al., 2015
Trolox Buffer	Oxygen radical absorbance capacity; 2mM Trolox in 50% PBS(1x) and 50% TRIS (1M) buffer	SIM	Rasnik et al., 2009
MEA switching buffer	100 mM MEA in PBS pH 7.4	SIM and *d*STORM	Linde et al., 2011

TABLE 3.2: Tested buffer conditions for correlated SIM-*d*STORM measurements to reduce photobleaching with SIM measurements.

The claim that fortuitously, the mounting medium "Vectashield" (Vector Labs) which is commonly used in 3D-SIM applications, enables excellent blinking behaviour of Alexa Fluor 647 (Mönkemöller et al., 2015) can only be confirmed with some reservations. The blinking properties of Alexa Fluor 647 are strongly influenced and an increased excitation intensity is required. In tests on our home build setup an increase of the excitation density of 20% was mandatory to achieve suitable switching rates. With Vectashield also a higher fluorescent background occured, when irradiating the sample with a wavelength of 640 nm. Therefore the signal to noise is compromised. Using the buffer just for SIM measurements was not applicable, since the high viscosity of the product does not support a complete removal. A Trolox buffer as described in Table 3.2 showed good properties for SIM measurements as it was published in Rasnik, McKinney, and Ha, 2006, although due to reduced off-switching rates *d*STORM images could not be acquired successfully. However, it is easy to remove and a standard switching buffer can be applied for *d*STORM measurements after initial SIM experiments.
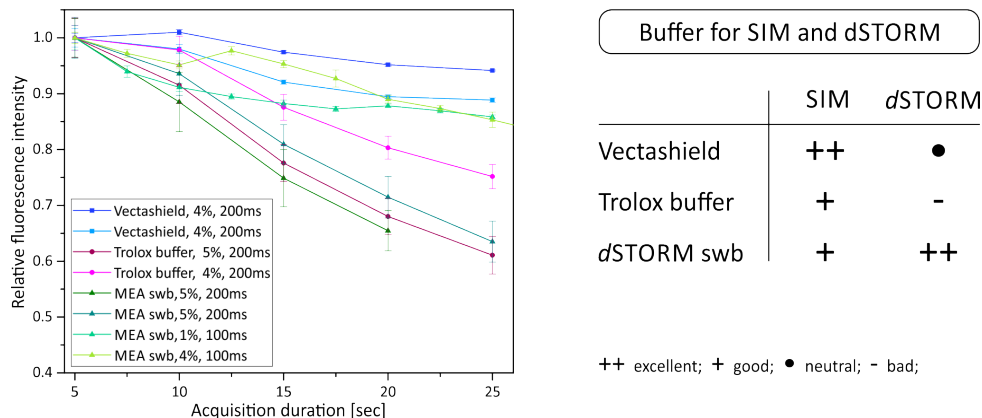
FIGURE 3.19: Comparision of different experimental settings used for SIM measurements. The mean fluorescence intensity of the sample is plotted over the overall integration time. Three elements were varied: the embedding medium, the integration time of the SIM image acquisition per rotation and the excitation intensity. The intensity values are relative values stated in percentage by the Zen control software. The error bars are defined through the standard deviation of the mean fluorescense intensity values of all rotations per layer.

The standard switching buffer for *d*STORM as described in Linde et al., 2011 was also investigated for SIM measurements. In particular 100 mM mercaptoethylamin with a pH of 7.4 is used without an additional oxygen scavenger system. For low excitations it stabilises the photostability of Alexa Fluor 647 and therefore enables a non-blinking fluorescent state with reduced bleaching compared to a PBS environment. To achieve the same bleaching prevention as with Vectashield the excitation intensity of the structural illumination needed to be decreased by at least 50% (compare Figure 3.19). An ideal combination of integration time and excitation needs to be evaluate specificly for each sample. But the achieved images of Alexa Fluor 647 and were always perfectly suitable with low excitation, since the SIM Alexa Fluor 647 signal serves mainly as orientation signal to compare with the corresponding SMLM signal of AF647. The photostability of other used dyes, in the following example Alexa Fluor 568 and GFP, were supported as well by the MEA switching buffer condition in the SIM experiments.

Orientation in the Sample

Orientation in a complex sample is a challenge, which exacerbates, when the sample needs to be moved to a different microscope stage. Despite the fact that it is possible to find the same region on a *d*STORM Setup, as was previously visited on a SIM setup, fiducial marker or landmarks that are visible in both images are mandatory for registration.
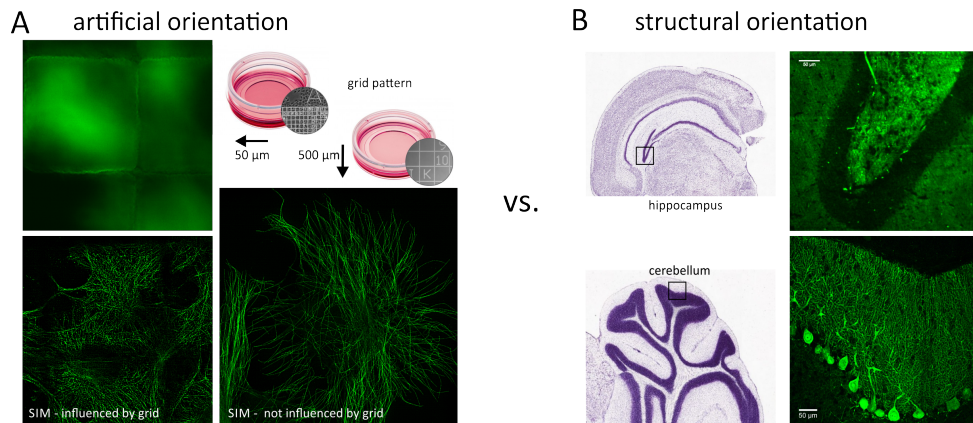
FIGURE 3.20: A) Chambers with orientation points e.g. grid patterns facilitate the orientation and the revisiting of individual areas. Though regular patterns might influence the performance of some methods. U2OS cells stained with Alexa Fluor 532 on beta-tubulin imaged with SIM. The cells plated on the 50 μm grid are imaged with artefacts, while structures that are in a sufficient distance from the grid are not influenced. Grid chambers by Ibidi (http://ibidi.com). B) Orientation by natural structures can be useful, but depending on the region of interest not always sufficient due to the limited field of view for dSTORM. Structural sketches by http://atlas.brain-map.org. Hilus in hippocampus overview: widefield fluorescence image of bassoon staining with Alexa Fluor 532. Cerrebelum Calbindin staining with Alexa Fluor 568 with SIM.

Some correlated approaches rely on artificial fiducial markers introduced into the sample. Hampton et al., 2017 used for example 10-nm gold as fiducials for alignment of tilt series images and 100–200 nm TetraSpeck or Fluo-Spheres as registration fiducial. Those Tetraspecks (ThermoFischer) or similar fluorescent spheres are filled with various, photostable fluorophores. Therefore these spheres are bright and stable fluorescent under various excitation wavelengths. As soon compact samples are used, like in our case brain tissue, those beads fail to enter the probe and remain on the surface. Therefore the alignment features are not necessarily in a region of interest. Another possibility would be to introduce specific marker that bind in the target area with a low labelling density. For example microtubuli stained with gold-beads or a fluorophore in an unused emission spectrum. This method demands an extra wavelength or if used parallel to a comparable fluorophore interferes with the sample information. As the most advantageous method we choose to align via the sample structure itself. This demands a careful setting for the SIM acquisition to minimize any photo-destruction of the target fluorophore. In section 3.2.2 the alignment process is explained further.

The previous mentioned markers are all designed to achieve a registration of the two image datasets for SIM and dSTORM. To facilitate the orientation in the sample itself chambers with an implemented grid pattern (Ibidi) where tested. Here it was noticeable that the regular pattern interferes with

the structural illumination approach and therefore the reconstructed images are error-prone as visualised in Figure 3.20 A. This influence on the PSF pattern also deteriorate the Gaussian fitting mandatory for *d*STORM. Note that for using those chambers a grid structure wider than the field of view is recommended. For tissue samples of certain brain areas the natural structure itself may serve as orientation. This was successfully tested on hippocampal and cerebellar structures. Though, a calibrated sample holder compatible with both microscope stages or a combined setup improves the orientation tremendously for introducing global coordinates.

Work-flow of SIM and *d*STORM Measurement

The sample preparation for both methods is in principle the same. Standard protocols for fluorescence labelling are applicable and mainly dependent on the target structure. A typical work-flow is drafted in Figure 3.21. Special requirements lie in the choice of fluorophores. *d*STORM measurements rely on reversible photoswitchable fluorophores (compare Chapter 1). It is recommendable to use Alexa Fluor 647 as it was shown that quantitative measurements with *d*STORM are most reliably performed using this red emitting carbocyanine dye or its homolog Cy5 in Ehmann et al., 2014. SIM images improve with more photostable dyes, but there are many options of dyes that can be used for various excitation wavelengths . SIM and *d*STORM measurements need to be processed sequentially. The illumination intensities applied by *d*STORM are approximately 5 kW/cm^2 and lead to photo-destruction of a subset of fluorophores. Since the alignment is applied via the signal of Alexa Fluor 647 of the two imaging modes to overlay the data, SIM imaging is accomplished first in 100 mM MEA switching buffer to minimise photobleaching.

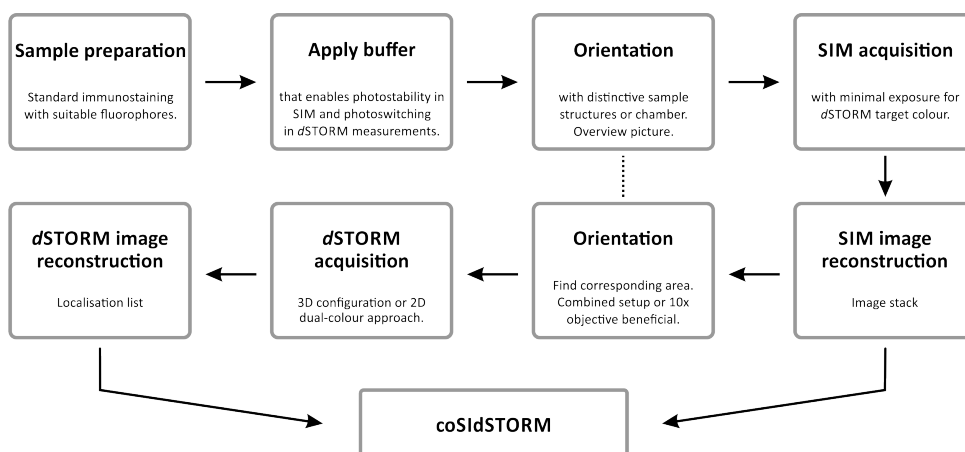| **Sample preparation** Standard immunostaining with suitable fluorophores.	**Apply buffer** that enables photostability in SIM and photoswitching in *d*STORM measurements.	**Orientation** with distinctive sample structures or chamber. Overview picture.	**SIM acquisition** with minimal exposure for *d*STORM target colour.
_d_STORM image reconstruction Localisation list	**_d_STORM acquisition** 3D configuration or 2D dual-colour approach.	**Orientation** Find corresponding area. Combined setup or 10x objective beneficial.	**SIM image reconstruction** Image stack

coSIdSTORM

FIGURE 3.21: Work-flow graphic for correlated SIM-*d*STORM measurements.

After applying the switching buffer the sample is introduced to the SIM setup. We used the Elyra S.1 (Zeiss, configuration Chapter 2) and searched for distinct structures with a 10x objective. After switching to the 63x oil objective, suitable acquisition settings for the different marker were chosen. The illumination and acquisition settings should be chosen as passive as possible for the dye that serves *d*STORM as target. Therefore the irradiation time and excitation intensity were minimized. The image reconstruction was performed with the Elyra S.1 implemented Zen software (black edition). SIM imaging should be performed for all areas of interest before shifting the sample to a widefield setup. Here I like to note again that a single combined setup would facilitate the orientation and direct sequential acquisition of one area of interest.

In principle the *d*STORM measurements then were performed as described in Chapter 2. It is advisable to renew the switching buffer every two hours. Typically, 100,000 frames for 3D-imaging were recorded at frame rates of 60 Hz. The blinking condition needs to be modulated to a lower on-off rate to ensure the temporal confinement of the fluorescence signal from different axial positions. The applied irradiation density lies at 4–6 kW/cm^2. Confined illumination with TIRF and HILO is not recommended, but epi-illumination to ensure an uniform illumination in axial direction. Light-sheet illumination would be advantageous. The image is reconstructed with the Software rapidSTORM with an output of listed localisation coordinates. For the 3D approach further evaluation is necessary as described in Franke, Sauer, and Linde, 2017 for TRABI 3D reconstruction and in Proppert, 2015 for astigmatic imaging.

3.2.2 Visualisation of Correlated *d*STORM-SIM Images

The structure of the data sets of SIM and *d*STORM differs fundamentally. *d*STORM offers a list of localisations. Reconstruction softwares like rapid-STORM list every localisation with an additional information set on the position in x,y and z, the frame number of occurrence and the photon intensity. This pointillist informations needs to be transferred into a pixel or voxel grid. SIM reconstruction Software like the commercial Zen Software (Zeiss) create an pixel-based output, mainly a hyperstack with channel and z-layer information. Those two sets of information need to be combined, aligned and rendered to gain a cohesive image. This demands a performance optimised read-out and strong graphical processing.

coSI*d*STORM

The Software coSI*d*STORM is fundamentally based on the phyton-based program vividSTORM published in Barna et al., 2016 that combined STORM and LSM measurements. The interior was changed substantially while focussing on improving the processing of high amounts of data and visualising them in suitable three-dimensional rendering. The software was programmed by the Bachelor student Sebastian Reinhardt. The main features

of the program and the improvement towards vividSTORM are explained in the following.

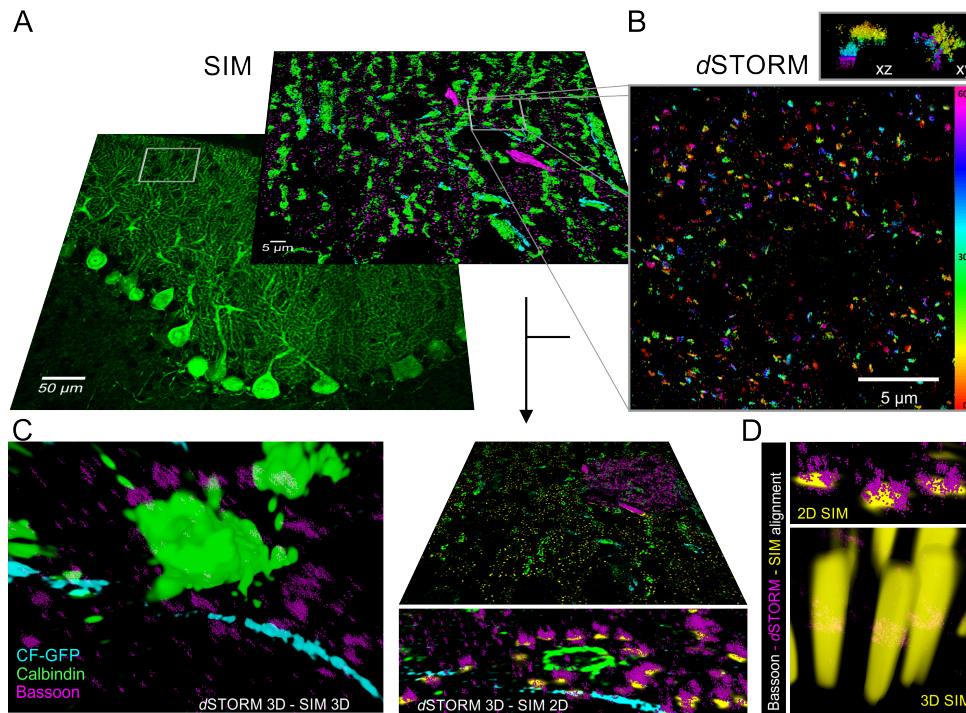The Software coSI*d*STORM is a tool to visualize big data sets of localisa-

FIGURE 3.22: (A) SIM (10x and 63x magnification) imaging of a 20 μm thick brain slice of a perfused mouse. The three colour staining shows climbing fibers (cyan, GFP transgenetic), Calbindin (green, Alexa Fluor 568, antibody staining) and Bassoon (magenta, Alexa Fluor 647, antibody staining) in the molecular layer of the cerebellum. (B) In the *d*STORM image Bassoon is visualised and the three-dimensional information is colour-coded in a range in between 0 - 600 nm. The inset (upper corner) shows two close synapses from orthogonal directions (xz and xy layer). The axial resolution is sufficient to separate the two synapses. (C) Overlay of the *d*STORM and SIM image performed with coSI*d*STORM. The SIM image serves a wider overview, while *d*STORM offers a detailed visualisation of the Bassoon distribution. (D) Comparison of the SIM and *d*STORM reconstruction. The images can be aligned via this structure though the difference in resolution is striking.

tion data and combine them with image-based SIM data sets. The display is openGL based and allows computing processes on graphic cards instead of sequential processing via the CPU. The performance is therefore increased and rendering can be performed in real time. For the 3D visualisation of SMLM data a point cloud visualisation tool is used with a rendering in which the radius of the localisation sphere is proportional to the precision of the localisation. The display of the SIM files is implemented by ray-casting, which also allows real-time rendering. coSI*d*STORM allows the registration of the *d*STORM data set to the SIM images by comparison of the structure of

one label imaged in both approaches and/or by setting landmarks. With the aid of this visualisation, areas of high interest can be identified and exported individually to enable further analysis on specific areas.

In Figure 3.22 the capabilities of this correlative method and Software are presented. From an overview of the molecular layer in the cerebellum (A - 10-fold magnification) to highly-resolved 80 μm x 80 μm field of view with SIM, we can zoom in to a super-resolved image of the synaptic active zones in the cerebellum with *d*STORM (B). The improvement of the resolution of *d*STORM towards SIM is shown in item D of Figure 3.22 by comparing the same structure in method specific resolution. coSI*d*STORM enables an accurate alignment of both image information and sets therefore a three-dimensional proteins distribution into a cellular multi-target context.

Software-Features coSI*d*STORM is an executable Software and is a ready to use package that runs on the operating platform Windows 8 and 10. The API openGL demands a Nvidia graphic card. For the the registration process the Fiji plugin bUnwarpJ is implemented. Therefore the open spource platform Fiji.app should be installed. In Figure 3.23 the start-interface of coSI*d*STORM is shown with all main functions being labelled.
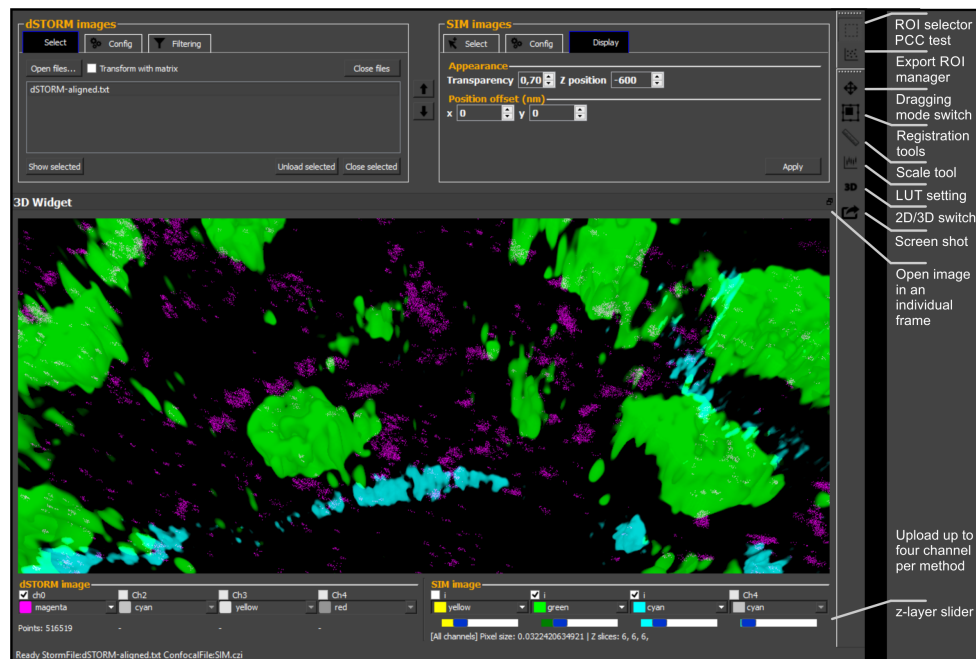

FIGURE 3.23: Functions of coSI*d*STORM: A) The main surface of the Software offers configurations for the SMLM data representation on the upper left frame and for SIM images of the right. The icons at the right rim of the frame enable functions for manipulation the combined image, for example the registration and export process.

The labelled functions are explained in the following:

*d*STORM image frame	Upload of localisation list and configuration input information. Size manipulation of localisation sphere and filtering by photon count, frame number and density.
SIM image frame	Upload of a SIM image file. Configuration of the layer settings and pixel size (readout of metadata per default). Display bar enables change of z-position relative to the localisation data.
ROI selector - PCC test	For a rectangular region of interest the Pearson's correlative coefficient is determined in between the *d*STORM and SIM image.
Export ROI manager	The image data of an ROI and the list of localisation in that area can be exported.
Dragging mode switch	In the default mode the whole image set can be dragged or tilted. With the pushed icon the images can be moved relative to each other in x-y-direction.
Registration tool	Landmarks can be set for both images and an affine transformation or an elastic transformation via the plugin bUnwarbJ can be executed.
Scale tool	Display of coordinate system with a scale grid or implementation of a scale bar.
LUT settings	Look up table for brightness correction
2D/3D switch	Both images can be switched into plane mode or 3D mode. Per default the localisation data is visualised in the maximum number of dimensions and the SIM data in 2D. The layers can be chosen individually per SIM channel. For a 3D SIM visualisation a ROI is necessary.
Screenshot	Saves screenshot of the actual frame.

Work-Flow for coSI*d*STORM   A short work-flow is added here to guide the way how the in this work presented images were created (compare Figure 3.24 A).

Start main.exe to proceed. To load an image, open a localisation text file, preferential in the rapidSTORM format. With the LUT tool and several filters the visibility of the localisation data is optimised. A local density filter helps to reduce sparse localisations. Perform a coarse image alignment manually by shifting the SIM image to the proper position (button

image shift). Identify the potential z-layer and shift the z-value to the corresponding *d*STORM z-position (3.24 B). Open the registration tools and set
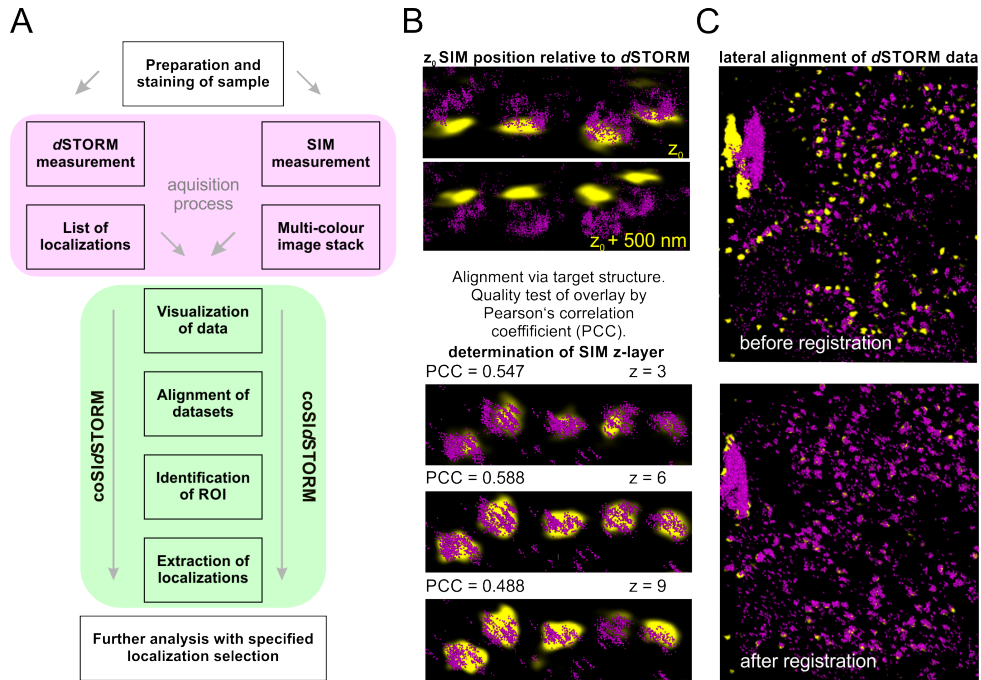

FIGURE 3.24: A) Short work-flow overview for a correlated-SIM-*d*STORM image. The whole visualisation process is realised by coSI*d*STORM. B) The z-position of the image data is not determined in a global coordinate system. The appropriate layers need to be assigned to each other. The best fitting SIM z-layer can be determined with a correlation test (PCC of the image information). C) A lateral registration can be performed by an affine transformation or with an elastic transformation by bUnwarbJ.

landmarks to identify matching structures. A left-mouse-double-click sets a marker for the localisation image and a right-mouse-double-click to the SIM image. Indicate the source folder of the Fiji.app and perform a transformation. The affine transformation is fast and orients solely on the set landmarks, while the elastic transformation of bUnwarbJ is slower (duration in the range of milliseconds), but more accurate, since it takes landmarks and image information into account. A maximum of nine landmarks can be set. To show the transformed image, select from the source folder of the localisation data the file sourcefilename_temp.txt and press "show selected". Note that sometimes more than one transformation process is recommendable to attain a suitable alignment. The transformation matrix is a temporary file in the folder $temp$. For permanent storage, the data set needs to be saved manually.

To test, if the chosen z-layer and the registration is valid, a colocalisation test between the *d*STORM and SIM image can processed. Therefore choose with the ROI selector an area and the structural resemblance is indicated by the Pearson's correlation coefficient (PCC). The corresponding SIM z-layer should give the highest correlation value. A screen-shot function lets you

capture the present frame. The ROI export manager gives you the option to save a two dimensional image of either data set or a combined one of localisation and SIM data. Localisation data of a region of interest is exported in form of a localisation list with the same header as the source.

Sample Structure - Bassoon in the Cerebellum   We applied coSI*d*STORM to image the distribution of the pre-synaptic protein Bassoon in active zones affiliated to Purkinje cells in the molecular layer of the cerebellum. For the
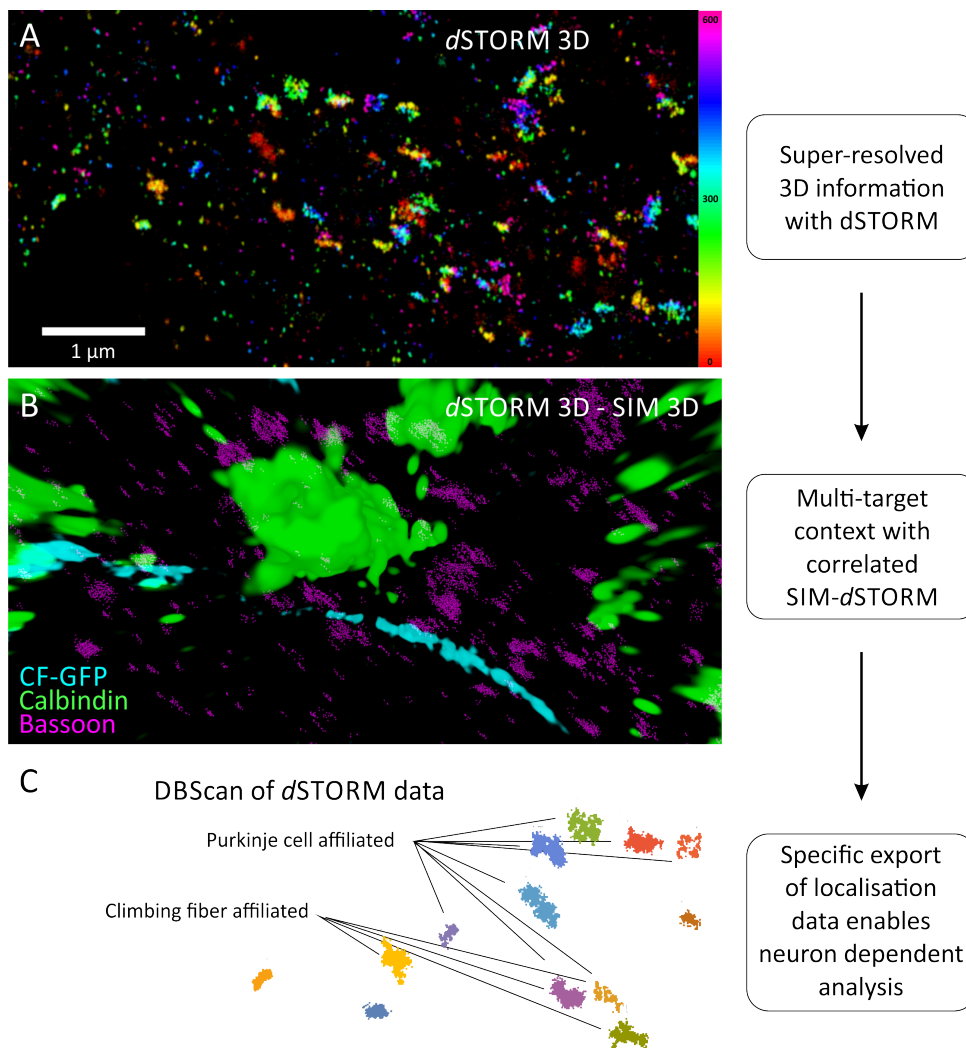
FIGURE 3.25: Correlative measurement enables neuron specific analysis: A) The 3D *d*STORM image resolves the Bassoon distribution with a high precision. B) The correlation with the SIM image via coSI*d*STORM exhibits the cellullar context, with the result that we can in C) analyse the Bassoon localisations distinct by their affilation.

experiments the Eilers Lab (University of Leipzig, Medical Faculty) provided a CF-GFP (CF climbing fiber) transgenic mouse. The immersion-fixated brain is P18 and was sliced with a cryotome in sagital directing of

cutting with help of Barbara Gado of the group of Prof. A.-L. Sirèn (Experimental neurosurgery, University clinic of Würzburg. I prepared slices of 20 μm thickness. The slices are stored in -20°C until staining. The immunostaining is performed as described in Chapter 2 paragraph "Tissue staining". As primary antibodies anti Calbindin-D-28k (host chicken, polyclonal, dilution 1:200; Synaptic systems) and anti-Bassoon (host mouse, monoclonal, dilution 1:200; Enzo) were used. The secondary antibodies Alexa Fluor 568 goat anti chicken (abcam) and Alexa Fluor 647 goat anti mouse (ThermoFischer) were both diluted 1:200.

It was managed to identify corresponding areas and perform a three colour, three dimensional correlated imaging experiment and single synapses at the contact points of Purkinje dendrites and climbing fiber axons can be identified via the active zone staining of bassoon. Bassoon was imaged with a biplane detection setup to gain axial information of the localisations. To increase the accuracy of the *d*STORM image and enable a super-resolved image of an axial range of 600 nm, the reconstruction was performed with the TRABI approach (Franke, Sauer, and Linde, 2017).

Possible application of this scenario are a specified analysis of the form and size of active zones in regard to their affiliated neuron types. Therefore possible differences in certain functionality dependent aggregation processes could be identified.

Also neurons that were prior analysed with physiological measurements can be targeted specificly with the correlated SIM-*d*STORM approach and selected areas can be analysed in a super-resolved matter.

Chapter 4

Conclusion and Outlook

This work provides insight into the applications of two-colour *d*STORM imaging in the field of neuroscience. Improvements in both methodological and analytical aspects of *d*STORM show promise for the use in synaptic protein research.
An improved work flow description of the analysis of dual-colour data using cluster and correlation analysis is given with the aim to facilitate its application on future protein interaction issues. An increased understanding of these analytical tools supports the comparability of SMLM imaging methods and brings these methods one step closer to becoming a standardized quantification tool.

Investigations that addressed the distribution of synaptic proteins in cultured neurons and therefore in a confined area are an ideal field of application for *d*STORM measurements. In the project with Dr. Robert Blum we could address a controversial issue regarding the distribution of the brain derived neurotrophic factor (BDNF) in hippocampal neurons, which is a key factor in synaptic plasticity. For the first time endogenous protein distributions could be investigated due to the single molecule sensitivity of *d*STORM and we could measure enriched occurance of BDNF in glutamatergic pre-synapses in mature hippocampal cultures. In light of this data, BDNF might be formed in the somatic compartment of the neuron and be brought to the glutamatergic pre-synapse by anterograte transport. Knowing the spatial distribution of BDNF is an important aspect for understanding the molecular processes involved in synaptic plasticity and could be further investigated with super-resolution imaging. The regulation of hippocampal synaptic plasticity by BDNF and its fundamental role in long-term potentiation has been reviewed recently by Leal, Bramham, and Duarte, 2017. However, the direct comparision of BDNF patterning in various time-points of the maturation process of synapses is still a topic that should be elucidated by quantitative *d*STORM analysis.

The metabotropic glutamate receptor mGlu4, a member of the transmembrane G-protein coupled receptor family, is involved in most aspects of normal brain function. The mGlu4 receptor participates in the modulation of synaptic transmission by progressing signals to intracellular signalling

partners under activation. The widespread expression of glutamate receptors makes these proteins attractive drug targets (Niswender and Conn, 2010). Therefore the exact understanding of spacial and functional interaction is of interest. Nevertheless structural understanding at the molecular level could confirm recent theories based on functional measurements of potential interaction partners of mGlu4 receptors.

In this context we investigated the distribution of the mGlu4 receptor in the molecular layer of cerebellar mouse-brain slices in cooperation with Prof. Dr. Davide Calebiro. This is an ongoing project and until now we have unravelled the four to six fold increased density of mGlu4 in pre-synaptic sites identified by bassoon staining. A correlation between mGlu4 and bassoon could be identified with coordinate based correlation analysis as well as with distance analysis of single receptors in regard to the clustered bassoon distribution in pre-synaptic active zones. However, in the ensemble of thousands of measured synapses we could not identify a certain distributional pattern of mGlu4 receptors in the synapse that differs significantly from a random receptor arrangement. This result does not exclude the possibility of function dependant clustering or a development of nanodomains in the active zone. However, we could not find a density gradient towards the outer rim or the centre of the synapse.

In the publication by Glebov et al., 2017 it is claimed that some synaptic proteins in the active zone (AZ) perform "nanoclustering", which leads to the hypothesis that functional processes in the AZ are locally controlled through molecular crowding. A challenge by gathering reliable data in the context of mGlu4 lies in the small number of proteins in one synaptic site, which was estimated to be around 2-5 receptors on average. Statistically solid approaches for pattern recognition might confirm nanoclustering also for mGlu4 receptors and therefore offer a more diverse insight to functional related molecular crowding.

The mGlu4 receptor belongs to a group of G-protein coupled receptors that function in form of dimers (Gurevich and Gurevich, 2008). Despite expectations of seeing homo-dimerisation of the mGlu4 receptor, quantitative analysis of the *d*STORM data did not lead to any conclusive statement whether the distribution of mGlu4 receptors underlie a homo-, hetero- or any dimerisation at all. We found that the long labelling cascade of primary and secondary antibodys widens the stochastic distribution for stoichiometry, thus we failed to set the blinking statistic into direct correlation to the number of targets. For further analysing a direct labelling approach would be advantageous decreasing the variance of localisation events. This is enabled with co-expression of fluorescent proteins or markers, or a direct peptide binding as it was realized for the post-synaptic protein gephyrin (Maric et al., 2017). This decreases the variance of localisation events. Combined with a control staining of single mGlu4 receptors expressed on a cell membrane, one of these approaches could help to gain more specific data on mGlu4 receptor stoichiometry. Recently Hummer, Fricke, and Heilemann, 2016 showed that the counting of molecules with SMLM methods is feasible, if the signature

of the fluorescent blinking is unravelled. This was shown for the fluorescent protein mEos.

Furthermore, we aimed to identify the affiliation of mGlu4 with the voltage-gated calcium channel Ca$_v$2.1. We could evaluate with a complementary approach of coordinate based correlation analysis and nearest neighbour analysis of cluster centroids that the correlation of the mGlu4 receptor and the voltage-gated calcium channel Ca$_v$2.1 varies from a random distribution and we can find a subset of almost 50% of the receptor population being located within a distance of on average 60 nm to a calcium channel. With coordinate based correlation analysis alone we could not determine any affiliation with Munc18, a protein involved in vesicle priming at the pre-synaptic site. Determining the nearest neighbour distances of Munc18 and mGlu4 cluster centroids is a logical continuation of this project to either confirm or discard the hypothesis of correlation.

Correlation analysis approaches like coordinate based correlation analysis and the nearest neighbour analysis of cluster centroids enable the evaluation of whether two proteins are spatially correlated in any way. However, such interpretation of experimental data also requires analytical skills of the user. The visualization of the correlation values by binning them into three groups of correlated, uncorrelated and anti-correlated, plotting them over increasing radii, created a distinguished distribution pattern. Here it would be interesting if we could further simplify this visualisation and create a guideline for distinguishable correlation patterns, by creating a lookup table from simulations of different correlation types of typical cluster distributions.

It is important to create relatable analysis approaches to gain a higher acceptance and a higher compatibility of SMLM data processing.

All above mentioned localisation based analysis methods have the advantage that they are applicable on 2D and 3D data sets, although a crucial point will be the computation power that is needed for the large amount of data processed in three-dimensional measurements. In the mGlu4 project we could circumvent 3D analysis by identifying different cluster analysis parameters that enabled the distinction for front and side view synapses. Since 2D measurements are experimentally less demanding it allowed us a higher data throughput. However, it is undeniable that multi-colour 3D *d*STORM would enable a more holistic overview. Characteristics like the average size of a synapse could be measured directly.

In this work I also showed that for approaching a three-dimensional extended structure the correlative approach of combined SIM-*d*STORM imaging is advantageous. Both super-resolution techniques not only differ in their spatial and temporal resolution, but also in the type of fluorophore that is used. Despite the fact that SIM is not limited to the limited choice

of *d*STORM applicable dyes, one and the same fluorophore results in a different response of the method. Localisation microscopy is sensitive to signals of single molecules and therefore recognizes low fluorophore densities, whereas SIM responds linearly to the fluorophore density and gains quality with increased signal. Therefore an intrinsic control for potential artefacts is given.

In the context of neuroscience, where there are hundreds of types of synapses that operate by the same fundamental mechanism, but exhibit distinct computational properties, correlated SIM-*d*STORM can help to unravel protein peculiarities of specific neuronal connections.
Our software coSI*d*STORM facilitates the visualisation process of a combined SIM-*d*STORM image and provides a reliable tool for fast registration. In the near future coSI*d*STORM could help combining functional methods with SMLM imaging. In the group of Prof. Dr. Hartmut Schmidt (University of Leipzig, Institute for Physiology) they enabled patch-clamp experiments in which they stain two specific neurons individually in organotypic brain slices. With SIM those neurons could be identified and analysed. Additionally the distribution of any desired synaptic proteins could be unravelled in close-ups by three-dimensional *d*STORM measurements. The performed experiment with the cerebellar cryo-slices mirrored this experimental setup, although brain tissue for physiological measurements tends to have an extension of several hundred micrometers. Samples of this thickness are not feasible for *d*STORM therefore reslicing would be necessary. If the neuron connection of interest is confined in a slice, coSI*d*STORM could enable this analysis if the neurons of interest remain uncompromised after cutting.
A further combination of the correlated SIM-*d*STORM approach with stitching protocols like tomoSTORM could bring super-resolved neuroimaging to another level. tomoSTORM combines single-molecule localization-based super-resolution microscopy with array tomography of structurally intact brain tissue as shown in Nanguneri et al., 2012 and Herrmannsdörfer et al., 2017.

In the introduction to my thesis I mentioned that the possibility of imaging a structure of a certain size requires that the target is in the range of the achievable resolution of the applied approach. Marrying complementary imaging techniques will offer deeper insights in the links between pathological phenotypes, molecule distribution and function. Further combinations with functional measurements will be the key to link structural imaging with cellular behaviour.

Appendix A

Abbreviations

AB	Antibody
AF-dyes	Alexa Fluor dyes
BSA	Bovine serum albumin
BDNF	Brain derived neurotrophic factor
CBC	Coordinate based correlation
CP	Cytoskeleton buffer
Cy-dyes	Carbocyanine dyes
DBScan	Density based scanning
DIV	Days in vitro
DMSO	Dimethylsulfoxid
*d***STORM**	*direct* stochastic optical reconstruction microscopy
EMCCD	Electron multiplying charge-coupled device
FA	Formaldehyde
FP	Fluorescent Protein
FWHM	Full width of half maximum of a Gaussian function
HILO	Highly inclined and laminated optical sheet
IgG	Immunglobulin G
MEA	β-Mercaptoethylamin
mGluR4	Metabotropic glutamate receptor 4
NA	Numerical aperture
PA-FP	Photoactivateable fluorescent protein
PALM	Photoactivateable Localization Microscopy
PBS	Phosphate buffered saline
PSF	Point spread function
RT	Room temperature

SIM	Structured illumination microscopy
SMLM	Single molecule localisation microscopy
STED	Stimulated emission depletion
STORM	Stochastic optical reconstruction microscopy
TIRF	Total internal reflection fluorescence

Appendix B

List of Figures

Appendix C

List of Tables

Appendix D

Publications

This thesis is based on following publications:

1. Steve Wolter, Anna Löschberger, Thorge Holm, Sarah Aufmkolk, Marie-Christine Dabauvalle, Sebastian van de Linde, and Markus Sauer. rapidSTORM: accurate, fast open-source software for localization microscopy. *Nat Meth,* **9**, 1040–1041 (2012).

2. Sebastian van de Linde, Sarah Aufmkolk, Christian Franke, Thorge Holm, Teresa Klein, Anna Löschberger, Sven Proppert, Steve Wolter, and Markus Sauer. Investigating Cellular Structures at the Nanoscale with Organic Fluorophores. *Chemistry & Biology,* **20**, 8 - 18 (2013).

3. Markus Sauer, Sebastian van de Linde, Thorge Holm, Sarah Aufmkolk, Nadine Ehmann, Robert Blum, Dana Bar-On, Amit Alon, Uri Ashery , Dimitrij Ljaschenko, Manfred Heckmann, Robert Kittel. *d*STORM of Synaptic Proteins. *Biophysical Journal,* **104**(2):341 (2013)

4. Thomas Andreska*, Sarah Aufmkolk*, Markus Sauer, and Robert Blum. High abundance of BDNF within glutamatergic presynapses of cultured hippocampal neurons. *Frontiers in Cellular Neuroscience,* **8**, (2014). * *authors equally contributed*

5. Sarah Aufmkolk, Sebastian Reinhardt, and Markus Sauer. 3D visualization of correlative SIM and SMLM data. (in submission)

Bibliography

Abbe, Ernst (1873). "Beiträge zur Theorie des Mikroskops und der mikroskopischen Wahrnehmung". In: *Archiv für Mikroskop. Anatomie* 9, pp. 413–418.

Abitbol, Karine et al. (2012). "A new signalling pathway for parallel fibre presynaptic type 4 metabotropic glutamate receptors (mGluR4) in the rat cerebellar cortex". In: *The Journal of physiology* 590.13, pp. 2977–2994.

Albou, Laurent-Philippe et al. (2009). "Defining and characterizing protein surface using alpha shapes." In: *Proteins* 76 (1), pp. 1–12.

Altar, C A et al. (1997). "Anterograde transport of brain-derived neurotrophic factor and its role in the brain." In: *Nature* 389 (6653), pp. 856–860.

Andreska, Thomas et al. (2014). "High abundance of BDNF within glutamatergic presynapses of cultured hippocampal neurons." In: *Frontiers in cellular neuroscience* 8, p. 107.

Annibale, Paolo et al. (2011). "Quantitative photo activated localization microscopy: unraveling the effects of photoblinking." In: *PloS one* 6 (7), e22678.

Aufmkolk, Sarah (2012). "Hochauflösende Mehrfarben-Fluoreszenzmikroskopie". MA thesis. Julius-Maximilians-Universität Würzburg.

Barde, Y A, D Edgar, and H Thoenen (1982). "Purification of a new neurotrophic factor from mammalian brain." In: *The EMBO journal* 1 (5), pp. 549–553.

Barna, Laszlo et al. (2016). "Correlated confocal and super-resolution imaging by VividSTORM." In: *Nature protocols* 11 (1), pp. 163–183.

Bates, Mark, Timothy R Blosser, and Xiaowei Zhuang (2005). "Short-range spectroscopic ruler based on a single-molecule optical switch." In: *Physical review letters* 94 (10), p. 108101.

Bates, Mark et al. (2007). "Multicolor super-resolution imaging with photoswitchable fluorescent probes." In: *Science (New York, N.Y.)* 317 (5845), pp. 1749–1753.

Betzig, E (1995). "Proposed method for molecular optical imaging." In: *Optics letters* 20 (3), pp. 237–239.

Betzig, Eric (2005). "Excitation strategies for optical lattice microscopy." In: *Optics express* 13 (8), pp. 3021–3036.

Blum, Robert and Arthur Konnerth (2005). "Neurotrophin-mediated rapid signaling in the central nervous system: mechanisms and functions." In: *Physiology (Bethesda, Md.)* 20, pp. 70–78.

Brigadski, Tanja, Matthias Hartmann, and Volkmar Lessmann (2005). "Differential vesicular targeting and time course of synaptic secretion of the mammalian neurotrophins." In: *The Journal of neuroscience : the official journal of the Society for Neuroscience* 25 (33), pp. 7601–7614.

Canossa, M et al. (2001). "Regulated secretion of neurotrophins by metabotropic glutamate group I (mGluRI) and Trk receptor activation is mediated via phospholipase C signalling pathways." In: *The EMBO journal* 20 (7), pp. 1640–1650.

Cheng, Pei-Lin et al. (2011). "Self-amplifying autocrine actions of BDNF in axon development." In: *Proceedings of the National Academy of Sciences of the United States of America* 108 (45), pp. 18430–18435.

Conner, J M et al. (1997). "Distribution of brain-derived neurotrophic factor (BDNF) protein and mRNA in the normal adult rat CNS: evidence for anterograde axonal transport." In: *The Journal of neuroscience : the official journal of the Society for Neuroscience* 17 (7), pp. 2295–2313.

Coons, Albert H, Hugh J Creech, and R Norman Jones (1941). "Immunological Properties of an Antibody Containing a Fluorescent Group." In: *Proceedings of the Society for Experimental Biology and Medicine* 47.2, pp. 200–202.

Corti, C et al. (2002). "Distribution and synaptic localisation of the metabotropic glutamate receptor 4 (mGluR4) in the rodent CNS." In: *Neuroscience* 110 (3), pp. 403–420.

Costes, Sylvain V et al. (2004). "Automatic and quantitative measurement of protein-protein colocalization in live cells." In: *Biophysical journal* 86 (6), pp. 3993–4003.

Dani, Adish et al. (2010). "Superresolution imaging of chemical synapses in the brain". In: *Neuron* 68.5, pp. 843–856.

Day, Richard N and Michael W Davidson (2009). "The fluorescent protein palette: tools for cellular imaging." In: *Chemical Society reviews* 38 (10), pp. 2887–2921.

Dean, Camin et al. (2009). "Synaptotagmin-IV modulates synaptic function and long-term potentiation by regulating BDNF release." In: *Nature neuroscience* 12 (6), pp. 767–776.

Deschout, H et al. (2014). "Progress in quantitative single-molecule localization microscopy." In: *Histochemistry and cell biology* 142 (1), pp. 5–17.

Dieni, Sandra et al. (2012). "BDNF and its pro-peptide are stored in presynaptic dense core vesicles in brain neurons." In: *The Journal of cell biology* 196 (6), pp. 775–788.

Dolphin, Annette C (2003). "G protein modulation of voltage-gated calcium channels." In: *Pharmacological reviews* 55 (4), pp. 607–627.

Edelsbrunner, H., D. Kirkpatrick, and R. Seidel (1983). "On the Shape of a Set of Points in the Plane". In: *IEEE Trans. Inf. Theor.* 29.4, pp. 551–559.

Ehmann, Nadine et al. (2014). "Quantitative super-resolution imaging of Bruchpilot distinguishes active zone states." In: *Nature communications* 5, p. 4650.

Endesfelder, Ulrike et al. (2013). "Multiscale spatial organization of RNA polymerase in Escherichia coli". In: *Biophysical journal* 105.1, pp. 172–181.

Endesfelder, Ulrike et al. (2014). "A simple method to estimate the average localization precision of a single-molecule localization microscopy experiment." In: *Histochemistry and cell biology* 141 (6), pp. 629–638.

Ester, Martin et al. (1996). "A density-based algorithm for discovering clusters in large spatial databases with noise." In: *Kdd*. Vol. 96. 34, pp. 226–231.

Figurov, A et al. (1996). "Regulation of synaptic responses to high-frequency stimulation and LTP by neurotrophins in the hippocampus." In: *Nature* 381 (6584), pp. 706–709.

Franke, Christian, Markus Sauer, and Sebastian van de Linde (2017). "Photometry unlocks 3D information from 2D localization microscopy data." In: *Nature methods* 14 (1), pp. 41–44.

Frost, Nicholas A et al. (2010). "Single-molecule discrimination of discrete perisynaptic and distributed sites of actin filament assembly within dendritic spines." In: *Neuron* 67 (1), pp. 86–99.

Galbraith, Catherine G. and James A. Galbraith (2011). "Super-resolution microscopy at a glance". In: *Journal of Cell Science* 124.10, pp. 1607–1611.

Glebov, Oleg O et al. (2017). "Nanoscale Structural Plasticity of the Active Zone Matrix Modulates Presynaptic Function." In: *Cell reports* 18 (11), pp. 2715–2728.

Gottschalk, W et al. (1998). "Presynaptic modulation of synaptic transmission and plasticity by brain-derived neurotrophic factor in the developing hippocampus." In: *The Journal of neuroscience : the official journal of the Society for Neuroscience* 18 (17), pp. 6830–6839.

Greenfield, Derek et al. (2009). "Self-organization of the Escherichia coli chemotaxis network imaged with super-resolution light microscopy." In: *PLoS biology* 7 (6), e1000137.

Gurevich, Vsevolod V and Eugenia V Gurevich (2008). "How and why do GPCRs dimerize?" In: *Trends in pharmacological sciences* 29 (5), pp. 234–240.

Gustafsson, Mats G L (2005). "Nonlinear structured-illumination microscopy: wide-field fluorescence imaging with theoretically unlimited resolution". In: *Proceedings of the National Academy of Sciences of the United States of America* 102.37, pp. 13081–13086.

Gustafsson, Mats G L et al. (2008). "Three-dimensional resolution doubling in wide-field fluorescence microscopy by structured illumination." In: *Biophysical journal* 94 (12), pp. 4957–4970.

Gustafsson, Mats GL (2000). "Surpassing the lateral resolution limit by a factor of two using structured illumination microscopy". In: *Journal of microscopy* 198.2, pp. 82–87.

Hamel, Virginie et al. (2014). "Correlative multicolor 3D SIM and STORM microscopy." In: *Biomedical optics express* 5 (10), pp. 3326–3336.

Hampton, Cheri M et al. (2017). "Correlated fluorescence microscopy and cryo-electron tomography of virus-infected or transfected mammalian cells." In: *Nature protocols* 12 (1), pp. 150–167.

Hartmann, M, R Heumann, and V Lessmann (2001). "Synaptic secretion of BDNF after high-frequency stimulation of glutamatergic synapses." In: *The EMBO journal* 20 (21), pp. 5887–5897.

Heilemann, Mike et al. (2005). "Carbocyanine dyes as efficient reversible single-molecule optical switch." In: *Journal of the American Chemical Society* 127 (11), pp. 3801–3806.

Heilemann, Mike et al. (2009). "Super-resolution imaging with small organic fluorophores". In: *Angewandte Chemie International Edition* 48.37, pp. 6903–6908.

Heintzmann, Rainer and Christoph G Cremer (1999). "Laterally modulated excitation microscopy: improvement of resolution by using a diffraction grating". In: *BiOS Europe'98*. International Society for Optics and Photonics, pp. 185–196.

Herrmannsdörfer, Frank et al. (2017). "3D d STORM Imaging of Fixed Brain Tissue". In: *Synapse Development: Methods and Protocols*, pp. 169–184.

Huang, Bo et al. (2008a). "Three-dimensional super-resolution imaging by stochastic optical reconstruction microscopy." In: *Science (New York, N.Y.)* 319 (5864), pp. 810–813.

Huang, Yang Z et al. (2008b). "Zinc-mediated transactivation of TrkB potentiates the hippocampal mossy fiber-CA3 pyramid synapse." In: *Neuron* 57 (4), pp. 546–558.

Hummer, Gerhard, Franziska Fricke, and Mike Heilemann (2016). "Model-independent counting of molecules in single-molecule localization microscopy". In: *Molecular biology of the cell* 27.22, pp. 3637–3644.

Izeddin, Ignacio et al. (2011). "Super-resolution dynamic imaging of dendritic spines using a low-affinity photoconvertible actin probe." In: *PloS one* 6 (1), e15611.

Juette, Manuel F et al. (2008). "Three-dimensional sub-100 nm resolution fluorescence microscopy of thick samples." In: *Nature methods* 5 (6), pp. 527–529.

Kammermeier, Paul J (2012). "Functional and pharmacological characteristics of metabotropic glutamate receptors 2/4 heterodimers." In: *Molecular pharmacology* 82 (3), pp. 438–447.

Kao, H Pin and AS Verkman (1994). "Tracking of single fluorescent particles in three dimensions: use of cylindrical optics to encode particle position". In: *Biophysical journal* 67.3, pp. 1291–1300.

Kinoshita, A et al. (1996). "Presynaptic localization of a metabotropic glutamate receptor, mGluR4a, in the cerebellar cortex: a light and electron microscope study in the rat." In: *Neuroscience letters* 207 (3), pp. 199–202.

Klar, T A and S W Hell (1999). "Subdiffraction resolution in far-field fluorescence microscopy." In: *Optics letters* 24 (14), pp. 954–956.

Klein, Teresa, Sven Proppert, and Markus Sauer (2014). "Eight years of single-molecule localization microscopy". In: *Histochemistry and cell biology* 141.6, pp. 561–575.

Kohara, K et al. (2001). "Activity-dependent transfer of brain-derived neurotrophic factor to postsynaptic neurons." In: *Science (New York, N.Y.)* 291 (5512), pp. 2419–2423.

Korte, M et al. (1995). "Hippocampal long-term potentiation is impaired in mice lacking brain-derived neurotrophic factor." In: *Proceedings of the National Academy of Sciences of the United States of America* 92 (19), pp. 8856–8860.

Kunishima, N et al. (2000). "Structural basis of glutamate recognition by a dimeric metabotropic glutamate receptor." In: *Nature* 407 (6807), pp. 971–977.

Laine, Romain F et al. (2016). "From single-molecule spectroscopy to super-resolution imaging of the neuron: a review". In: *Methods and Applications in Fluorescence* 4.2, pp. 1–12.

Lampe, André et al. (2012). "Multi-colour direct STORM with red emitting carbocyanines." In: *Biology of the cell* 104 (4), pp. 229–237.

Lazo, Oscar M et al. (2013). "BDNF regulates Rab11-mediated recycling endosome dynamics to induce dendritic branching." In: *The Journal of neuroscience : the official journal of the Society for Neuroscience* 33 (14), pp. 6112–6122.

Leal, G, CR Bramham, and CB Duarte (2017). "Chapter Eight-BDNF and Hippocampal Synaptic Plasticity". In: *Vitamins and Hormones* 104, pp. 153–195.

Lichtman, Jeff W and Winfried Denk (2011). "The big and the small: challenges of imaging the brain's circuits." In: *Science (New York, N.Y.)* 334 (6056), pp. 618–623.

Linde, Sebastian van de and Markus Sauer (2014). "How to switch a fluorophore: from undesired blinking to controlled photoswitching". In: *Chem. Soc. Rev. 2014* 43(4), pp. 1076–1087.

Linde, Sebastian van de et al. (2009). "Multicolor photoswitching microscopy for subdiffraction-resolution fluorescence imaging". In: *Photochemical & Photobiological Sciences* 8.4, pp. 465–469.

Linde, Sebastian van de et al. (2011). "Direct stochastic optical reconstruction microscopy with standard fluorescent probes." In: *Nature protocols* 6 (7), pp. 991–1009.

Linde, Sebastian van de et al. (2013). "Investigating Cellular Structures at the Nanoscale with Organic Fluorophores". In: *Chemistry & Biology* 20.1, pp. 8 –18.

Malkusch, Sebastian et al. (2012). "Coordinate-based colocalization analysis of single-molecule localization microscopy data." In: *Histochemistry and cell biology* 137 (1), pp. 1–10.

Manders, EM et al. (1992). "Dynamics of three-dimensional replication patterns during the S-phase, analysed by double labelling of DNA and confocal microscopy". In: *Journal of cell science* 103.3, pp. 857–862.

Manders, EMM, FJ Verbeek, and JA Aten (1993). "Measurement of co-localization of objects in dual-colour confocal images". In: *Journal of microscopy* 169.3, pp. 375–382.

Mönkemöller, Viola et al. (2015). "Multimodal super-resolution optical microscopy visualizes the close connection between membrane and the cytoskeleton in liver sinusoidal endothelial cell fenestrations." In: *Scientific reports* 5, p. 16279.

Manley, Suliana et al. (2008). "High-density mapping of single-molecule trajectories with photoactivated localization microscopy". In: *Nature methods* 5.2, pp. 155–157.

Maric, Hans Michael et al. (2017). "Gephyrin-binding peptides visualize postsynaptic sites and modulate neurotransmission". In: *Nature chemical biology* 13.2, pp. 153–160.

Mateos, José Marıa et al. (1999). "Clustering of the group III metabotropic glutamate receptor 4a at parallel fiber synaptic terminals in the rat cerebellar molecular layer". In: *Neuroscience research* 35.1, pp. 71–74.

Matsuda, Atsushi et al. (2010). "Condensed mitotic chromosome structure at nanometer resolution using PALM and EGFP- histones." In: *PloS one* 5 (9), e12768.

McEvoy, Ann L et al. (2012). "mMaple: a photoconvertible fluorescent protein for use in multiple imaging modalities." In: *PloS one* 7 (12), e51314.

Moerner and Kador (1989). "Optical detection and spectroscopy of single molecules in a solid." In: *Physical review letters* 62 (21), pp. 2535–2538.

Mortensen, Kim I et al. (2010). "Optimized localization analysis for single-molecule tracking and super-resolution microscopy." In: *Nature methods* 7 (5), pp. 377–381.

Muto, Takanori et al. (2007). "Structures of the extracellular regions of the group II/III metabotropic glutamate receptors". In: *Proceedings of the National Academy of Sciences* 104.10, pp. 3759–3764.

Nan, Xiaolin et al. (2013). "Single-molecule superresolution imaging allows quantitative analysis of RAF multimer formation and signaling." In: *Proceedings of the National Academy of Sciences of the United States of America* 110 (46), pp. 18519–18524.

Nanguneri, Siddharth et al. (2012). "Three-dimensional, tomographic super-resolution fluorescence imaging of serially sectioned thick samples". In: *PloS one* 7.5, e38098.

Niswender, Colleen M and P Jeffrey Conn (2010). "Metabotropic glutamate receptors: physiology, pharmacology, and disease". In: *Annual review of pharmacology and toxicology* 50, pp. 295–322.

Orefice, Lauren L et al. (2013). "Distinct roles for somatically and dendritically synthesized brain-derived neurotrophic factor in morphogenesis of dendritic spines." In: *The Journal of neuroscience : the official journal of the Society for Neuroscience* 33 (28), pp. 11618–11632.

Orrit and Bernard (1990). "Single pentacene molecules detected by fluorescence excitation in a p-terphenyl crystal." In: *Physical review letters* 65 (21), pp. 2716–2719.

Owen, Dylan M et al. (2010). "PALM imaging and cluster analysis of protein heterogeneity at the cell surface." In: *Journal of biophotonics* 3 (7), pp. 446–454.

Pageon, Sophie V et al. (2016). "Clus-DoC: a combined cluster detection and colocalization analysis for single-molecule localization microscopy data." In: *Molecular biology of the cell* 27 (22), pp. 3627–3636.

Park, Hyungju and Mu-ming Poo (2013). "Neurotrophin regulation of neural circuit development and function." In: *Nature reviews. Neuroscience* 14 (1), pp. 7–23.

Patterson, George H and Jennifer Lippincott-Schwartz (2002). "A photoactivatable GFP for selective photolabeling of proteins and cells." In: *Science (New York, N.Y.)* 297 (5588), pp. 1873–1877.

Pearson, Karl (1896). "Mathematical contributions to the theory of evolution.– on a form of spurious correlation which may arise when indices are used in the measurement of organs". In: *Proceedings of the royal society of london* 60.359-367, pp. 489–498.

Proppert, Sven Martin (2015). "Design, implementation and characterization of a microscope capable of three-dimensional two color super-resolution fluorescence imaging". PhD thesis.

Ramos, Cathy et al. (2012). "Native presynaptic metabotropic glutamate receptor 4 (mGluR4) interacts with exocytosis proteins in rat cerebellum." In: *The Journal of biological chemistry* 287 (24), pp. 20176–20186.

Rasnik, Ivan, Sean A McKinney, and Taekjip Ha (2006). "Nonblinking and long-lasting single-molecule fluorescence imaging." In: *Nature methods* 3 (11), pp. 891–893.

Rayleigh, Lord (1896). "XV. On the theory of optical images, with special reference to the microscope". In: *Philosophical Magazine* 42.255, pp. 167–195.

Rossberger, Sabrina et al. (2013). "Combination of structured illumination and single molecule localization microscopy in one setup". In: *J. Opt.* 15.9.

Südhof, Thomas C (2012). "The presynaptic active zone." In: *Neuron* 75 (1), pp. 11–25.

Sauer, Markus and Mike Heilemann (2017). "Single-Molecule Localization Microscopy in Eukaryotes." In: *Chemical reviews*.

Shannon, Claude Elwood (1949). "Communication in the presence of noise". In: *Proceedings of the IRE* 37.1, pp. 10–21.

Shen, Yi, Tiffany Lai, and Robert E Campbell (2015). "Red fluorescent proteins (RFPs) and RFP-based biosensors for neuronal imaging applications." In: *Neurophotonics* 2 (3), p. 031203.

Shigemoto, R et al. (1996). "Target-cell-specific concentration of a metabotropic glutamate receptor in the presynaptic active zone." In: *Nature* 381 (6582), pp. 523–525.

Shimomura, Osamu (1979). "Structure of the chromophore of Aequorea - green fluorescent protein". In: *FEBS letters* 104.2, pp. 220–222.

Small, Alex and Shane Stahlheber (2014). "Fluorophore localization algorithms for super-resolution microscopy". In: *Nature methods* 11.3, pp. 267–279.

Small, J et al. (1999). "Visualising the actin cytoskeleton". In: *Microscopy research and technique* 47.1, pp. 3–17.

Ströhl, Florian and Clemens F. Kaminski (2016). "Frontiers in structured illumination microscopy". In: *Optica* 3.6, pp. 667–677.

Subach, Fedor V et al. (2010). "Bright monomeric photoactivatable red fluorescent protein for two-color super-resolution sptPALM of live cells." In: *Journal of the American Chemical Society* 132 (18), pp. 6481–6491.

Tønnesen, Jan and U Valentin Nägerl (2013). "Superresolution imaging for neuroscience." In: *Experimental neurology* 242, pp. 33–40.

Winterflood, Christian M et al. (2015). "Dual-color 3D superresolution microscopy by combined spectral-demixing and biplane imaging." In: *Biophysical journal* 109 (1), pp. 3–6.

Wolter, Steve et al. (2011). "Measuring localization performance of super-resolution algorithms on very active samples." In: *Optics express* 19 (8), pp. 7020–7033.

Wolter, Steve et al. (2012a). "rapid STORM manual". In: *Biotechnologie & Biophysik, Universität Würzburg, version* 3.

Wolter, Steve et al. (2012b). "rapidSTORM: accurate, fast open-source software for localization microscopy." In: *Nature methods* 9 (11), pp. 1040–1041.

Xu, Ke, Guisheng Zhong, and Xiaowei Zhuang (2013). "Actin, spectrin, and associated proteins form a periodic cytoskeletal structure in axons." In: *Science (New York, N.Y.)* 339 (6118), pp. 452–456.

Zhao, Yongxin and Robert E. Campbell (2015). "Fluorescent Proteins for Neuronal Imaging". In: *New Techniques in Systems Neuroscience*. Ed. by Adam D. Douglass. Cham: Springer International Publishing, pp. 57–96.

Acknowledgements

I would like to thank everyone who supported me during the recent years.

First, I wish to thank Markus Sauer for giving me the opportunity to work in his group and for introducing me to many interesting projects during my time as a PhD student. Thank you cordially, Markus, for supporting me with expertise, enthusiasm and understanding. Not to mention the amazing experiences in the Alps. From Pizza to powder in two days with Markus and Marina. Thank you for these adventures!

I would also like to thank Manfred Heckmann for taking the time to be my second referee and helping me out in neuroscience related questions. It is a pleasure to exchange scientific expertise with you and your group.

Thank you, Sören Doose, for having an open ear. I really enjoyed discussions with you and I'm grateful for your amazing support regarding data analysis and your editing skills.

Working in an interdisciplinary field I had the opportunity to cooperate with many groups and I would like to express my gratitude for all the lovely and valuable experiences I gained in those times.
I would like to mention thankfully Jens Eilers and Anna-Leena Sìren for supporting me in a very uncomplicated way. Thank you, Davide Calebiro and Sana Siddig for working with me on my latest project.
I would like to send special thanks to my first cooperation partner Robert Blum. It was a pleasure to work and discuss with you! On this occasion many thanks to Thomas Andreska as well for the great team work.

I want to express my gratitude to the unequalled Sauer group. The working atmosphere and team spirit goes beyond any standards, thank you everyone for the many beautiful experiences.
Here, I want to mention my special thanks to the early crew: Sebastian van de Linde, thank you for exciting me about every single molecule we saw, Teresa for being not only my personal biology queen, but also for the latest support, Tobias Klamp (Hell yeah.) for being an endless spring of positivity (Alles sch... mit der Sch...), Steve Wolter and Andre Lampe for great explanations and advice.
Thanks to the one and only "Mauser Büro": Thorge Holm (and family) for making me smile, Julian Lehmann for the numerous adventures, Franz Engelmayer for taking me out. Thank you Christian RB Franke for being a companion since day one of my studies.
I also want to send my gratitude to Lisa Behringer-Pließ and Marcus Behringer for being a reference for countless questions. Thank you Sebastian Reinhardt for the exceptional work in your bachelor thesis.

Declaration of Authorship

Sarah Aufmkolk
Schadewitzstrasse 29
97074 Würzburg
sarah.aufmkolk@uni-wuerzburg.de

Erklärungen nach §4 Abs. 3 Satz 3, 5, 8 der Promotionsordnung der Fakultät für Biologie

Affidavit

I hereby declare that my thesis entitled: „Super-resolution microscopy of synaptic proteins" is the result of my own work.

I did not receive any help or support from commercial consultants. All sources and / or materials applied are listed and specified in the thesis.

Furthermore I verify that the thesis has not been submitted as part of another examination process neither in identical nor in similar form.

Eidesstattliche Erklärung

Hiermit erkläre ich an Eides statt, die Dissertation: „Super-resolution microscopy of synaptic proteins", eigenständig, d. h. insbesondere selbständig und ohne Hilfe eines kommerziellen Promotionsberaters, angefertigt und keine anderen, als die von mir angegebenen Quellen und Hilfsmittel verwendet zu haben.

Ich erkläre außerdem, dass die Dissertation weder in gleicher noch in ähnlicher Form bereits in einem anderen Prüfungsverfahren vorgelegen hat.

Signed:

Date: